

**SUSPENDED CARBON NANOTUBES
COUPLED TO SUPERCONDUCTING CIRCUITS**

**SUSPENDED CARBON NANOTUBES
COUPLED TO SUPERCONDUCTING CIRCUITS**

Proefschrift

ter verkrijging van de graad van doctor
aan de Technische Universiteit Delft,
op gezag van de Rector Magnificus Prof. ir. K. C. A. M. Luyben,
voorzitter van het College voor Promoties,
in het openbaar te verdedigen op donderdag 3 juli 2014 om 12:30 uur

door

Ben Helmut SCHNEIDER

natuurkundig doctorandus
geboren te Aken, Duitsland.

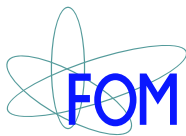
Dit concept-proefschrift is goedgekeurd door de promotor:

Prof. dr. ir. H. S. J. van der Zant

Samenstelling promotiecommissie:

Rector Magnificus,	voorzitter
Prof. dr. ir. H. S. J. van der Zant,	Technische Universiteit Delft, promotor
Dr. G. A. Steele,	Technische Universiteit Delft, copromotor
Prof. dr. Y. M. Blanter	Technische Universiteit Delft
Prof. dr. ir. L. P. Kouwenhoven	Technische Universiteit Delft
Prof. dr. ir. T. H. Oosterkamp	Universiteit Leiden
Prof. dr. tech. P. Hakonen	Aalto University School of Science, Finland
Prof. dr J. Hone	Columbia University, United States of America

Dr. G. A. Steele heeft als begeleider in belangrijke mate aan de totstandkoming van het proefschrift bijgedragen.



Nederlandse Organisatie voor Wetenschappelijk Onderzoek

Keywords: Nanomechanical devices, carbon nanotube, Josephson junction, NEMS, SQUID, superconducting, molybdenum, rhenium, ringdown

Printed by: Ipskamp

Front & Back: Ringdown response of a carbon nanotube.

Copyright © 2014 by B.H. Schneider

Casimir PhD Series, Delft-Leiden 2014-18

ISBN 978-94-6186-327-0

An electronic version of this dissertation is available at

<http://repository.tudelft.nl/>.

CONTENTS

1	Introduction	1
2	Background and theory	9
2.1	Carbon nanotube mechanics	10
2.2	Quantum transport in carbon nanotubes	15
2.2.1	Fabry-Pérot regime:	18
2.2.2	Coulomb Blockade regime	21
2.3	Superconducting Junctions	26
2.3.1	Josephson Junctions	26
2.3.2	Superconducting quantum interference device	28
2.3.3	Microscopic free electron model of Andreev Bound States in a CNT Josephson junction	30
3	Fabrication of carbon nanotube superconducting-circuits	37
3.1	Superconducting Materials	38
3.1.1	Niobium Titanium Nitride	38
3.1.2	Rhenium	42
3.1.3	Molybdenum-Rhenium	44
3.1.4	Concluding remarks	47
4	Coupling carbon nanotube mechanics to a superconducting circuit	53
4.1	Results	55
4.2	Discussion	59
4.3	Methods	60
4.4	Supplementary Information	64
5	Enhanced mechanical transduction with a suspended carbon nanotube Josephson junction	73
6	Decoherence in a carbon nanotube mechanical resonator	85
6.1	Introduction	86
6.2	Results	88
6.3	Ringdown Q_R factor	92

6.4	Discussions	93
6.5	Supplementary Information	97
6.5.1	Fabrication of the device	97
6.5.2	Theory: Ringdown of a resonator	97
6.5.3	Signal from the CNT	100
6.5.4	Input signal at the lock-in	102
6.5.5	Spectral measurements	106
6.5.6	Ringdown measurements	108
6.5.7	Model for ringdown	111
6.5.8	Gate dependent measurements	115
6.5.9	Residual driving when the switch is off	115
7	Spectroscopy of carbon nanotube superconducting junctions	117
7.1	Basic characterisation of the devices	118
7.2	Supercurrent in as-grown CNT junctions	121
7.3	Analysis of superconducting IV curves	126
7.4	Conversion of IV into VI plots	128
7.5	Spectroscopy up to $2\ \mu\text{A}$ current bias	134
7.5.1	Conclusion	136
7.6	Spectroscopy in the Coulomb blockade regime	139
7.6.1	Visible features in the CB regime.	140
7.7	NDC in co-tunnelling at higher gate voltages	141
7.7.1	Conclusion	142
7.8	Summary and conclusion	144
7.9	Supplementary Information	144
7.9.1	Basic characterisation at $25\ \text{mK}$	144
7.9.2	$I_C R_N$ product in the Fabry P�erot regime	145
7.9.3	CNT-JJ device shows hysteretic behaviour	146
7.9.4	Spectroscopy up to $100\ \text{nA}$ current bias	146
	Summary	151
	Samenvatting	155

1

INTRODUCTION

A music instrument is a mechanical resonator. When a music instrument such as a grand piano is played, we can hear a sound. This sound comes from a suspended string that oscillates inside the piano. As the string oscillates, sound waves are traveling through the air to the ear where it is heard. Depending on the note played, a different string with a different weight, tension or length produces a different sound. The human ear can hear sounds at a frequency in the range from 16 Hz up to 20 kHz. In the case of a resonating string, an important parameter is the quality factor. The quality factor of the resonator tells us for how long we can hear this sound after a note has been played.

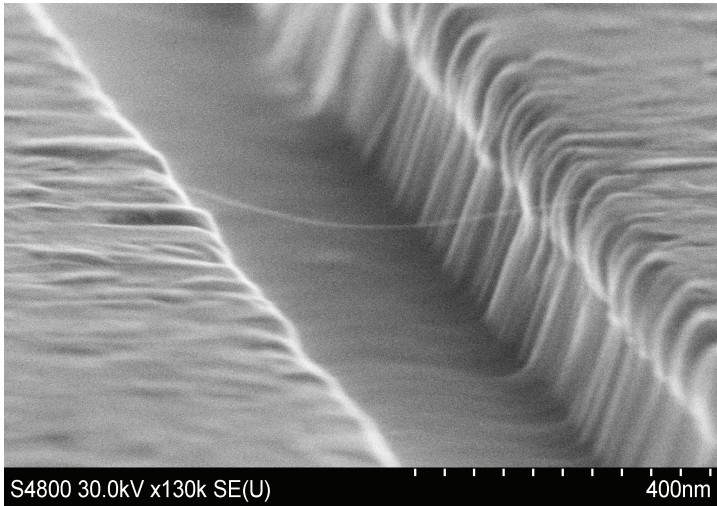


FIGURE 1.1: **Scanning electron microscope image of a suspended carbon nanotube**, the carbon nanotube is suspended across a 500 nm wide and 250 nm deep trench.

In our experiments, the string is replaced by a $1/1000$ mm long and ~ 1 nm thick tube of carbon (a carbon nanotube). As illustrated in Figure 1.1 the carbon nanotube is suspended between two metal contacts. This carbon nanotube oscillates similar to a suspended string. The frequency of a string is proportional to $\frac{1}{2L}$, where L is the length of the string. Since the length of the suspended carbon nanotube is much smaller than that of a piano string the resonance frequency is much higher. The resonance frequency of such a suspended carbon nanotube is not at a hearable frequency (~ 100 MHz). Our carbon nanotube resonators are placed in vacuum where no sound waves can travel to the ear. To hear or to detect the motion of the carbon nanotube we send electrons through it as it oscillates in an electric field. Once these electrons passed through the oscillating carbon nanotube,

they contain certain information about the mechanical motion. This is similar to the waves which travel from a piano string through the air before we hear a sound.

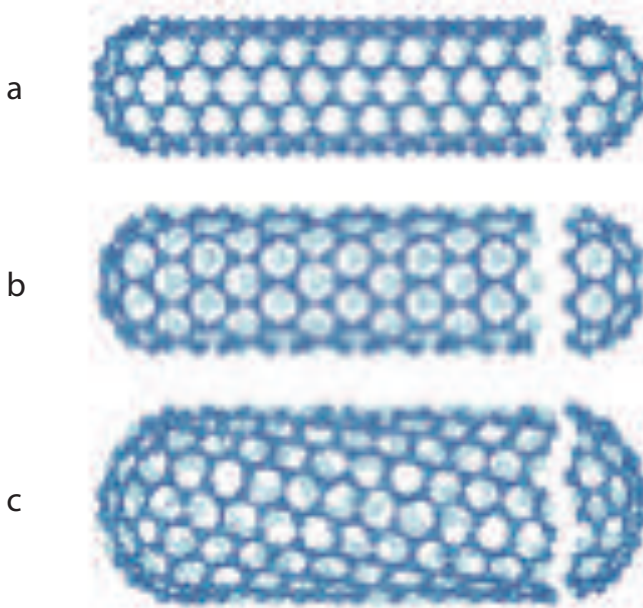


FIGURE 1.2: **Structure of a carbon nanotube** , (a) shows a so-called armchair carbon nanotube, (b) a zig-zag tube, and (d) a general chiral tube. (figure adapted from[1])

A single walled carbon nanotube (CNT) can be described as a graphene sheet rolled into a 1-2 nm thick cylinder with round spherical ends (Fig. 1.2). A CNT can be produced by a range of different methods; such as laser ablation[2, 3] ,arc discharge[4, 5] ,chemical vapour deposition (CVD)[6], or by PECVD[7]. By using enhanced chemical vapor deposition, CNTs with a length of 18.5 cm have been reported[8]. Figure 1.2 shows three different types of carbon nanotubes. The electronic properties of a single walled CNT vary from semiconducting to metallic, depending on how the graphene sheet is rolled up into a CNT[1]. The remarkable mechanical and electronic properties in the carbon nanotube arise from its strong inter-carbon-atom bonding and perfect crystalline structure.

Nanomechanical carbon nanotube resonators promise applications as mass[9, 10] and force sensors[11–13]. This is because a carbon nanotube can have a mass as low as $(5 \cdot 10^{-21} \text{ kg})$ per μm length and their stiffness makes them reach high

1 resonance frequencies (MHz to several GHz[14]). Furthermore they can achieve high mechanical quality factors[15] and by using a carbon nanotube either as a transistor or as a quantum dot, it is capable of detecting its own motion[16]. The mechanical resonance frequency and the non-linear shape frequency response of such a suspended carbon nanotube, strongly changes by a single electron tunnelling to the carbon nanotube[17, 18]. The high quality factors, high frequency and low mass of a carbon nanotube together with its strong non-linear behaviour, make it very interesting and challenging to put a carbon-nanotube resonator into the quantum ground state. But how to measure this?

Several schemes have been developed to measure the motion of a suspended carbon nanotube and are still not sensitive enough. Such scheme includes the use of a gate underneath the suspended carbon nanotube, to couple the oscillation of the carbon nanotube to its resistance in an electric field. Only for certain mechanical resonators, the quantum motion of a macroscopic objects has been explored. This was done by combining the mechanical resonator with a superconducting circuit or an optical setup[19–22]. However, previously a superconducting circuit has been used to measure the mechanical motion of a suspended beam[23], which is also suspended between two clamping points. To detect the mechanical motion, the mechanical beam resonator was embedded into one arm of the superconducting quantum interference device (SQUID). The SQUID couples the oscillation of the beam with a voltage measured across the SQUID in the presence of a magnetic field. Figure 1.3 shows a colorised scanning electron microscope image this SQUID.

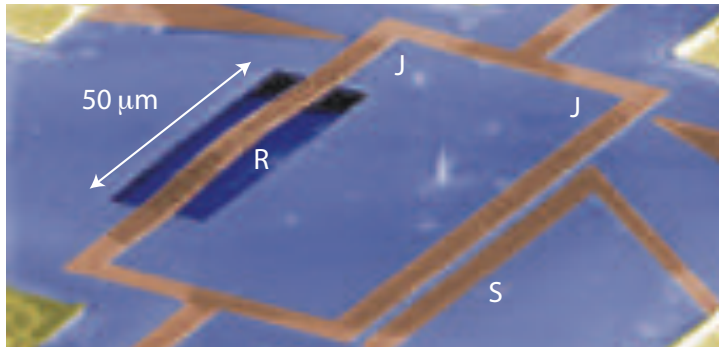


FIGURE 1.3: **The SQUID configuration used to measure a suspended beam** Colorised scanning electron microscope (SEM) image of the SQUID device. The SQUID is used measure the motion of a suspended beam resonator (R), it is sensitive to the amount of magnetic field lines passing through the loop (flux). As the resonator moves, it changes the area of the loop which then changes the flux. This change is then detected as a change in voltage across the SQUID. (Figure adapted from[23])

Using superconducting circuits to probe the mechanical motion of a CNT is an interesting and novel approach that is pursued in this thesis. Along the road we explore the possibilities and phenomena when combining a carbon nanotube resonator with superconducting contacts made of molybdenum rhenium. In **chapter 2**, the background for this thesis is given. It starts with a brief overview on previous methods used to detect the motion of a carbon nanotube. Then some background information, on quantum transport of electrons through a carbon nanotube in the Fabry-Pérot and Coulomb blockade regime, together with an reference map, to identify and to distinguish, different features in a measurement. Furthermore some theoretical background on superconducting Josephson junctions, SQUIDS and Andreev bound states in an carbon nanotube Josephson junction is given. **Chapter 3**, describes the fabrication of superconducting circuits with grown suspended carbon nanotube mechanical resonators. Three superconducting materials were tested to make such devices. The materials tested are Niobium-Titanium-Nitride, Rhenium and Molybdenum-Rhenium. The fabrication process, which was used to make the superconducting circuits with suspended carbon nanotube mechanical resonators is provided. **Chapter 4**, contains measurement results of DC-SQUID with suspended carbon nanotube junctions. We apply a Voltage to the gate, which displaces the suspended part of the carbon nanotube. This displacement is then coupled to the critical current of the SQUID with an applied magnetic field. which is then measured as a function of magnetic field and gate voltage. In **chapter 5**, we report an enhanced mixing signal which we observe in a suspended CNT-Josephson junction, without applying an magnetic field to the device. **Chapter 6**, contains measurement results of the mechanical ringdown of a suspended CNT. A high bandwidth readout-scheme, was used to detect the ringdown of a CNT at 2 K. In **Chapter 7**, we give an overview of the measurement data on the spectroscopy of CNT-Josephson junctions from different devices.

REFERENCES

- [1] C. Schoenenberger, *Band structure of graphene and carbon nanotubes: An exercise in condensed matter physics*, University of Basel (2000).
- [2] S. J. Henley, C. H. P. Poa, A. A. D. T. Adikaari, C. E. Giusca, J. D. Carey, and S. R. P. Silva, *Excimer laser nanostructuring of nickel thin films for the catalytic growth of carbon nanotubes*, *Appl. Phys. Lett.* **84**, 4035 (2004).
- [3] K. Y. Lim, C. H. Sow, J. Lin, F. C. Cheong, Z. X. Shen, J. T. L. Thong, K. C. Chin, and A. T. S. Wee, *Laser pruning of carbon nanotubes as a route to static and movable structures*, *Adv. Mater.* **15**, 300 (2003).
- [4] M. Keidar and A. M. Waas, *On the conditions of carbon nanotube growth in the arc discharge*, *Nanotechnology* **15**, 1571 (2004).
- [5] H. Lange, M. Sioda, A. Huczko, Y. Q. Zhu, H. W. Kroto, and D. R. M. Walton, *Nanocarbon production by arc discharge in water*, *Carbon* **41**, 1617 (2003).
- [6] L. Durrer, T. Helbling, C. Zenger, A. Jungen, C. Stampfer, and C. Hierold, *SWNT growth by CVD on Ferritin-based iron catalyst nanoparticles towards CNT sensors*, *Sensors and Actuators B: Chemical* **132**, 485 (2008).
- [7] M. Meyyappan, L. Delzeit, A. Cassell, and D. Hash, *Carbon nanotube growth by PECVD: a review*, *Plasma Sources Science and Technology* **12**, 205 (2003).
- [8] X. Wang, Q. Li, J. Xie, Z. Jin, J. Wang, Y. Li, K. Jiang, and S. Fan, *Fabrication of ultralong and electrically uniform single-walled carbon nanotubes on clean substrates*, *Nano Lett.* **9**, 3137 (2009).
- [9] K. Jensen, K. Kim, and A. Zettl, *An atomic-resolution nanomechanical mass sensor*, *Nature Nanotech.* **3**, 533 (2008).
- [10] J. Chaste, A. Eichler, J. Moser, G. Ceballos, R. Rurali, and A. Bachtold, *A nanomechanical mass sensor with yoctogram resolution*, *Nature Nanotech.* **7**, 301 (2012).
- [11] D. Rugar, R. Budakian, H. J. Mamin, and B. W. Chui, *Single spin detection by magnetic resonance force microscopy*, *Nature* **430**, 329 (2004).
- [12] C. A. Regal, J. D. Teufel, and K. W. Lehnert, *Measuring nanomechanical motion with a microwave cavity interferometer*, *Nature Phys.* **4**, 555 (2008).

- [13] O. Usenko, A. Vinante, G. Wijts, and T. H. Oosterkamp, *A superconducting quantum interference device based read-out of a subattoneutron force sensor operating at millikelvin temperatures*, Applied Physics Letters. **98**, 133105 (2011).
- [14] E. A. Laird, F. Pei, W. Tang, G. A. Steele, and L. P. Kouwenhoven, *A high quality factor carbon nanotube mechanical resonator at 39 GHz*, Nano Lett. **12**, 193 (2011).
- [15] A. K. Hüttel, G. A. Steele, B. Witkamp, M. Poot, L. P. Kouwenhoven, and H. S. J. van der Zant, *Carbon nanotubes as ultrahigh quality factor mechanical resonators*, Nano Lett. **9**, 2547 (2009).
- [16] V. Sazonova, Y. Yaish, H. Üstünel, D. Roundy, T. A. Arias, and P. L. McEuen, *A tunable carbon nanotube electromechanical oscillator*, Nature **431**, 284 (2004).
- [17] G. A. Steele, A. K. Hüttel, B. Witkamp, M. Poot, H. B. Meerwaldt, L. P. Kouwenhoven, and H. S. J. van der Zant, *Strong coupling between single-electron tunneling and nanomechanical motion*, Science **325**, 1103 (2009).
- [18] H. B. Meerwaldt, G. Labadze, B. H. Schneider, A. Taspinar, Y. M. Blanter, H. S. J. van der Zant, and G. A. Steele, *Probing the charge of a quantum dot with a nanomechanical resonator*, Phys. Rev. B. **86**, 115454 (2012).
- [19] K. C. Schwab and M. L. Roukes, *Putting mechanics into quantum mechanics*, Physics Today **58**, 36 (2005).
- [20] A. D. O'Connell, M. Hofheinz, M. Ansmann, R. C. Bialczak, M. Lenander, E. Lucero, M. Neeley, D. Sank, H. Wang, M. Weides, et al., *Quantum ground state and single-phonon control of a mechanical resonator*, Nature **464**, 697 (2010).
- [21] J. D. Teufel, T. Donner, D. Li, J. W. Harlow, M. S. Allman, K. Cicak, A. J. Sirois, J. D. Whittaker, K. W. Lehnert, and R. W. Simmonds, *Sideband cooling of micromechanical motion to the quantum ground state.*, Nature **475**, 359 (2011), ISSN 0028-0836, [1103.2144](#).
- [22] J. Chan, T. P. M. Alegre, A. H. Safavi-Naeini, J. T. Hill, A. Krause, S. Gröblacher, M. Aspelmeyer, and O. Painter, *Laser cooling of a nanomechanical oscillator into its quantum ground state*, Nature **478**, 89 (2011).

- [23] S. Etaki, M. Poot, I. Mahboob, K. Onomitsu, H. Yamaguchi, and H. S. J. van der Zant, *Motion detection of a micromechanical resonator embedded in a dc {SQUID}*, Nature Phys. **4**, 785 (2008).

2

BACKGROUND AND THEORY

2.1 CARBON NANOTUBE MECHANICS

Figure 2.1a is a scanning electron microscope (SEM) image, which shows a suspended CNT. A segment of the CNT is freely suspended between two metallic contact leads which are separated by a distance of 500 nm. This suspended nanotube segment can freely oscillate like a guitar string. The oscillation frequency is defined by the length over which the CNT segment is suspended. The CNT can oscillate in different mode shapes resulting in different resonance frequencies. Due to the high Young's modulus ($E = 1.2$ TPa) and its low mass density ($\rho = 1350$ kg/m³) [2, 3], the carbon nanotube easily reaches high mechanical resonance frequencies. For an 600 nm long CNT segment, we measured a resonance frequency of 300 MHz (Chapter 6).

The mechanical resonance frequency can be tuned by electrostatic forces, originating from a voltage difference between a gate underneath the suspended CNT and the CNT. In this situation, electrostatic forces are pulling the suspended CNT segment toward the gate which then changes its tension and thus alters its resonance frequency. (This effect is similar to tuning a guitar string by changing the tension in the wire.) Moreover because of this voltage difference the electric field present dopes the CNT with holes or electrons, changing its resistance. Figure 2.1b is measured by Ref. [1] by using a similar suspended CNT device. The figure shows the measured detected signal (colour scale) as a function of gate voltage (horizontal axis) and frequency (vertical axis). Resonance lines, which can be identified by peaks in the detected signal (extracted in the inset) are from the mechanical resonance. These lines show a clear frequency dependence with gate voltage. In our devices, we find that we can tune the mechanical resonance frequency of a 600 nm long suspended CNT from 300 MHz to 315 MHz by applying a voltage of 4 V to the gate.

One method to detect the mechanical motion of the CNT is shown in Fig. 2.2a, (adapted from [4]). In this method the CNT is driven with a radio frequency, while applying a gate voltage, sending a voltage through the CNT and measuring the current passing through it. When slowly stepping the drive frequency across the mechanical resonance of the CNT an increased change in measured current is detected. This method uses the strong change in CNT conductance as a function of gate voltage at low temperatures.

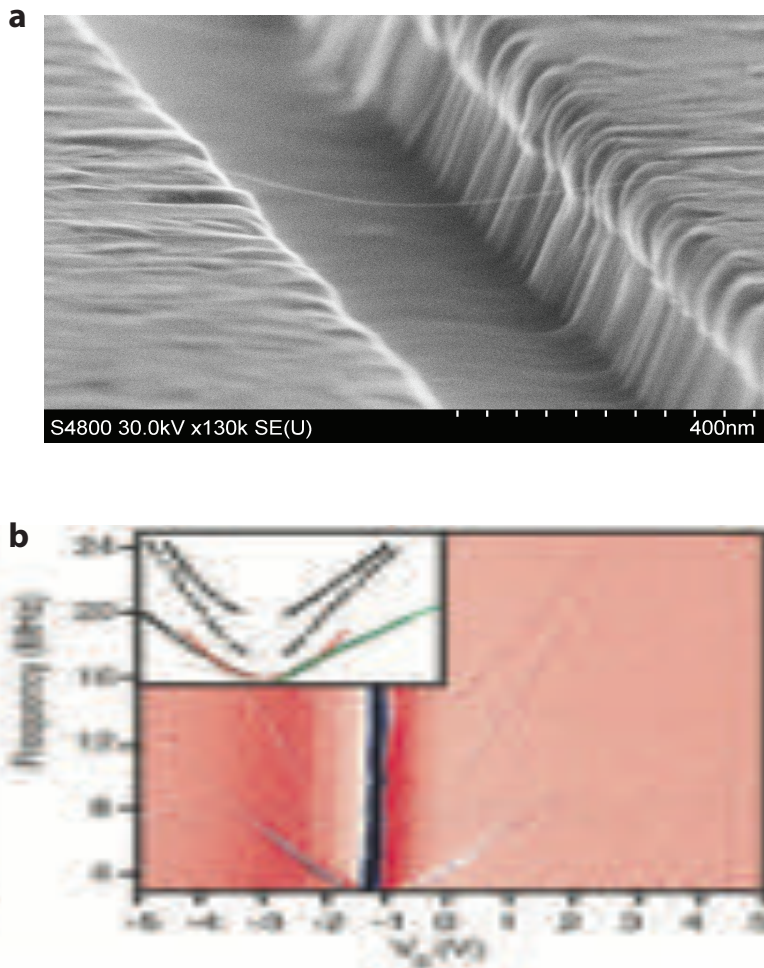


FIGURE 2.1: **A suspended CNT resonator and gate tune-ability with an electric field.** **a** SEM image of a Suspended CNT between two metal leads. **b** Gate tuneable mechanical CNT resonator. Measured mixing signal (colour) as a function of drive frequency and gate voltage. The inset shows the extracted positions of the CNT resonance. (Figure adapted from [1])

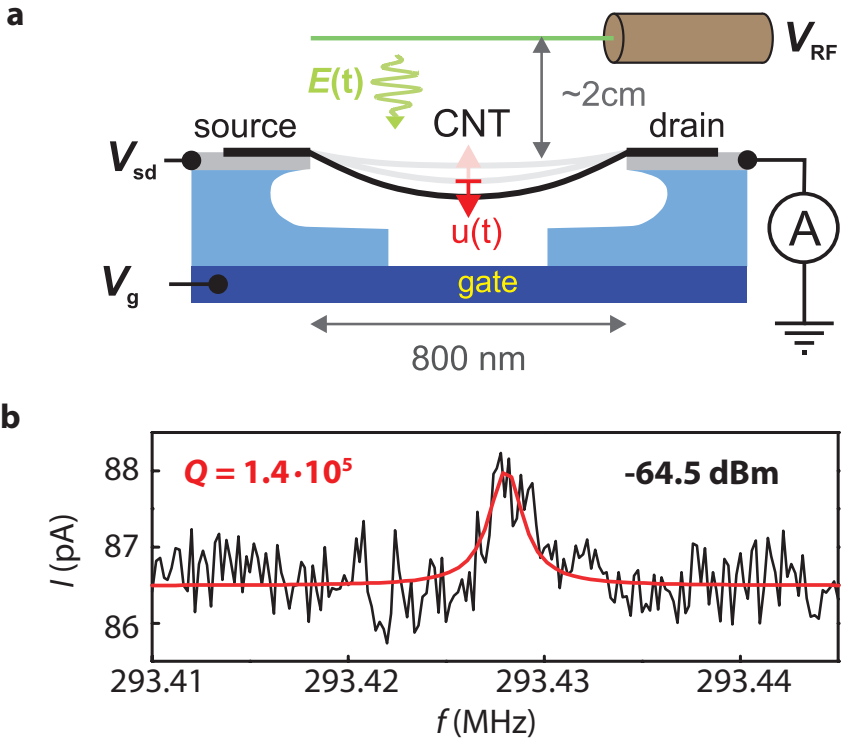


FIGURE 2.2: **DC readout scheme for a CNT with a high Q factor** **a** Measured current as a function of drive frequency through a high Q CNT device. (Figure adapted from [4]) **b** DC-rectification method scheme: A current passing through the device is measured as a function of bias voltage, gate voltage and applied drive frequency. (Figure adapted from [4])

Figure 2.2b shows the measured current passing through the CNT device (Ref. [4]) as a function of drive frequency. From the shape of the signal response a spectral Quality factor of $Q = 140000$ is obtained. These high mechanical quality factors are obtained by fabricating ultra clean CNT devices (Chapter 1). This high Q factor together with the low mass and high Young's modulus make CNT's excellent candidates to fabricate nanomechanical resonators with high sensitivity, quality factors and frequency.

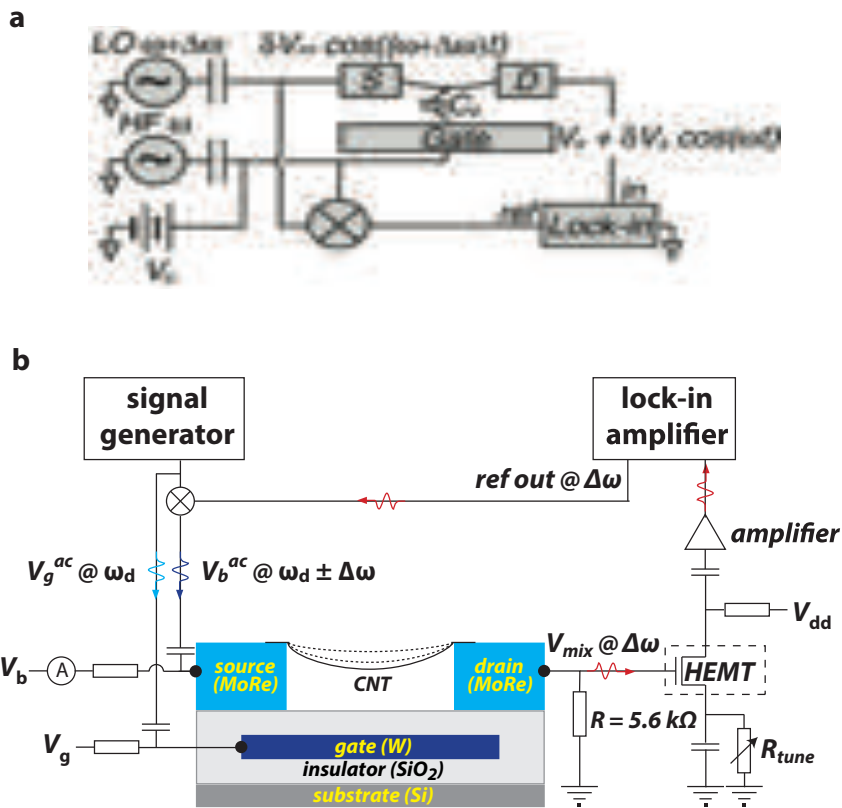


FIGURE 2.3: **AC readout schemes** **a** FM-mixing technique employs two signal generators and a lock-in amplifier to lock into a mixed signal which comes from the CNT. The CNT acts as a mixer, mixing the frequency from the gate and the source. (Figure adapted from [1]) **b** High bandwidth detection technique, is in principle similar to the FM-mixing technique. The key ingredient is, that it also incorporates a HEMT amplifier in close proximity to the CNT output, allowing to impedance match and to readout a mixing signal from the CNT with a high bandwidth. (Figure adapted from [5])

Another method to detect the CNT motion even at room temperature is shown in figure 2.3a (Ref.[1]). This method employs frequency mixing in combination with a Lock-in amplifier to detect the CNT motion (Ref.[1]). For this, two signal generators are used. One generates a frequency (HF) at resonance with the CNT and is applied to the gate. This frequency generator drives the CNT. A second frequency generator (LO) detuned from HF is applied to the source (input) of the CNT device. When the CNT is oscillating (i.e. when driven by HF), the CNT mixes its a

2

signal from its own mechanical oscillation with the input signal LO. This mixing happens because the conductance of the CNT changes with gate voltage. At the drain of the CNT device (output), the mixed signal is detected by a Lock-in amplifier. By externally mixing the LO with the HF a reference signal is generated for the Lock-in amplifier. As the Lock-in amplifier tracks the mixing response from the CNT, an additional a DC gate voltage is applied to tune the resonance frequency. This technique was used to generate Fig.2.1b.

The Fast readout method, shown in Fig. 2.3b was developed (by[5]) to increase the readout bandwidth available when measuring the oscillation of a CNT resonator. This was achieved by placing a high electron mobility transistor (HEMT) amplifier in close proximity to the drain (output) of the device. By doing so, a signal originating from the CNT is impedance matched with minor losses to 50Ω by the HEMT. The surrounding circuit is similar to the FM mixing method. Instead of using two signal generators, one signal generator is used to drive the CNT at the gate input. Additionally a reference output signal from a Lock-in amplifier is mixed with the signal generator to generate a probe signal, which goes to the source (input) of the CNT device. The CNT, mixes these signals into a signal which is then amplified by the HEMT and detected by the Lock-in amplifier.

An alternative method to detect the motion of a CNT, or DC displacement, is to embed the CNT into a DC superconducting quantum interference device (SQUID). A CNT would be suspended between two superconducting leads and act as a Josephson junction of the SQUID. This happens if the CNT can carry a proximity induced supercurrent from one superconducting contact lead to another. The displacement of the CNT is coupled to the amount of supercurrent passing through the DC-SQUID in the presence of a magnetic flux passing through the SQUID. This method is explained in section 2.3.2. The results of such measurements are presented in chapter 4.

2.2 QUANTUM TRANSPORT IN CARBON NANOTUBES

Let us consider a carbon nanotube which is suspended between two metallic contacts with a gate underneath (Fig. 2.4a). The two metal contacts are separated by a distance L from each other. A current passing through the CNT is measured as a function of gate-bias voltage.

In general carriers in the CNT segment are separated from the energy levels of the source and drain electrodes by tunnel barriers. A 1D schematic of this is shown in Fig. 2.4b. For electron doping, we can understand it as a PNP junction. For hole doping, there is still some scattering from the tunnel barriers at the edge of the suspended segment: the origin is not clear. In our devices we typically find that the tunnel barriers for holes have a relatively high transparency ($R_{CNT} \sim 6.5k\Omega$) (Chapter 4 and 7). One possible explanation for this is a Schottky barrier formation[6] due to the difference in the work function of the CNT and the contact metal. The nanotube segment is then isolated by two tunnel barriers from the source and the drain. Figure 2.4b, shows an energy diagram versus distance in the horizontal axis. E_F is the Fermi energy, and the nanotube segment is separated by two barriers from the source and drain.

Electrons are confined in a limited amount of space which results in an energy level spacing. The isolated nanotube segment has a length L and a diameter D which is typically 1.2 nm for a single walled CNT. Neglecting parabolic curvature of the bands from a possible band gap, we can estimate the level spacing from the longitudinal confinement, (the single particle energy level spacing) as:

$$\Delta_{SP} \approx \frac{hV_F}{2L}, \quad (2.1)$$

where the electron Fermi velocity in a metallic CNT is $V_F \sim 8.1 \times 10^5$ m/s[7] and $h = 6.63 \times 10^{-34}$ Js, is Planks constant. For our devices, the suspended CNT has a length of $L \approx 1 \mu\text{m}$ such that $\Delta_{SP} \approx 1.7$ meV. As a comparison, the energy level spacing from the confinement around the nanotube with a diameter of 1.2 nm is $\Delta_{sub-band} \approx \frac{hV_F}{2 \cdot (\pi d)} \sim 0.445$ eV, which corresponds to a wavelength of $\lambda_{sub-band} \approx 2.7 \mu\text{m}$ (which is a wavelength in far infrared). Since we work at Fermi energies $E_F \ll 0.4$ eV, we can neglect these higher subbands.

To understand the conductance of the nanotube as a function of gate and source-drain bias voltage we consider a capacitance model for the device shown in figure 2.4c. The nanotube segment is capacitively isolated from the source, drain and gate. It sees a tunnelling resistance to the source R_{TS} and to the drain R_{TD} . For simplicity we assume that both tunnel resistances are equal: $R_T = R_{TS} = R_{TD}$. We also ignore any other capacitances, for example to the environment or directly from the source to the gate or the drain.

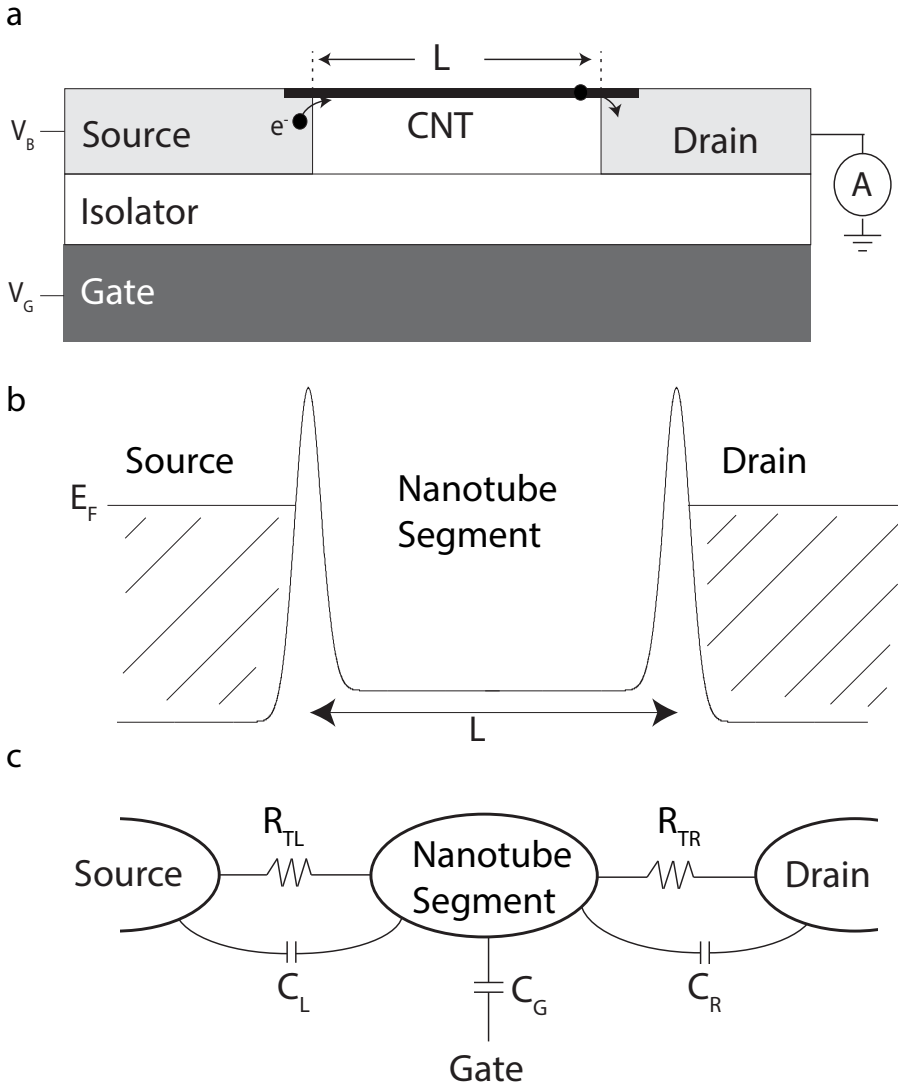


FIGURE 2.4: **Suspended CNT between two metal leads.** **a** Device sketch the suspended CNT, L is distance between the two contact leads. **b** Energy diagram of the suspended carbon nanotube segment. **c** Capacitance interaction model of the nanotube segment. R_{TL} and R_{TR} are the left and right tunnel-resistances to the segment from the source and drain respectively.

If we consider the suspended segment to be like an isolated metallic island, then the energy required to add one electron to this segment is equal to:

$$E_c = \frac{e^2}{2C}, \quad (2.2)$$

where C is its capacitance to the outside world. For our device, the capacitance of the nanotube segment is $C = C_S + C_D + C_G$, which is the sum of its capacitances to the source, drain and gate. In order to add one additional electron, the energy required is:

$$E_{add} = \frac{e^2}{C}, \quad (2.3)$$

which is valid assuming four fold symmetry of each single particle level and neglecting valley scattering and spin orbit coupling. For our devices, the typical capacitance is $C \approx 8.8$ aF such that $E_c \approx 9.1$ meV.

To measure charge quantisation in the device the thermal energy needs to be smaller than the charging energy E_c and the energy level spacing Δ_{SP} :

$$K_B T < E_c, \Delta_{SP} \quad (2.4)$$

,where K_B is the Boltzmann constant. Note that $K_B T < \Delta_{SP}$ only needs to be satisfied in order to observe quantisations at that energy scale (i.e. sequential or cotunneling lines). At 300 K $K_B T = 26$ meV, at 106 K $K_B T = E_{add} = 9.1$ meV and at 19.7K $K_B T = \Delta_{SP} = 1.7$ meV. This means that the temperature criteria is fulfilled at a temperature below 19.7 K. This can be done by cooling the device with liquid Helium (4 K).

The second requirement to observe charge quantisation is to have sufficiently high tunnel barriers. The time constant coming from the tunnelling resistance and the device capacitance $R_T \cdot C$, needs to be larger than the time associated with the energy uncertainty ($\Delta E \Delta t \sim \hbar$), where the energy is given by $\Delta E \sim E_{add}$. This results into a minimum tunnelling resistance, which is required to see discrete charge quantisation:

$$R_T \gg \frac{\hbar}{e^2} \approx 26 \text{ k}\Omega \quad (2.5)$$

Due to a difference in work-function of the CNT and the contact metal, a PN or NP junction is formed[6] at the metal CNT interface. For our devices, the CNT forms a PNP junction. By applying a voltage to the gate, the suspended nanotube segment can be doped with holes or electrons. So we can add or remove an electron from the CNT segment with the gate voltage. For a positive gate voltage the

device is a PNP-CNT junction, resulting in a high resistance measured across the device. In this case the resistance of the device is much larger than $R \gg 26 \text{ k}\Omega$, thus fulfilling the quantisation criteria if the device is also cooled down below 19 K. On the other hand if we apply a negative gate voltage we can dope the PNP junction into a PPP junction, resulting in a low resistance measured across the device. For our devices, we measured resistances very close to $6.5 \text{ k}\Omega$ when applying a negative gate voltage. This means we can use the gate voltage not only to add or remove electrons to the suspended nanotube segment but also tune it into and out of a charge quantisation regime.

2.2.1 FABRY-PÉROT REGIME:

We now consider transport through the nanotube when the tunnel barrier resistance is $R_T < h/e^2$, such that the conditions of charge quantisation are not fulfilled. Figure 2.5a shows a bias-gate voltage plot of the conductance measured in this regime by Ref. [8]. The figure shows a pattern which follows an oscillation with gate voltage. We refer to these as Fabry-Pérot oscillations, and the gate periodicity of these changes inversely with the length L of the nanotube segment [8].

In order to explain the nature of these oscillations, we look into what each electron sees when it travels from the source to the drain. For this we have to take the wave particle duality of an electron into account and see what happens to the electron wave in the carbon nanotube. This matters if the coherence length of an electron inside the carbon nanotube is longer than the nanotube itself. Since a CNT is a ballistic transporter, a clean CNT does little to disturb this electron coherence. The wavelength of the electron (λ_e) depends on the Fermi-velocity (V_F) inside the CNT. This Fermi velocity arises from the CNT band structure. ($V_F = \frac{1}{\hbar} \frac{\Delta E}{\Delta k}$ [9]) For a metallic CNT $V_F = 8.1 \times 10^5 \text{ m/s}$. It is important to note that the gate voltage changes Fermi-velocity V_F and thus λ .

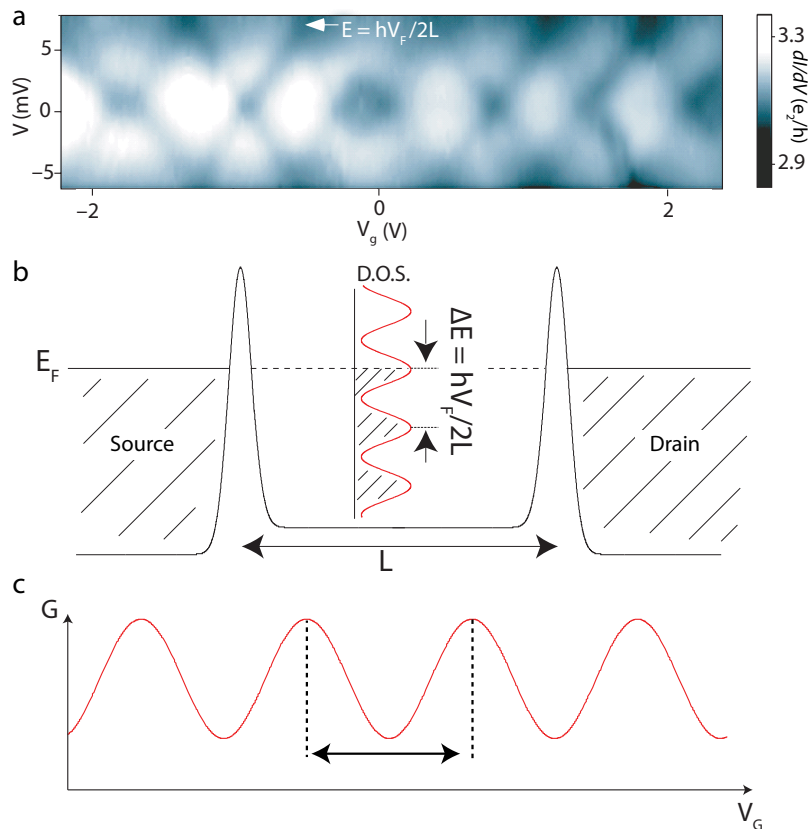


FIGURE 2.5: **Transport in the Fabry P erot regime.** **a** 2D Colour-scale differential conductance (dI/dV) plot as a function of voltage bias V and gate voltage V_g at 4 K. Device has a 220-nm long SWNT (not-suspended). The plot shows a semi-periodic pattern of dark lines. The voltage bias at which two lines intersect (white arrow) correspond to the energy scale ($E/e = V$). V_F is the Fermi velocity of the electrons. **b** Energy diagram and density of states (DOS) in the Fabry P erot regime. E_F is the Fermi energy level in the leads. **c** Cartoon showing conductance as a function of gate voltage in the Fabry P erot regime. (Panel **a** is adapted from [8])

Figure 2.5b shows an energy diagram with the two tunnel barriers at either side of the nanotube segment. An electron wave traveling from the source to the drain sees two successive barriers. These barriers act as two mirrors separated by a distance L from each other. Like in an optical Fabry-Pérot (FP) interferometer, where photons interfere, electron waves interfere with themselves as they pass through the nanotube segment. The condition for constructive interference upon transmission is when $(2L = n\lambda_e)$. As we change the gate voltage λ_e changes, such that we observe oscillations in the conductance.

(The free spectral range (*FSR*) of the conductance peaks with gate voltage (distance from peak to peak divided by the peak width[10]) increases with the electron reflectivity at the tunnel barriers. For our devices, *FSR* is often found to be around 2 with a tunnel resistance of $2 \cdot R_T \sim 6.5 \text{ k}\Omega$.)

As we change the gate voltage, we change the Fermi level in the CNT and this changes the electron wavelength λ_e . The density of states as a function of energy is reflected in the measured conductance measured as a function of applied gate voltage (Fig. 2.5c). From the constructive interference condition $(2L = n\lambda_e)$ we can derive an energy level spacing which is exactly the same as from equation 2.1:

$$\Delta_{SP} = \frac{\hbar V_F}{2L}. \quad (2.6)$$

This Δ_{SP} is the energy difference between two conductance peaks. The density of states (D.O.S.) as a function of energy in the nanotube segment is plotted in Figure 2.5b. We observe conductance oscillations with bias voltage following the density of states in the nanotube segment. Figure 2.5a shows a white arrow indicated a position where the dark lines criss cross the voltage bias corresponds to $\Delta_{SP} \sim 6.5 \text{ meV}$. The device has a trench size of $L \sim 220 \text{ nm}$ such that the calculated $\Delta_{SP} = 7.6 \text{ meV}$, which is close to the expected value. (The difference suggests that the nanotube segment is slightly larger than the trench size.)

2.2.2 COULOMB BLOCKADE REGIME

We now dope the device into an PNP or NPN junction with the gate voltage. Because of an increased barrier we observe a much higher resistance, such that both quantisation criteria are fulfilled: $R_T \gg 26 \text{ k}\Omega$ and $K_B T < \Delta_{SP}, E_C$. In this regime, we observe Coulomb blockade as a function of gate voltage. Figure 2.6a shows an example of a two dimensional colour map of the measured voltage as a function of gate and voltage bias by Ref.[11].

As in the previous plot we observe a periodic pattern along the gate axis. However, this the periodicity is different, the patterns looks like four diamonds which repeat with gate. As we tune the gate voltage we can dope/add electrons to the nanotube segment. Du to its structural nature the carbon nanotube has two energy levels K and K'.[7]. For now we, assume that both levels K and K' are degenerate and that no magnetic field is present near the CNT. As shown in Figure 2.6b, K and K' can contain 2 electrons, one spin up and one spin down, before both energy levels are filled. (In this figure K and K' are energy degenerate)

By tuning the gate voltage we, can dope the nanotube segment and add electrons or holes to it. Each time we, add one electron we observer a peak in the conductance (Fig. 2.6c). The energy required to add one electron depends if the K or K' levels are already filled with electrons for a particular energy level. If they are both filled the energy required to add one electron into the next higher energy level is $E_{add} + \Delta_{SP}$, where E_{add} is the addition energy and $\Delta_{SP} = \frac{hV_F}{2L}$ is the energy level spacing (Fig. 2.6b). The required change in gate voltage is $\Delta_{SP} V_G = \alpha(E_{add} + \Delta_{SP})$, where α is a coupling factor which relates the gate voltage to the Fermi level. For the case that K and K' have exactly the same energy level, the energy required to add each electron is E_{add} ($\Delta_{SP} V_G = \alpha E_{add}$) until K and K' are filled. Once K and K' are both filled with four electrons, this repeats itself, such that we would observe a four fold symmetry.

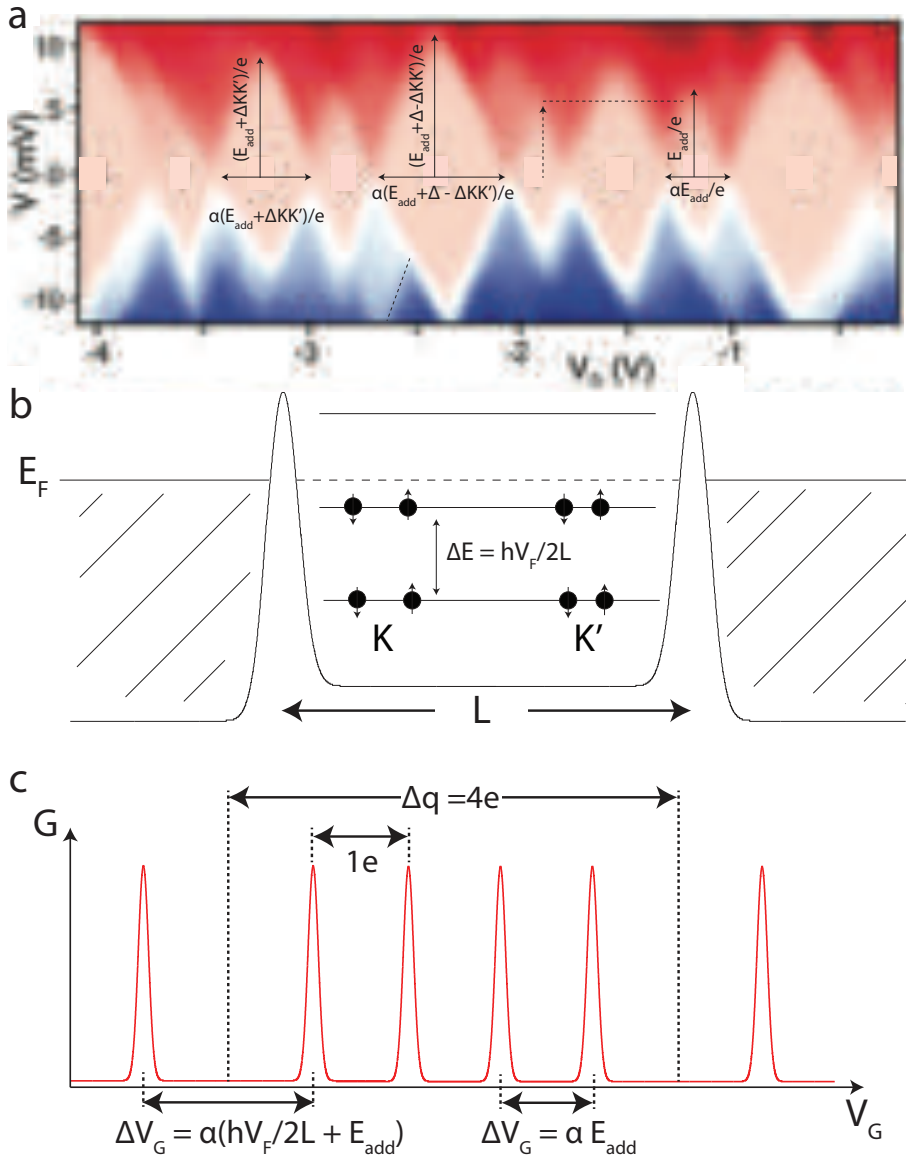


FIGURE 2.6: **Coulomb blockade of the current** **a** Colour map (dI/dV) versus gate voltage (V_G) and bias voltage (V), (data adapted from [11]) **b** Energy diagram and energy levels in the CNT. **c** Cartoon showing conductance as a function of gate voltage in the Coulomb blockade regime.

In typical experiments K and K' do not have the same energy level but are separated by an energy spacing of $\Delta_{KK'}$. This separation is because of spin-orbit coupling[12] and sometimes disorders in the nanotube segment. Due to this separation the energy required to add the third electron after the first 2 electrons occupy the first K level would then be $E_{add} + \Delta_{KK'}$. Once both K and K' are filled with electrons, the energy required to add one electron into the next higher energy level is then $E_c + \Delta_{SP} - \Delta_{KK'}$. This results into a pattern such as shown in figure 2.6a. Where a big diamond is followed by a small one, the two successive diamonds are different in size.

In figure 2.6a it is possible to estimate the addition energy E_{add} , single level energy spacing Δ_{SP} and the energy level difference between K and K' $\Delta_{KK'}$. The addition energy E_{add} is estimated from the small diamonds which follow the big ones. However since the two smallest diamonds in a set of four aren't equal in size we estimate the addition energy from the average size, which is $E_{add} \sim 5.5$ meV (Fig. 2.6a) Once the addition energy is known it is possible to obtain the energy splitting between the K and K' level from the next larger sized diamond. Here $E_{add} + \Delta_{KK'} \sim 8.7$ meV such that $\Delta_{KK'} \sim 3.2$ meV. From the biggest diamond it is possible to obtain the energy level splitting (Δ_{SP}), $E_{add} + \Delta_{SP} - \Delta_{KK'} \sim 11.25$ meV. So we get $\Delta_{SP} \sim 8.95$ meV, which is close to 9.3 meV the value expected for a 180 nm long tube. A more accurate estimate of these values was done by the author of the data set see Ref.[11].

The gate voltage V_G changes Fermi level. From the conductance we find that with an increased Fermi level the barrier height decreases. As the barrier height decreases, the tunnelling rate of electron from the source to the nanotube segment and then further to the drain increases. Due to this it is more likely that more than one electron tunnels at the same time on and of the nanotube segment and higher order events happen. A detailed explanation on what exactly happens during these processes is given by Ref.[13]. Figure 2.7 and 2.8 show experimental data, together with a cartoon schematics and a linecut. In the data and the cartoons important positions are indicated such that the individual features can be distinguished and characterised. Figure 2.7 is an overview of features seen for a low tunnel coupling i.e. when the gate voltage is low. There are two main features sequential tunnelling and co-tunnelling. Co-tunnelling is described as an inelastic tunnelling effect where a conductance feature appears at an energy E_{ex} inside the coulomb diamond. Figure 2.8 shows features such as Kondo peaks and co-tunnelling with peaks, which appear for a stronger tunnel coupling.

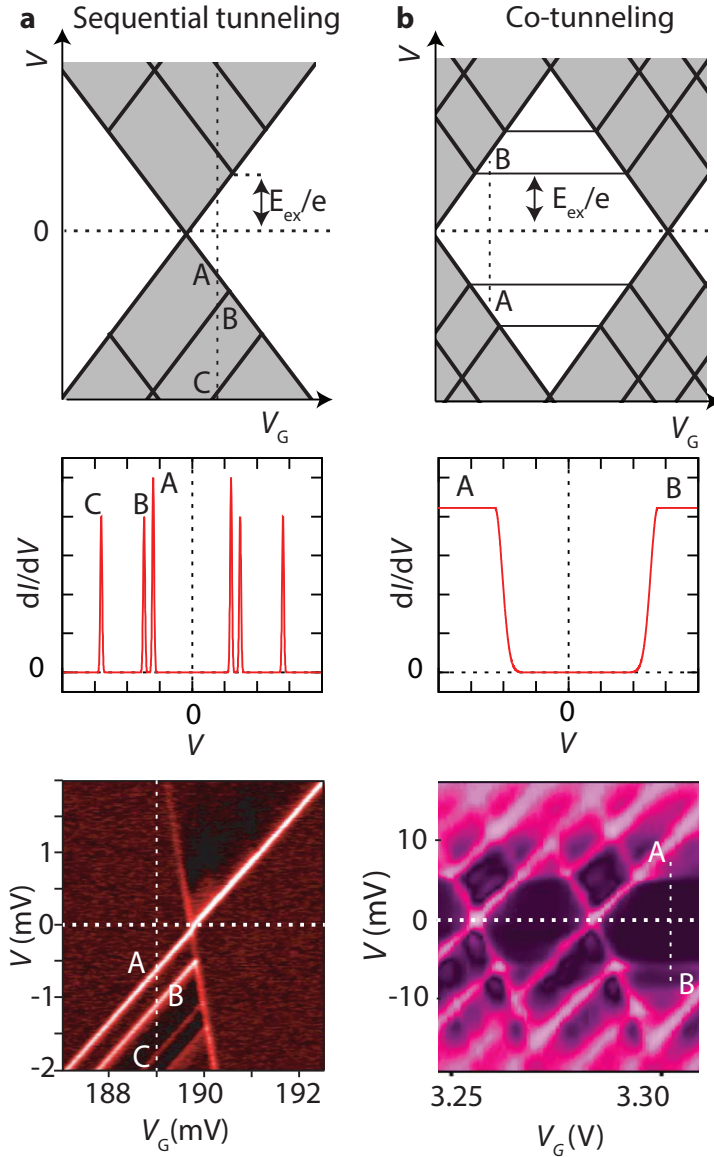


FIGURE 2.7: **Transport features in Coulomb blockade for weak tunnel coupling.** The top figures shows schematics of the differential conductance. The conductance peaks are indicated by black lines. **Middle figures** show a line cut along the vertical voltage bias axis (position indicated by the vertical dashed line in the schematic drawing above) Position of the peaks and positions are labeled and correlated with the schematic above. **The bottom figures show** experimental data at which such features were observed before. **a** Sequential tunneling (data adapted from from[12]). The voltage at which the first exited state enters the Coulomb diamond corresponds to the exchange energy. **b** Cotunnelling lines appear in conjunction with the sequential tunnelling lines at higher gate voltages (data adapted from[11]). Inside the diamond ridges (pos A and B) are then visible in the differential conductance line-cut.

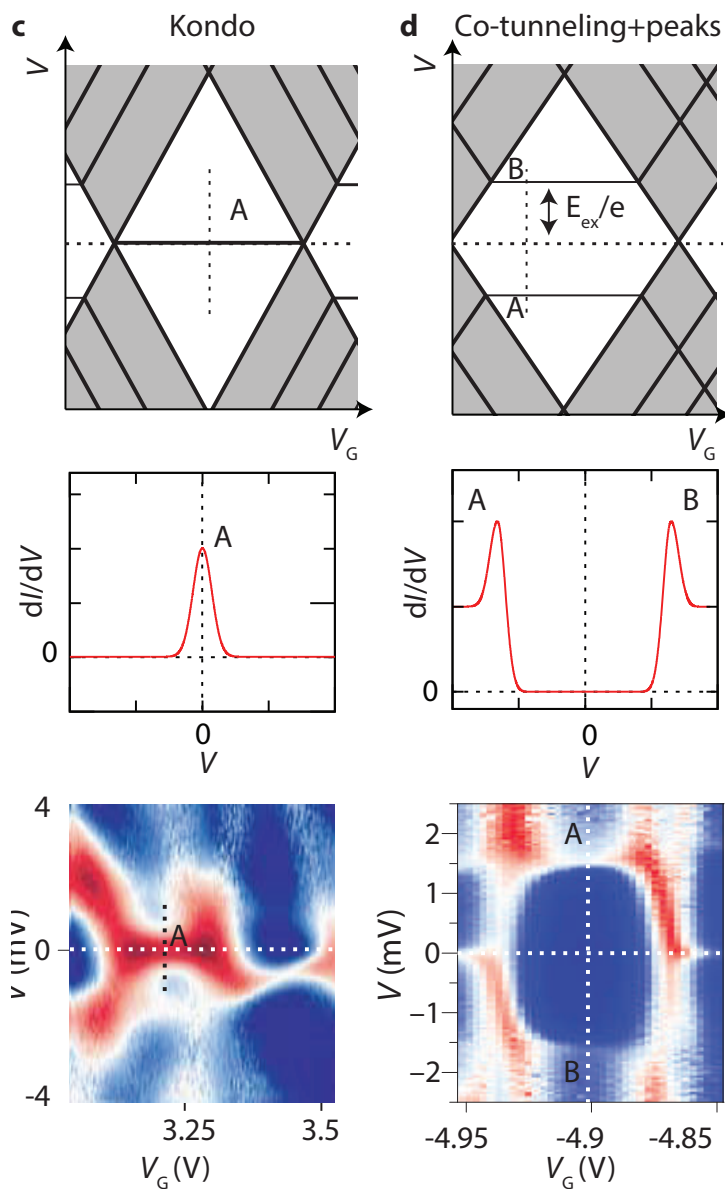


FIGURE 2.8: **Transport features in Coulomb blockade for stronger tunnel coupling.** These features are usually seen at higher gate voltages. **c** Kondo (data adapted from [14]). The Kondo effect is characterised by a clear peak at zero voltage bias. They appear in every second diamond. They are often surrounded by: **d** Co-tunnelling with peaks which appear in addition to the ridges (data adapted from [15]) In general we found that all our devices show this type of features instead of only co-tunneling lines.

2.3 SUPERCONDUCTING JUNCTIONS

The contact leads of our devices are made of an molybdenum rhenium alloy. This alloy becomes superconducting at dilution fridge temperatures (below 4.5 K). A CNT suspended between two of these superconductors have shown to form a Josephson junctions (JJ)[16]. In this configuration the device is a superconducting SQUID with two JJ in parallel, with a supercurrent of up to 30 nA going across both junctions in parallel.

2.3.1 JOSEPHSON JUNCTIONS

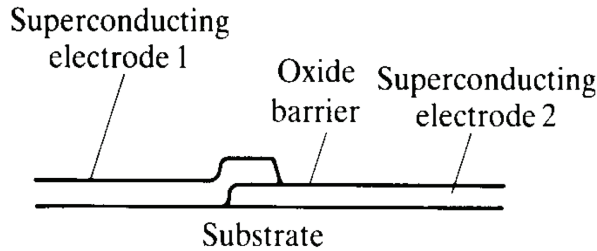


FIGURE 2.9: SIS josephson junction (Adapted from[17])

One of the most basic JJ is the SNS JJ which are two superconductors with a thin insulating material in between (Fig. 2.9). In this configuration the equations describing the current going through and the voltage across the junction are dependent on the phase of the superconducting wave functions on either side of the JJ[17]:

$$I_S = I_C \sin \Delta\phi \quad (2.7)$$

$$V = \hbar/2e \cdot \frac{d(\Delta\phi)}{dt}, \quad (2.8)$$

where the phase difference between the two superconducting wave functions are given by ϕ and Δ is the superconducting gap.

When considering a simplified JJ circuit where the JJ is in parallel with a resistor, we can describe such a system with a particle in a washboard potential. Using this description, equations 2.7 and 2.8, are best understood in the form of a cartoon (Fig. 2.10), showing a phase particle in a washboard potential. The horizontal axis represents the phase and the vertical axis the potential energy. The particle with mass m prefers to go downwards. The position of the phase particle along the x-axis describes is the phase of the JJ. As no current is applied the phase particle sits in the well. However as soon as a small current is applied to the junction which

is yet smaller than the critical current (I_C) of the junction no voltage is measured across the junction, however the phase of the junction changed. As soon as the current is larger than the critical current of the Josephson junction, the phase particle starts to roll downwards. When that happens the phase changes with time and as from equation 2.8 a voltage will be measured across the Josephson junction. (Figure 2.10)

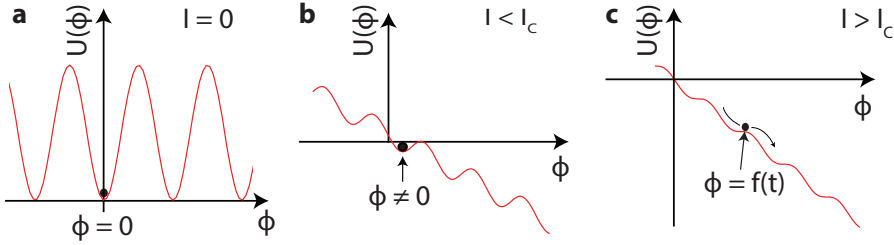


FIGURE 2.10: **Particle in a washboard potential** Any change in position of the phase particle results in a measured voltage across the JJ. **a,b**, ($I < I_C$), Phase particle sits in potential well, no voltage is measured. **c**, ($I > I_C$), Phase particle starts rolling downwards, a voltage is measured as the position of the particle changes. If the phase particle has a high enough momentum it may keep rolling across the potential, even when tilting the washboard back again (reversing the sweep direction to $I < I_C$). If this happens a voltage is measured even though $I < I_C$. Any shunted resistance, acts as a damper for the phase particle such that the phase particle would stop earlier.

The CNT-JJ has similarities to an SIS (superconducting-insulating-superconducting) Josephson junction. Due to the proximity effect of the superconducting, the transport of the supercurrent for a short distance across the the isolating or metal region is allowed. In such a setup an estimate of the $I_C R_N$ product of the SIS-JJ as a function of temperature has been worked out by Ambegaokar and Baratoff[18], which is given by:

$$I_C R_N = (\pi \Delta / 2e) \tanh(\Delta / 2k_B T), \quad (2.9)$$

where $\Delta = \frac{3.528}{2} K_B T_C$ is the superconducting gap for a superconducting with a critical temperature of T_C .

Proximity effect correction in a normal metal superconducting interface

Refinements to the proximity effect were done by Kulik and Omel'yanchuk[19]. These are for an superconducting-normal-superconducting (SNS) weak links, with a short metallic constriction, where a diffusive approximation is valid in the Ginzburg-Landau theory (two superconducting wave functions overlap across the constriction). In a way this sets a limit of how long a metal may be, such that a supercurrent

is transported. The length of the normal-metal coherence length is[17]:

$$\xi_n = \hbar V_F / 2\pi k_B T, \quad (2.10)$$

where V_F is the Fermi electron velocity and T is the operation temperature.

Carbon nanotubes however are one dimensional ballistic electron transporters (typical with a diameter of 1.2 nm). The electron coherence length of a CNT must be long because we observe Fabry-Pérot oscillations in the CNT-junction (Section 2.2.1). This makes it difficult to describe the CNT-JJ with such a model. A more adequate description of the CNT-JJ was done by[20]. A brief overview of this is given in section 2.3.3.

2.3.2 SUPERCONDUCTING QUANTUM INTERFERENCE DEVICE

The superconducting quantum interference device (SQUID) consists of two JJ in parallel. One can imagine /compare the SQUID to an optical interferometer, in which two beams interfere with each other. Figure 2.11 shows a SQUID. The SQUID separates two superconducting wave functions which interfere with each other. This interference happens along the SQUID loop. Inside the loop a circulating current builds up when the waves constructively interfere with each other. As this happens this circulating current consumes the remaining supercurrent that can pass through the SQUID. If both wave functions are exactly the same (i.e. if the SQUID has equal junctions on both sides and is free of any thermal noise and inductance) upon constructive interference I_C would be equal to zero. However if the SQUID does not have exactly equal JJ on both sides, the super-conducting wave functions do not fully interfere with each other, such that some remaining supercurrent can pass through the SQUID. This is comparable to an interferometer where two light beams only fully destructively interfere with each other if the frequency and amplitude are exactly equal.

As a current is circulating in the SQUID loop of are A in either direction, it generates a magnetic field through the loop of the SQUID. As a magnetic field is applied to the SQUID, this magnetic field interacts with the phase of the wave functions which are interfering with each other inside the SQUID loop. This is similar to changing the path length of one beam with respect to the other. The important factor is the magnetic flux going through the SQUID, meaning the product of the squid loop area time the magnetic field going through it. Thus a SQUID with a big loop is more sensitive to a change in magnetic field. Assuming we have two exactly equal wave functions; As the magnetic field changes, the critical current going through the squid changes with:

$$I_c = 2I_0 \cdot \left| \cos\left(\pi \frac{\Phi}{\Phi_0}\right) \right|, \quad (2.11)$$

where $\Phi = B \cdot A$, for a magnetic field with strength B and $\Phi_0 = h/2e = 2.07 \cdot \text{mT} \mu\text{m}^2$ is the superconducting flux quanta. In the presence of a static magnetic field, the flux through the SQUID can also be changed by changing the SQUID loop area and thus the critical current passing through the SQUID. This change in area of the SQUID loop can also origin from a small resonator embedded in the SQUID. The oscillation of the critical current passing through the SQUID as a function of magnetic flux is plotted in Fig 2.11b. The equations for non-equal squid-junctions, finite thermal noise and inductance in the SQUID are found in [21]. Figure Fig 2.11c shows the oscillations for such non-equal interfering wave functions.

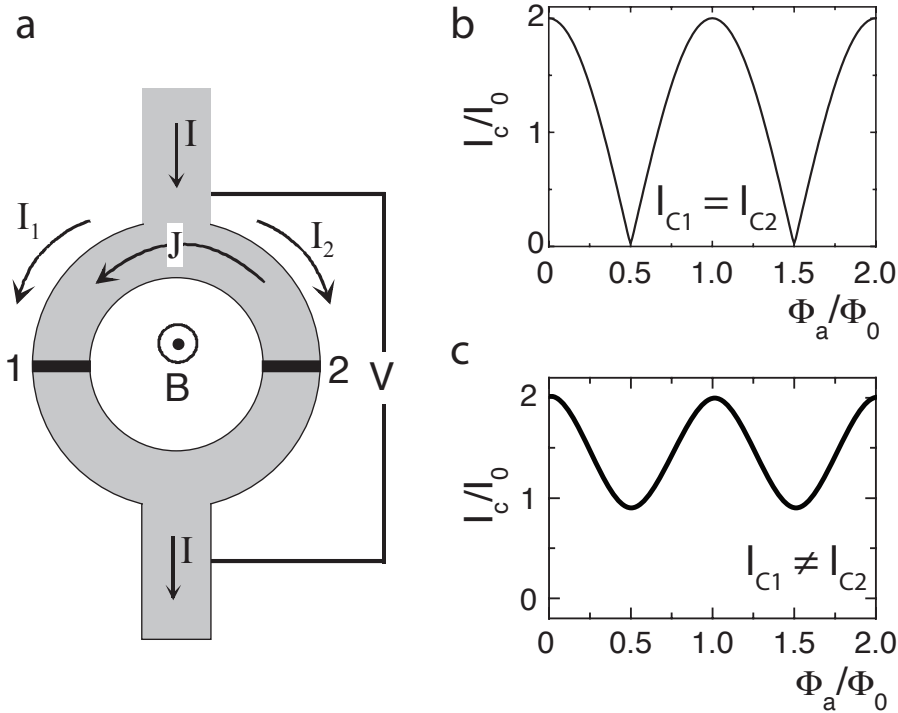


FIGURE 2.11: **Basic principle of a SQUID** a, A SQUID carbon with two JJ in paralel b, Critical current as a function of flux, with identical junctions without thermal noise and negligible SQUID inductance. c, I_c versus flux with non identical junctions, finite thermal noise and inductance in the SQUID. The oscillation was calculated by[21]. (all three figures are adapted from[21])

2.3.3 MICROSCOPIC FREE ELECTRON MODEL OF ANDREEV BOUND STATES IN A CNT JOSEPHSON JUNCTION

In this thesis we use the simplest model for a carbon nanotube coupled to metallic electrodes. In Fig. 2.12 we show an energy diagram for a CNT which is clamped between normal metal contacts and in the Fabry P erot regime. The Fermi energy level matches the FP SP energy level Δ_{SP} . An electron on this level is confined by the barriers at the two metallic-CNT interfaces. In this configuration we can think of two things the electron might do: a) the electron tunnels through one of the barriers into the leads or b) the electron reflects at the barrier. For the case that the electron is reflected, it gains a phase shift of π upon each reflection.

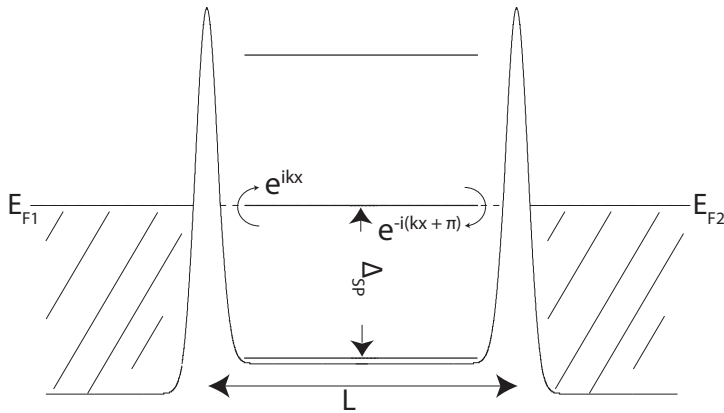


FIGURE 2.12: **Energy diagram sketch of a Normal metal CNT junction.** Level spacing is the FP SP energy level spacing Δ_{SP} . For the case that a SP energy level is aligned with the Fermi energy, the electron either reflects of the leads (small arrows) and obtains a π phase shift upon each reflection, or it tunnels into the metal leads.

Instead of a normal metal CNT interface we now consider a superconducting CNT interface. Figure 2.13 is a 1-D sketch for a case where the FP single particle energy level Δ_{SP} is away from the Fermi energy level and the superconducting gap 2Δ . Similar as before, electrons on those energy levels will reflect at the barriers with a phase shift of π (electron-electron reflections). Figure 2.14 shows a schematic, in which the FP SP energy level Δ_{SP} is within the superconducting gap window Δ and matches the Fermi energy E_F . For this situation we can think of two things that may happen. The electron is reflected as an electron plus a π phase shift at the barrier (electron-electron reflection). Or the electron tunnels through a barrier and is then reflected as a hole with a phase shift of Φ which is dependent on the electron energy and the superconducting gap (Andreev bound states).

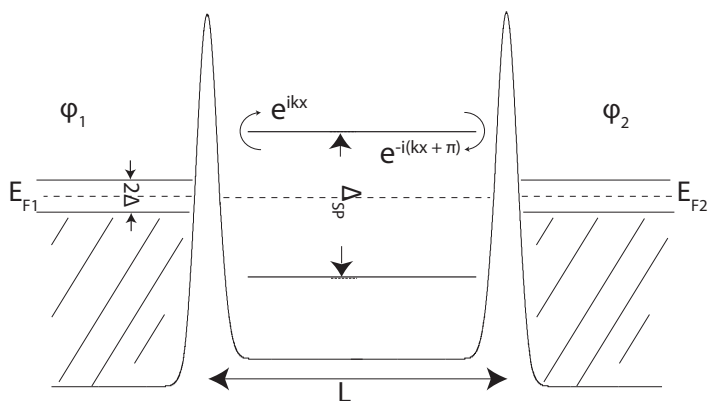


FIGURE 2.13: **Energy diagram sketch of a superconducting (S) S-CNT-S.** The FP SP energy level is outside the superconducting gap. Electron in these levels are reflected as electrons of the contact barriers with a π phase shift.

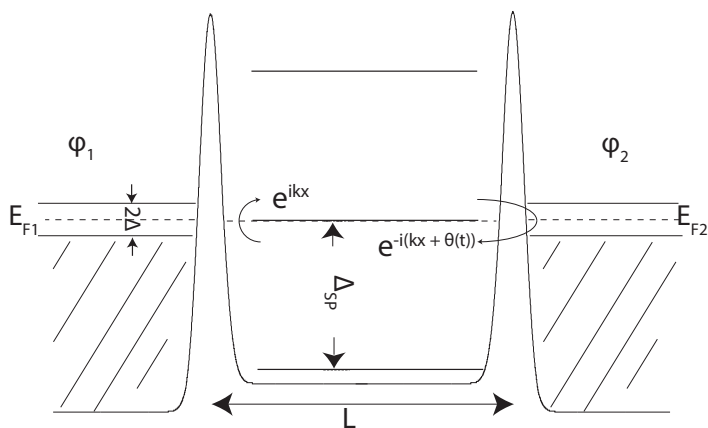


FIGURE 2.14: **Energy diagram sketch of a S-CNT-S junction.** A FP SP energy level is inside the superconducting gap. Electron which tunnel through the barrier may be reflected as holes with a phase shift of Φ . This phase shift is depending on the electron energy and the superconducting gap size Δ and the phase of the superconducting wave function in the leads. Electrons or holes may also reflect as themselves at the tunnel barriers and obtain a phase shift of π .

Experimentally a CNT-SC interface has been investigated using an on chip fabricated tunnel probe made by[20, 22]. The Fermi energy was probed by changing the bias voltage which changes the voltage bias window. The FP SP energy levels were probed by doping the CNT with holes or electrons. This was done by applying a voltage on the gate located underneath the CNT. Figure 2.15 is from[22], Fig. 2.15a and c show the experimentally acquired density of states (D.O.S.) (colour scale) as a function of gate voltage (V_{bg}) (horizontal axis) and energy (vertical axis). Fig. 2.15b shows modelled results using a model (described here[22]).

From the figures we can observe features such as white lines from the FP SP energy levels. As long as the SP level is outside the energy of the superconducting gap such as for the schematic in Fig. 2.13, we expect electrons to reflect at the tunnel barriers or tunnel through them directly into the SC-leads if the voltage bias window is large enough. We observe in Fig. 2.15a and c, alike features as for a CNT junction with normal metallic interfaces, for energies larger than the superconducting gap. However, as these white lines (from the SP energy level) enter energies of the superconducting gap (i.e. the energy is less than Δ) the features appear different as for a normal metal CNT junction. In this case we have a situation as described by Fig. 2.14, where the SP energy level in the CNT is within the energy of the superconducting gap. In this situation we get Andreev bound states together with barrier reflections. The energy can be described by the following equation[23]:

$$E_n = \pm\Delta\sqrt{1 - T_h^2 \sin^2\left(\frac{\phi}{2}\right)}, \quad (2.12)$$

where T_h describes the transparency of the barriers (eigenvalues of a matrix describing the transparency through the tunnel barriers), Δ is the superconducting gap and ϕ is the phase difference between the two electron density wave functions of the superconducting contacts.

In the case of Andreev bound states, electrons in the CNT are reflected as holes at the superconducting interface. The phase of the reflected hole depends on the phase of the superconducting wave function. And the phase determines if one obtains constructive or destructive interference across the S-CNT-S junction. Upon constructive interference one obtains a high current passing through (presence of an Andreev bound state), or upon destructive interference, no current passes through (No Andreev bound state present). The phase difference of two superconducting wave functions across the S-CNT-S junction depends on the applied current (as long as the current is smaller than the critical current of the junction this phase is stable) and upon a magnetic flux passing through a loop for the case of a SQUID. The device used by[20] had such a flux loop, such that the phase difference of the superconducting wave functions can carefully be tuned with a mag-

netic field. Figure 2.16a shows a schematic of the expected Andreev bound state energy position as a function of phase. Figure 2.16b shows the measured density of states (colour) as a function of flux (horizontal axis) and Energy (vertical axis). In these we observe brighter lines (higher density of states = presence of Andreev bound state) change in energy as a function of the phase (which was induced by a magnetic field).

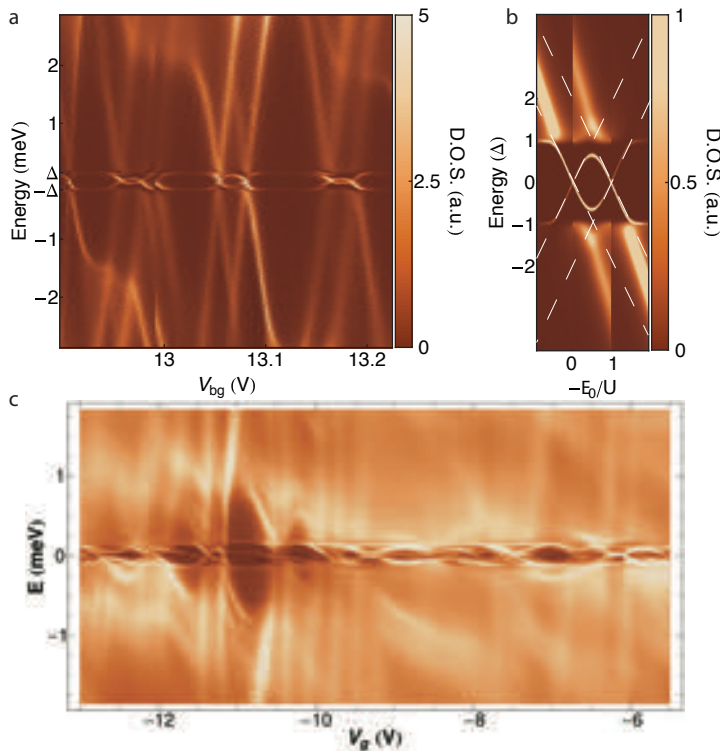


FIGURE 2.15: **Relation of Andreev bound states to resonant levels entering the bias window.** (figure adapted from [22])

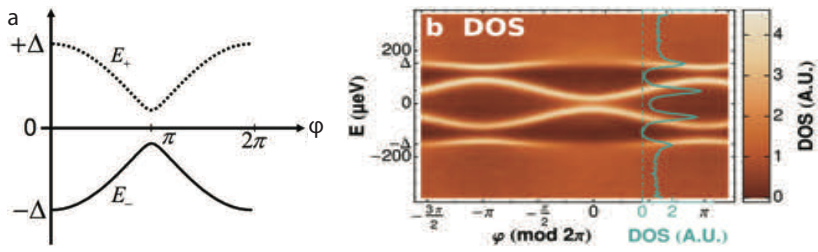


FIGURE 2.16: **Dependence of ABS energy on the phase across the superconducting junction.** (figure adapted from [22])

REFERENCES

- [1] V. Sazonova, Y. Yaish, H. Üstünel, D. Roundy, T. A. Arias, and P. L. McEuen, *A tunable carbon nanotube electromechanical oscillator*, *Nature* **431**, 284 (2004).
- [2] K. Jensen, K. Kim, and A. Zettl, *An atomic-resolution nanomechanical mass sensor*, *Nature Nanotech.* **3**, 533 (2008).
- [3] H.-Y. Chiu, P. Hung, H. W. C. Postma, and M. Bockrath, *Atomic-scale mass sensing using carbon nanotube resonators*, *Nano Lett.* **8**, 4342 (2008).
- [4] A. K. Hüttel, G. A. Steele, B. Witkamp, M. Poot, L. P. Kouwenhoven, and H. S. J. van der Zant, *Carbon nanotubes as ultrahigh quality factor mechanical resonators*, *Nano Lett.* **9**, 2547 (2009).
- [5] H. B. Meerwaldt, S. R. Johnston, H. S. J. van der Zant, and G. A. Steele, *Submicrosecond-timescale readout of carbon nanotube mechanical motion*, *Appl. Phys. Lett.* **103**, 53121 (2013).
- [6] R. T. Tung, *The physics and chemistry of the Schottky barrier height*, *Applied Physics Reviews* **1**, 11304 (2014).
- [7] C. Schoenenberger, *Band structure of graphene and carbon nanotubes: An exercise in condensed matter physics*, University of Basel (2000).
- [8] W. Liang, M. Bockrath, D. Bozovic, J. H. Hafner, M. Tinkham, and H. Park, *Fabry-Perot interference in a nanotube electron waveguide*, *Nature* **411**, 665 (2001).
- [9] K. Seeger, *Semiconductor physics: an introduction* (Springer, 2004).
- [10] G. Hernández, *Fabry-Perot Interferometers*, vol. 3 (Cambridge University Press, 1988).
- [11] S. Sapmaz, P. Jarillo-Herrero, J. Kong, C. Dekker, L. P. Kouwenhoven, and H. S. J. van der Zant, *Electronic excitation spectrum of metallic carbon nanotubes*, *Phys. Rev. B.* **71**, 153402 (2005).
- [12] F. Kuemmeth, S. Ilani, D. C. Ralph, and P. L. McEuen, *Coupling of spin and orbital motion of electrons in carbon nanotubes*, *Nature* **452**, 448 (2008).
- [13] J. M. Thijssen and H. S. J. van der Zant, *Charge transport and single-electron effects in nanoscale systems*, *Physica Status Solidi (b)* **245**, 1455 (2008).

- [14] P. Jarillo-Herrero, J. Kong, H. S. J. Van Der Zant, C. Dekker, L. P. Kouwenhoven, and S. De Franceschi, *Orbital Kondo effect in carbon nanotubes*, Nature **434**, 484 (2005).
- [15] J. Paaske, A. Rosch, P. Wölfle, N. Mason, C. M. Marcus, and J. Nygård, *Non-equilibrium singlet-triplet Kondo effect in carbon nanotubes*, Nature Phys. **2**, 460 (2006).
- [16] B. H. Schneider, S. Etaki, H. S. J. van der Zant, and G. A. Steele, *Coupling carbon nanotube mechanics to a superconducting circuit*, Sci. Rep. **2** (2012).
- [17] M. Tinkham, *Introduction to superconductivity* (McGraw Hill (New York), 1996).
- [18] V. Ambegaokar and A. Baratoff, *Tunneling Between Superconductors*, Phys. Rev. Lett. **10**, 486 (1963).
- [19] I. O. Kulik and A. N. Omel'yanchuk, *Contribution to the microscopic theory of the Josephson effect in superconducting bridges*, JETP Letters (USSR) (Engl. Transl.), v. 21, no. 4, pp. 96-97 (1975).
- [20] J. D. Pillet, C. H. L. Quay, P. Morfin, C. Bena, A. L. Yeyati, and P. Joyez, *Andreev bound states in supercurrent-carrying carbon nanotubes revealed*, Nature Phys. **6**, 965 (2010).
- [21] J. Clarke and A. I. Braginski, *The {SQUID} handbook*, vol. 1 (Wiley Online Library, 2006).
- [22] J.-D. Pillet, Ph.D. thesis, Université Pierre et Marie Curie-Paris VI (2011).
- [23] Y. V. Nazarov and Y. M. Blanter, *Quantum transport: introduction to nanoscience* (Cambridge University Press, 2009).

3

FABRICATION OF CARBON NANOTUBE SUPERCONDUCTING-CIRCUITS

This chapter describes the fabrication of superconducting circuits with as grown suspended carbon nanotube mechanical resonators. The aim is to combine the high quality carbon nanotube mechanical resonator, with the detection sensitivity of a superconducting quantum interference device (SQUID). To do this, we embed the suspended carbon nanotube into the SQUID, serving as both, a Josephson junction and a mechanical resonator. A proximity induced supercurrent, passing through the suspended carbon nanotube, needs to be large enough to allow electrical read-out of the nanotube motion, in the presence of a magnetic field. For this we need to find the right superconductor and fabrication method. In this chapter, we show that when the carbon nanotube is grown as the last step in fabrication and by using a Molybdenum-Rhenium (MoRe) superconducting alloy, high critical currents alongside a low contact resistance of the carbon nanotube to the MoRe can be achieved.

USING normal metal leads such as platinum, carbon nanotube (CNT) mechanical resonators of high quality have been reported.[1] The key issue in device fabrication is to grow the CNT as the final step in the fabrication. This results in defect-free CNTs often together with a high mechanical quality factor. In particular mechanical quality factors achieving 10^5 at cryogenic temperatures have been reported, which are much higher than in previous findings.[2] These clean CNTs are obtained by growing the CNT by chemical vapour deposition in a tube oven at 900°C after the normal metal electrodes have been deposited. To grow nanotubes in the final fabrication step, the metal leads, have to sustain the harsh conditions of the tube oven at 900°C , while subject to a flow of Ar, H_2 and CH_4 . Moreover, the materials involved should not hamper CNT growth.

To build a SQUID with a ultra-clean suspended CNT, a superconductor which can withstand the conditions in the oven is needed. The suspended CNT would then be the mechanical elements and the Josephson junctions of the SQUID. For a CNT-SQUID the coupling between mechanical motion and detector signal is proportional to the super current and the applied magnetic field.[3, 4] Therefore, a high supercurrent is beneficial and this can be achieved by decreasing the contact resistance of the CNT to the superconductor. By choosing a material, with a work-function, close to that of carbon we hope to achieve a lower contact resistance due to the Schotkey barrier. Finally, superconductors with a high-critical temperature (T_C) are preferred as their proximity induced superconductivity in the CNT is expected to be higher[5], possibly resulting in a higher supercurrent at the desired magnetic field ($\sim 1\text{ T}$).

3.1 SUPERCONDUCTING MATERIALS

3.1.1 NIOBIUM TITANIUM NITRIDE

Niobium Titanium Nitride (NbTiN) is a promising candidate to serve as superconducting electrode material as it is expected to withstands the a temperature of 900°C (needed for CNT growth) because of the high melt temperature of Niobium and Titanium.[6] It has a T_C of 15 K [7]; We estimate the work-function to be between that of Niobium (4.19 eV [8]) and of Titanium (4.1 eV [9])[10, 11]; Any value between these is at least 0.8 eV below the work-function of a CNT which is $4.9 - 5.1\text{ eV}$ [12]. We have tested the suitability of this superconductor for contacting clean CNTs by fabricating test structures and subject them to the conditions in the oven that is used for CNT growth.

Device fabrication started with thin-film magnetron sputtering of NbTi in nitrite and argon gas on a Si/SiO_2 wafer with a 500 nm thick SiO_2 layer. The target sample stayed at room temperature during the sputtering process. The $p++$ doped Silicon can be used as a back-gate. Electron beam lithography (EBL) was done with

a 500 nm thick positive resist layer ZEP 520A on NbTiN. Dry etching of the NbTiN and of 100 nm SiO₂ was performed with a BCl₃ and He plasma dry etch. In this step the self aligned trenches are formed as-well. The EBL resist was then removed with a resist stripper and boiling acetone. Etch remains were removed with ammoniac and IPA. Subsequently an organic iron catalyst used for CNT growth was deposited close to the trench. The catalyst is a mixture of 30 ml Methanol, 30 mg Aluminium oxide, 40 mg (Fe(NO₃)₃ 9H₂O) Ferric nitrate Nona-hydrate and 9 mg MoO₂(acac)₂. Catalyst liftoff was done using EBL with a 225 nm/100 nm thick PMMA 495K/950K

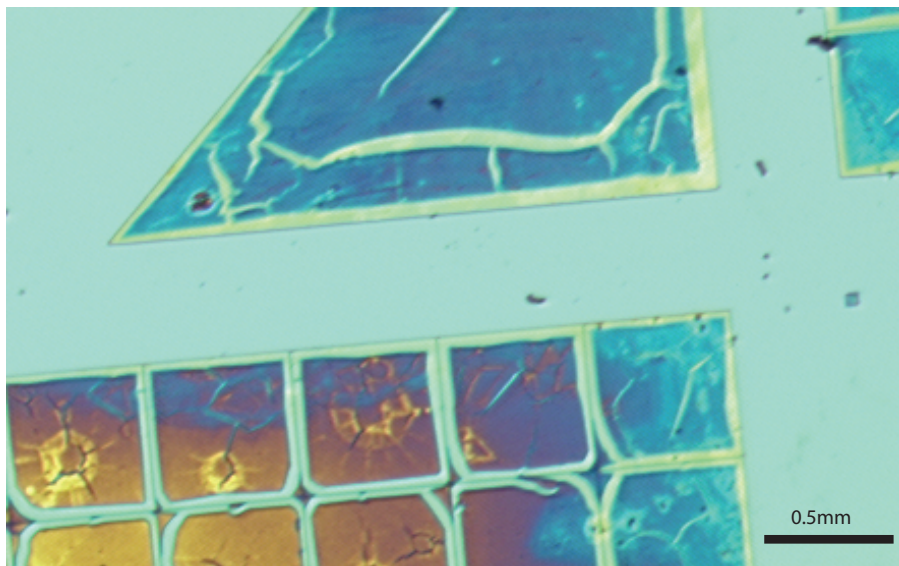


FIGURE 3.1: Optical image of NbTiN on SiO₂ after placing it in the CNT oven and subjecting it to the CNT growth conditions. The NbTiN appears dark blue and yellow with cracks on top.

bilayer. Before deposition, the catalyst was sonicated for 30 minutes and the sample exposed to Oxygen plasma (100 W, 350 μ bar) for 30 seconds. After deposition, once the catalyst has dried on the chip it was placed on a hotplate for 30 minutes. Then the sample was held in Acetone (55 ° C) and sonicated (weak sonication) for 20 seconds and immediately blown dry with nitrogen. This catalyst resist-liftoff procedure is critical to avoid catalyst contamination or accidental removal.

The sample is then placed in the oven to grow CNTs. In the oven a flow of Argon (1.5 l/min) is used while warming the sample to 900 ° C within 30 minutes. Then, a Hydrogen flow (700 ml/min) is activated without Argon for 10 minutes. Subsequently, CNT growth is started by adding a Methane flow (600 ml/min)

which is for 10 minutes sustained at 900 ° C after which the CNT growth is completed. Within 45 minutes the sample cools down to room temperature in Hydrogen (700 ml/min). Some CNTs are expected to grow from the catalyst across the trench and make contact to the underlying superconducting leads.

Figure 3.1 shows an optical image of a fabricated device after the CNT-oven was used. The superconducting film on the bottom left appears as yellow and dark blue square structures with cracks on top lying on the Silicon oxide (light blue). The colour of the NbTiN film thus changes across the sample from yellow to blue after it was placed in the oven. We found that this colour change was reduced with increased H₂ flow, by sealing leaks at the inlet of the CNT oven, by changing the recipe such that warmup of the sample happens in Hydrogen (700 ml/min) instead of Argon, and by dedicating gas flows sole for the CNT oven (minimise chances of leaks on lines). The colour change of the NbTiN film and the required methods to reduce this colour change, however indicates that NbTiN is highly sensitive to Oxygen at higher temperatures. Although Nb can form hydrides [13], tests with annealed NbTiN in H₂ showed that this was not playing a role here.

CNT growth also appeared to be affected as only a 1% yield of suspended CNT was observed, much lower than the yield when using the standard recipe with Tungsten Platinum. Nevertheless a few working devices were fabricated and electrical characterisation could be performed. Figure 3.2 shows a two-terminal room-temperature (RT) measurement of a CNT at three different bias voltages. A zero and negative bias voltage is used to check for gate leakage across the insulating SiO₂ between the gate and the electrodes. The device in Fig. 3.2 has a resistance of 25 MΩ at a positive gate voltage of 40 V, a value which is much larger than the quantised conductance indicating high tunnel barriers at the contacts. Summarising, the colour change of the NbTiN film after growing CNTs and the high contact resistance indicate that NbTiN is not the superconductor we are looking for.

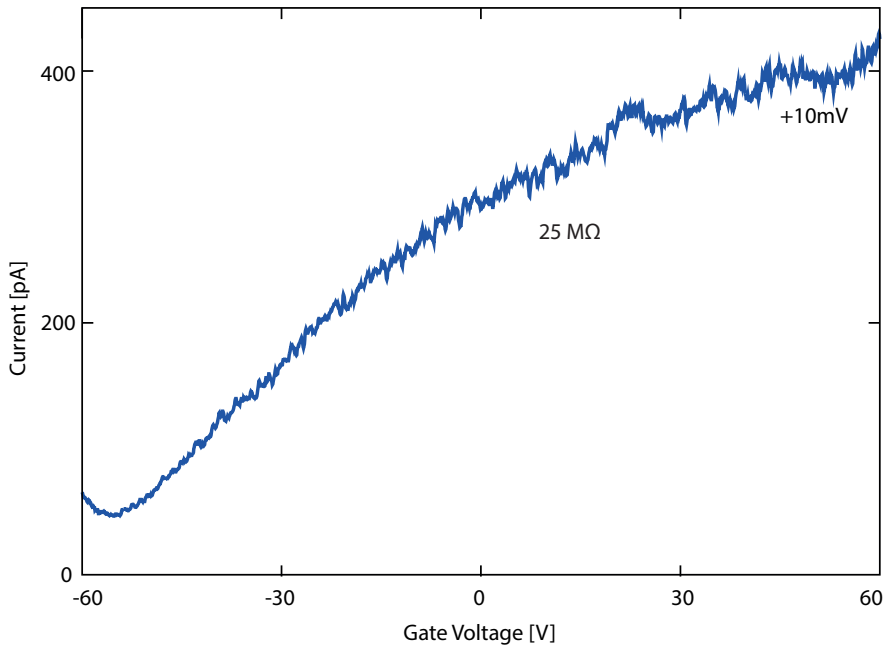


FIGURE 3.2: Current versus to gate voltage at three different voltage biases indicated near the curves for a suspended CNT with NbTiN electrodes measured at room temperature. A 0 mV and a -10 mV bias voltage is used to test for gate leakage across the nm thick SiO_2 to the electrodes.

3.1.2 RHENIUM

Rhenium is a rare earth material and a superconductor at cryogenic temperatures. It was successfully used by others in our department to contact CNTs.[14] Its T_C of 1.69 K[15] is considerably lower than that of NbTiN but the work-function is 4.8-5 eV[16], which matches that of a CNT well. A lower Schottky barrier and contact resistance are therefore expected in comparison to NbTiN.

We have again tested the suitability of this material in a similar way as described for NbTiN. Devices with rhenium were made according to the following procedure (see also Fig. 3.3); A Si/SiO₂ wafer which has a thinner 285 nm thick SiO₂ layer has, however, been used to obtain a stronger electrostatic gate coupling to the CNT. A 100 nm thick Rhenium (99.96 % purity) layer was first magnetron sputtered in the presence of 2×10^{-3} mbar Argon gas (Fig. 3.3a). Self-aligned trenches were made by using a four-layer resist mask. The four-layer resist mask, (see Table 3.1) consists of 200 nm PMMA950K, 700 nm hard baked S1813, 7 nm Tungsten and 200 nm PMMA950K on top. After developing, the EBL mask was formed by plasma etching of the Tungsten layer using 12.5 SCCM SF₆ and 10 SCCM He, followed by plasma etching of S1813 and PMMA with 20 SCCM O₂. While oxygen plasma does not etch tungsten the S1813 and the PMMA are non-isotropically etched. The PMMA serves as a liftoff layer while the hard-baked S1813 has a low etch-rate for dry etching. This mask makes it possible to obtain very high aspect ratios for dry etching while keeping the precision of top resist layer. Furthermore the four layer mask can be removed by sonicating the sample in warm acetone, thus avoiding chemicals which may potentially damage or alter the superconducting metal. Bond-pad electrodes and self aligned trenches are formed by continued etching of 100 nm Rhenium and of 200 nm SiO₂ with SF₆ and He (Fig. 3.3b,c). After removing the resist mask, catalyst was deposited and CNTs were grown using the same method and settings as for the NbTiN devices (Fig. 3.3d-f).

At room temperature two-wire electrical measurements exhibited a 70% yield of devices having a CNT; 30% of those had a resistance of 10-50 K Ω . The high yield of potential devices and low-contact resistance make this material a good candidate for fabricating superconducting CNT resonators.

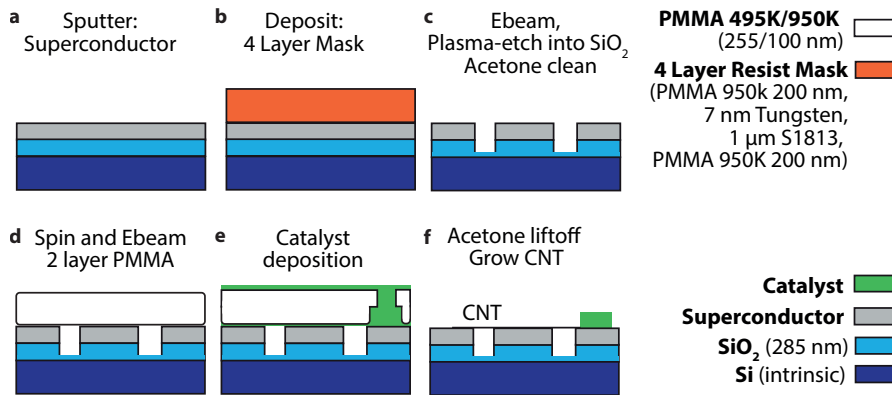


FIGURE 3.3: Fabrication overview of a CNT-Squid with self-aligned trenches. The superconductor used is 115 nm Rhenium when testing Rhenium devices. A bilayer of co-sputtered Molybdenum and Rhenium each 40 nm is used when making devices with Molybdenum Rhenium.

4-Layer Mask	Etch
Spin PMMA 950K 4000 rpm (200 nm) 100°C 30 min and 180°C 1 min	Develop after Ebeam MIBK(1):IPA(3) 90 sec IPA 90 sec
Sputter W (7 nm) 50 μbar 150 W RF 15 s	SF_6 (12.5 SCCM) + He (10 SCCM) 10 μbar 45 W ($V_B = -320$ V) 18 sec + 3 sec (overetch)
Spin S1813 5000 rpm (700 nm) 120°C 10 min and 180°C 30 min	O_2 (20 SCCM) 4 μbar 50 W ($V_B = -450$ V) 15 min
Spin PMMA 950K 4000 rpm (200 nm) 180°C 30 min	O_2 (20 SCCM) 4 μbar 50 W ($V_B = -450$ V) 2 min + 5 min (overetch)

TABLE 3.1: Overview of the four Layer etch mask. This mask can be used to etch into thick metal and SiO_2 while having the high precision on PMMA and keeping an high aspect ratio. For the the top layer instead of PMMA950L, a positive 200nm thick NEB22 resist can be used. NEB22 requires a much lower electron beam dose than PMMA950K such that exposure does not damage the bottom PMMA layer.

3.1.3 MOLYBDENUM-RHENIUM

In search of a superconductor with a higher T_C than Re, we started to look at MoRe alloys. For example, $\text{Mo}_{38}\text{Re}_{62}$ has a T_C of 15 K when deposited at 1225°C [17] as a bulk material. The work function of Molybdenum is 4.36 - 4.95 eV, again close to that of a CNT. [18] Also for this material test devices have been made to assess the suitability for contacting CNT resonators. Sample fabrication follows the same procedure as for Rhenium. Instead of sputtering 100 nm of Rhenium, first a 40 nm Rhenium layer is deposited by magnetron sputtering. Additionally a Molybdenum layer of 40 nm is then magnetron sputtered in argon gas at $20 \mu\text{bar}$ and a power of 100 W. The four layer resist mask (Table 3.1) is then used to etch bond-pads, electrodes and self aligned trenches. It is expected that after catalyst deposition the Mo and Re in the two separate layers subsequently alloy due to the diffusion length of a metal at 900°C . [19]

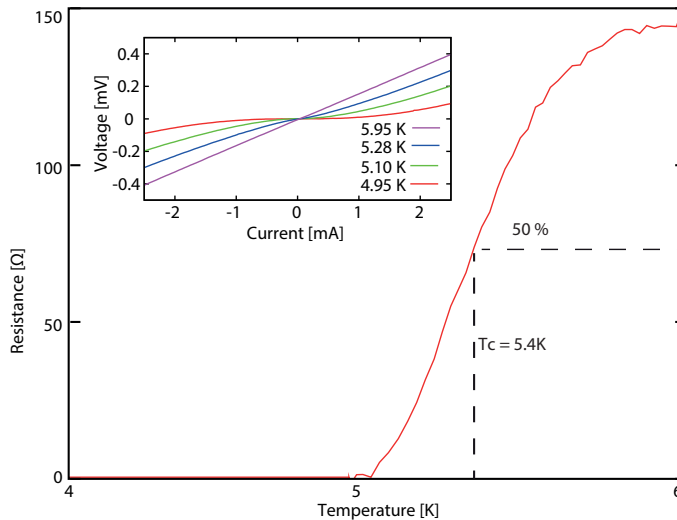


FIGURE 3.4: Four-terminal Resistance Ω of a MoRe bulk film as a function of temperature measured at a current bias of 2 mA on a 40/40 nm MoRe film after being exposed to the CNT oven conditions (900°C in hydrogen flow of 700 ml/min for 1 hour and methane flow of 600 ml/min for 10 minutes). The dimensions of the Molybdenum Rhenium sheet are $500 \mu\text{m} \times 170 \mu\text{m} \times 80 \text{ nm}$ thickness, four aluminium wires were wire-bonded on this sheet. Inset: Four-terminal Voltage versus current bias across the MoRe film at different temperatures.

To test this, we have characterised films that were placed in the oven by four-terminal resistance measurements. The data (Fig. 3.4) show that the resulting film is a superconductor with a T_C of 5.5 K. A T_C of 5.5 K indicates that the film has

formed an alloy as the T_C of Mo equals 0.9 K and that of Re 1.6 K [15].

The measured superconducting T_C 5.5 K is below the optimum of 15 K. This is likely due to the non optimised ratio and deposition temperature of Molybdenum and Rhenium [20]. Molybdenum was sputtered in a different machine as Rhenium, and the machine with the Rhenium target is also used for Chromium evaporation. Chromium could be adding magnetic impurities in Rhenium, which lowers the T_C of the superconductor. Another possibility is that we have not achieved the optimal ratio of Mo and Re in the film. The T_C of MoRe is expected to be dependent on the film thickness as rhenium and molybdenum films show dependence of thickness. [21, 22] However, previous experiments encompassing thin MoRe films report a T_C higher than 5.5 K. [23, 24] Very thin films of MoRe (4 nm thick) used for single phonon detection were reported to have a T_C of 7.7 K. [25]. MoRe films with a thickness on the order of 20 nm thick had a T_C of 8.5 K [24], 500 nm thick films a T_C of 13.5 K [20]

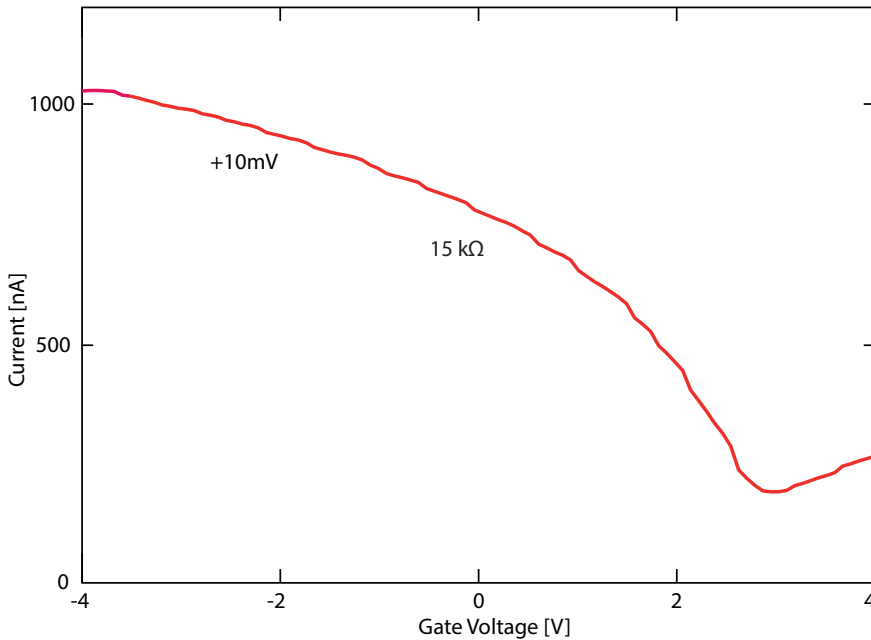


FIGURE 3.5: Current versus gate voltage for a suspended CNT with MoRe electrodes at three different bias voltages indicated near the curves measured at room temperature. A 0 mV bias is used to test for gate leakage across the 285 nm thick SiO₂. The resistance is about 15 kΩ.

At room-temperature the two-terminal electrical measurements across the devices exhibit the same high yield and low contact resistance as for Rhenium (see Fig. 3.5). The catalyst is displaced $1.2 \mu\text{m}$ away from the trench to ensure good electrical contact of the CNT to the MoRe. Even though, the number of CNTs grown from the catalyst is not fixed as visible in Fig. 3.6 the distance from the catalyst to the trench can be varied to optimise the yield of working devices.

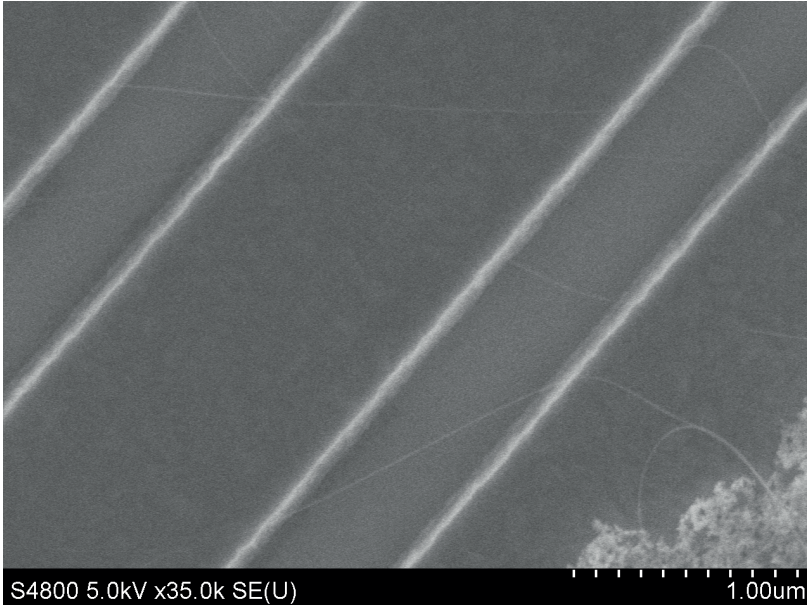


FIGURE 3.6: Scanning electron microscope image of CNTs grown across two trenches on MoRe. Trenches have a width of 600 nm a depth of 200 nm and are separated $1.2 \mu\text{m}$ from each other.

Promising devices with a resistance of approximately $20 \text{ k}\Omega$ have been wire-bonded and cooled to 4 K for further investigations. Spectroscopy was done by measuring the current through the device at a fixed bias voltage with respect to the gate voltage. By changing the gate voltage the suspended part of the CNT is doped with holes or electrons. The suspended part of a semi-conducting CNT can become a p-n-p or n-p-n quantum dot which then should exhibit Coulomb blockade (see chapter 2) .

Figure 3.7 a, shows the four-terminal voltage versus current across a CNT-SQUID made of MoRe with two single walled CNT Josephson junctions in parallel. The critical current is measured as a switch in voltage at 28 nA when sweeping from

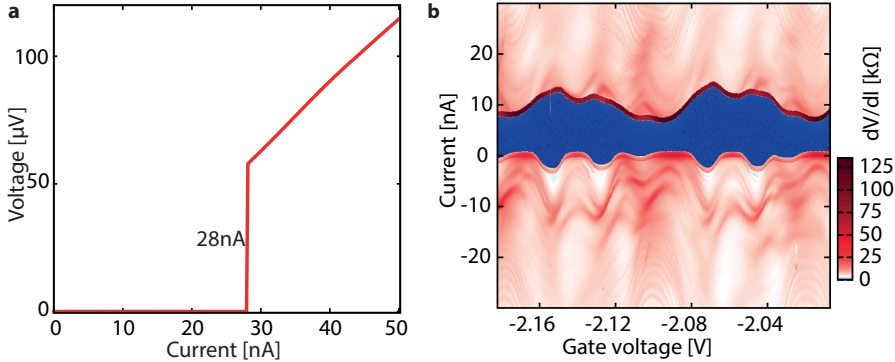


FIGURE 3.7: Four-terminal voltage versus applied current across a CNT-SQUID made of MoRe. **a**, The voltage switch at 28 nA indicates that one CNT carries at least a 14 nA supercurrent, a value which is higher than those previously reported for a single walled carbon nanotube. **b**, Differential resistance dV_M/dI_B (colour map) as a function of Current and Gate voltage (forward sweep direction at $T=100$ mK). The critical current oscillates with gate voltage, following the modulation of the normal-state conductance.

negative to positive current indicating that each CNT carries a supercurrent of 14 nA. This value, measured across the 800 nm long single walled CNT at 25 mK, is much higher than reported previously.[26–36] The critical current of the CNT junctions is also tuneable by the gate following the resistance of the CNTs which is oscillating with gate voltage in the hole regime (Fig. 3.7 b) at 100 mK.

3.1.4 CONCLUDING REMARKS

Table 3.2 shows an overview of the three superconducting metals tested for suitability in making a clean CNT device while withstanding the harsh conditions in a CNT oven at 900 ° C. NbTiN has a critical temperature of 15 K; it was however not chosen because of its high sensitivity for O₂ at 900 ° C its suppression of CNT yield and the high resistance observed of the few CNT devices which were produced with NbTiN. Rhenium with a literature T_C value of 1.69 K proved to be a reliable material for CNT growth with a high device yield and low contact resistances. However, its maximum critical current of 2 nA makes it difficult to obtain a high coupling strength for a CNT-SQUID in the presence of a magnetic field. Molybdenum-Rhenium alloy has a measured T_C of 5.5 K. It showed low contact resistances and a high critical current of 14 nA for one single walled CNT. This superconductor thus proved to be the optimal candidate to build superconducting CNT mechanical devices such as for instance the CNT-SQUID described in the next chapter.

	NbTiN	Rhenium	Molybdenum-Rhenium
T_C	15 K[7]	1.69 K[15]	5.5 K
Work-function	3.8 eV[10, 11]	5 eV[16]	4.6-4.95 eV[18]
Meas. CNT Res.	1 M Ω	20 K Ω	20 K Ω
Device Yield	>1%	30%	30%
Meas. I_C	-	2 nA[14]	12 nA[37]

TABLE 3.2: Overview the three materials tested suitable for CNT Growth. While NbTiN has the highest T_C , it obtained the lowest device yield with the highest room temperature contact resistance to a CNT. Rhenium and Molybdenum-Rhenium did obtain the same yield and contact resistance. Molybdenum-Rhenium has a higher T_C and a higher critical current for a SWCNT.

REFERENCES

- [1] J. Cao, Q. Wang, and H. Dai, *Electron transport in very clean, as-grown suspended carbon nanotubes*, *Nature Materials* **4**, 745 (2005).
- [2] A. K. Hüttel, G. A. Steele, B. Witkamp, M. Poot, L. P. Kouwenhoven, and H. S. J. van der Zant, *Carbon nanotubes as ultrahigh quality factor mechanical resonators*, *Nano Lett.* **9**, 2547 (2009).
- [3] J. Clarke and A. I. Braginski, *The {SQUID} handbook*, vol. 1 (Wiley Online Library, 2006).
- [4] S. Etaki, M. Poot, I. Mahboob, K. Onomitsu, H. Yamaguchi, and H. S. J. van der Zant, *Motion detection of a micromechanical resonator embedded in a dc {SQUID}*, *Nature Phys.* **4**, 785 (2008).
- [5] M. Tinkham, *Introduction to superconductivity* (McGraw Hill (New York), 1996).
- [6] R. E. Bedford, G. Bonnier, H. Maas, and F. Pavese, *Recommended values of temperature on the International Temperature Scale of 1990 for a selected set of secondary reference points*, *Metrologia* **33**, 133 (2003).
- [7] J. R. Gavaler, D. W. Deis, J. K. Hulm, and C. K. Jones, *Superconducting properties of Niobium-Titanium-Nitride thin films*, *Appl. Phys. Lett.* **15**, 329 (1969).
- [8] R. G. Wilson, *Vacuum Thermionic Work Functions of Polycrystalline Nb, Mo, Ta, W, Re, Os, and Ir*, *J. Appl. Phys.* **37**, 3170 (1966).
- [9] P. H. Dalle Mura, Tech. Rep., DTIC Document (1952).

- [10] D. R. Heslinga, H. H. Weitering, D. P. der Werf, T. M. Klapwijk, and T. Hibma, *Atomic-structure-dependent Schottky barrier at epitaxial Pb/Si (111) interfaces*, Phys. Rev. Lett. **64**, 1589 (1990).
- [11] W. Middleton and M. E. Van Valkenburg, *Reference data for engineers: radio, electronics, computer, and communications* (Newnes, 2002).
- [12] M. Shiraishi and M. Ata, *Work function of carbon nanotubes*, Carbon **39**, 1913 (2001).
- [13] H. K. Birnbaum, M. L. Grossbeck, and M. Amano, *Hydride precipitation in Nb and some properties of NbH*, Journal of the Less Common Metals **49**, 357 (1976), ISSN 0022-5088.
- [14] H. Keijzers, *Josephson effects in carbon nanotube mechanical resonators and graphene* (PhD-Thesis, Tu-Delft, 2012).
- [15] B. W. Roberts, *Survey of superconductive materials and critical evaluation of selected properties*, J. Phys. Chem. Ref. Data **5** (1976).
- [16] Y. Liang, J. Curlless, C. J. Tracy, D. C. Gilmer, J. K. Schaeffer, D. H. Triyoso, and P. J. Tobin, *Interface dipole and effective work function of Re in Re/ HfO/ SiO/ n-Si gate stack*, Appl. Phys. Lett. **88**, 72907 (2006).
- [17] L. R. Testardi, J. J. Hauser, and M. H. Read, *Enhanced superconducting Tc and structural transformation in Mo-Re alloys*, Solid State Commun. **9**, 1829 (1971).
- [18] S. Berge, P. O. Gartland, and B. J. Slagsvold, *Photoelectric work function of a molybdenum single crystal for the (100),(110),(111),(112),(114), and (332) faces*, Surf. Sci. **43**, 275 (1974).
- [19] H. W. Fink and G. Ehrlich, *Rhenium on W (110): Structure and mobility of higher clusters*, Surf. Sci. **150**, 419 (1985).
- [20] A. Andreone, A. Barone, A. Di Chiara, G. Mascolo, V. Palmieri, G. Peluso, and U. di Uccio, *Mo-Re superconducting thin films by single target magnetron sputtering*, Magnetism, IEEE Transactions on **25**, 1972 (1989).
- [21] P. E. Frieberthausen and H. A. Notarys, *Electrical Properties and Superconductivity of Rhenium and Molybdenum Films*, Journal of Vacuum Science and Technology **7**, 485 (1970).

- [22] A. U. Haq and O. Meyer, *Electrical and superconducting properties of rhenium thin films*, Thin Solid Films **94**, 119 (1982).
- [23] M. Ashkin, D. W. Deis, M. Gottlieb, and C. K. Jones, *Ultrasonic attenuation in superconducting molybdenum-rhenium alloys*, Physica **55**, 631 (1971).
- [24] V. E. Shaternik, A. N. Ivanjuta, and A. V. Shaternik, *Nonuniform current flow in superconductor-fullerene-superconductor junctions*, Low. Temp. Phys+ **32**, 633 (2006).
- [25] I. Milostnaya, A. Korneev, M. Tarkhov, A. Divochiy, O. Minaeva, V. Seleznev, N. Kaurova, B. Voronov, O. Okunev, G. Chulkova, et al., *Superconducting single photon nanowire detectors development for IR and THz applications*, J. Low Temp. Phys. **151**, 591 (2008).
- [26] A. F. Morpurgo, J. Kong, C. M. Marcus, and H. Dai, *Gate-controlled superconducting proximity effect in carbon nanotubes*, Science **286**, 263 (1999).
- [27] A. Y. Kasumov, R. Deblock, M. Kociak, B. Reulet, H. Bouchiat, I. I. Khodos, Y. B. Gorbatov, V. T. Volkov, C. Journet, and M. Burghard, *Supercurrents through single-walled carbon nanotubes*, Science **284**, 1508 (1999).
- [28] a. Kasumov, M. Kociak, M. Ferrier, R. Deblock, S. Guéron, B. Reulet, I. Khodos, O. Stéphan, and H. Bouchiat, *Quantum transport through carbon nanotubes: Proximity-induced and intrinsic superconductivity*, Phys. Rev. B. **68**, 214521 (2003), ISSN 0163-1829.
- [29] H. I. Jørgensen, K. Grove-Rasmussen, T. Novotný, K. Flensberg, and P. E. Lindelof, *Electron transport in single-wall carbon nanotube weak links in the Fabry-Perot regime*, Phys. Rev. Lett. **96**, 207003 (2006).
- [30] P. Jarillo-Herrero, J. A. Van Dam, and L. P. Kouwenhoven, *Quantum supercurrent transistors in carbon nanotubes*, Nature **439**, 953 (2006).
- [31] J.-P. Cleuziou, W. Wernsdorfer, V. Bouchiat, T. H. Ondarçuhu, and M. Monthieux, *Carbon nanotube superconducting quantum interference device*, Nature Nanotech. **1**, 53 (2006).
- [32] H. T. Man, *Carbon nanotube-based superconducting and ferromagnetic hybrid systems* (PhD-Thesis, Tu-Delft, 2006), ISBN 9789085930150.
- [33] K. Grove-Rasmussen, H. I. Jørgensen, and P. E. Lindelof, *Kondo resonance enhanced supercurrent in single wall carbon nanotube Josephson junctions*, New J. Phys. **9**, 124 (2007), ISSN 1367-2630.

-
- [34] G. Liu, Y. Zhang, and C. N. Lau, *Gate-tunable dissipation and "superconductor-insulator" transition in carbon nanotube Josephson junctions*, Phys. Rev. Lett. **102**, 16803 (2009).
- [35] K. Grove-Rasmussen, H. I. Jørgensen, B. Andersen, J. Paaske, T. S. Jespersen, J. Nygård, K. Flensberg, and P. E. Lindelof, *Superconductivity-enhanced bias spectroscopy in carbon nanotube quantum dots*, Phys. Rev. B. **79**, 134518 (2009), ISSN 1098-0121, [arXiv:0809.1944v2](https://arxiv.org/abs/0809.1944v2).
- [36] A. Tselev, Y. Yang, J. Zhang, P. Barbara, and S. E. Shafranjuk, *Carbon nanotubes as nanoscale probes of the superconducting proximity effect in Pd-Nb junctions*, Phys. Rev. B. **80**, 54504 (2009).
- [37] B. H. Schneider, S. Etaki, H. S. J. van der Zant, and G. A. Steele, *Coupling carbon nanotube mechanics to a superconducting circuit*, Sci. Rep. **2** (2012).

4

COUPLING CARBON NANOTUBE MECHANICS TO A SUPERCONDUCTING CIRCUIT

The quantum behaviour of mechanical resonators is a new and emerging field driven by recent experiments reaching the quantum ground state. The high frequency, small mass, and large quality-factor of carbon nanotube resonators make them attractive for quantum nanomechanical applications. A common element in experiments achieving the resonator ground state is a second quantum system, such as coherent photons or superconducting device, coupled to the resonators motion. For nanotubes, however, this is a challenge due to their small size. Here, we couple a carbon nanoelectromechanical (NEMS) device to a superconducting circuit. Suspended carbon nanotubes act as both superconducting junctions and moving elements in a Superconducting Quantum Interference Device (SQUID). We observe a strong modulation of the flux through the SQUID from displacements of the nanotube. Incorporating this SQUID into superconducting resonators and qubits should enable the detection and manipulation of nanotube mechanical quantum states at the single-phonon level.

Parts of this chapter have been published in Scientific Reports (2012) [1].

THE remarkable properties of nanoelectromechanical systems (NEMS) are useful for a wide variety of applications, such as ultra-sensitive force detection [2–4], mass detection at the single atom level [5, 6], and exploring the quantum limit of mechanical motion [7–11]. For all of these applications, sensitive detection of the resonator motion is crucial. The ultimate limit of the detection of the motion of a mechanical resonator is given by its quantum zero point fluctuations, which result in an uncertainty in the resonators position determined by the standard quantum limit [12].

An effective way of detecting the quantum motion of mechanical devices is to couple their displacement to another “probe” quantum system which can be read out and controlled, such as coherent quantum states of a superconducting qubit [9], coherent photons in a cold microwave resonator circuit [10], or the coherent fields of a laser [11]. In the last decade, superconducting circuits have emerged as an established platform for engineering and controlling quantum behaviour [13]. This has formed the motivation for many works coupling MEMS and NEMS devices to superconducting circuits [3, 9, 10, 12, 14–16]. By coupling microelectromechanical (MEMS) devices to quantum superconducting circuits, researchers have recently demonstrated mechanical resonators in their quantum ground state [9, 10] and achieved single-phonon control over their motion [9]. An outstanding challenge in these experiments is simultaneously achieving both a strong coupling at the single-phonon level, together with a high frequency and large quality factor for the mechanical resonator.

Carbon nanotube mechanical resonators [17–19] possess a unique combination of large quality factor, small mass, and high frequency. Because of their small size, however, it is not easy to couple to their quantum motion. Techniques based on a capacitive interaction with superconducting qubits or microwave photon cavities, as was done in recent experiments with MEMS devices reaching the mechanical quantum ground state [9, 10], do not provide sufficient coupling strength. An alternative is to incorporate the mechanical element into a SQUID, as was demonstrated recently using micromechanical beams [20]. If a carbon nanotube NEMS element could be included in a SQUID, the SQUID could then be used as a transducer to couple the mechanical motion to a superconducting cavity [21], or as the basis for a superconducting qubit, coupling the motion directly to the quantum states of the qubit.

Here, we demonstrate the coupling of a carbon nanotube NEMS device to a superconducting circuit, based on a suspended carbon nanotube SQUID. The flux through the SQUID couples to the nanotube displacement with a strength of $0.36 \text{ m}\Phi_0/\text{pm}$. This new device opens up the possibility of combining carbon NEMS devices with the quantum toolkit from the superconducting community. Doing so, we expect the suspended nanotube SQUID will provide a platform for detection of

the nanotube resonator's ground state, and control over its motion at the level of single phonons.

4.1 RESULTS

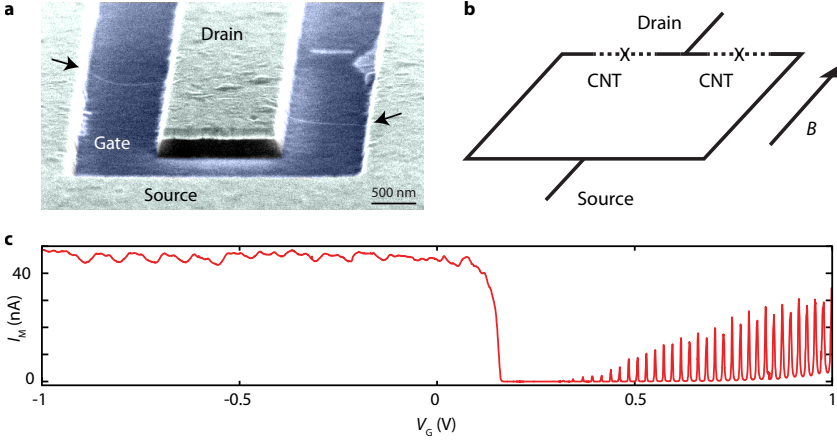


FIGURE 4.1: **Design and characterization of the device** **a**, Colorised scanning electron microscope (SEM) image of a typical device showing a single carbon nanotube (CNT) crossing two trenches. The device is made by etching two 800 nm wide trenches in a MoRe layer and underlying SiO_2 , and subsequently growing CNTs over the prefabricated structure. We apply a voltage V_G to the doped substrate underneath the SiO_2 , which acts as a gate. **b**, Schematic drawing of the SQUID. The two suspended segments of the CNT form two SNS-type Josephson junctions, indicated by the crosses. An external magnetic field B can be applied in-plane along the trench. **c**, I_M as a function of V_G measured with an applied source-drain bias voltage $V_B = 2$ mV. For $V_G > 0.3$ V, the suspended segments form a p-n-p quantum dots exhibiting Coulomb blockade. For $V_G < 0.2$ V, the CNT is doped with holes, showing Fabry-Pérot oscillations with high conductance.

The device consists of a SQUID in which the two Superconductor-Normal metal-Superconductor (SNS) weak links are made from carbon nanotube junctions [22–24]. In contrast to earlier works, the carbon nanotubes are freely suspended, and thus also act as NEMS elements embedded in the SQUID. To make the suspended nanotube SQUID, a clean carbon nanotube is grown in the last step of fabrication [25] over a trench patterned between metal source and drain contacts made from a MoRe superconducting alloy (see Methods). A Scanning Electron Microscope (SEM) image of a typical device is shown in Fig. 4.1a. The doped substrate below the trench is used as a global backgate. The device is mounted in a superconducting magnet coil with the magnetic field aligned in the plane of the sample, parallel to the trenches, as indicated in Fig. 4.1b. The magnetic field orientation is chosen

to maximize the coupling of vertical displacements on the nanotube to flux in the SQUID loop [20]. A small misalignment of the sample also induces a magnetic field perpendicular to the sample surface which is used to tune the flux operating point of the SQUID.

Figure 4.1c shows the current through the device (I_M) as a function of the applied gate voltage (V_G). From the gate voltage thresholds for electron and hole conduction, we estimate that the carbon nanotube has a small bandgap of 40 meV (see Supplementary Information). Due to a work function difference present between the nanotube and the metal contacts, the nanotube is doped with holes near the edge of the trench. At positive gate voltages, electrons induced by the gate are confined by p-n junction tunnel barriers [25] in a Coulomb-blockaded quantum dot. For negative gate voltages, holes are induced in the suspended segment with no tunnel barriers. Here, instead of Coulomb blockade, conductance oscillations arising from Fabry-Pérot electronic interference [26] are observed with conductances of up to $4.7 e^2/h$ (see Fig. 4.2a). Note that this value exceeds the maximum conductance expected for a single carbon nanotube ($G_{\max} = 4 e^2/h$), consistent with a SQUID geometry (Fig. 4.1b) where there are two carbon nanotube junctions in parallel (Fig. 4.1a).

In Fig. 4.2, we use the gate to dope the nanotube with holes such that the device is tuned into the high-conductance Fabry-Pérot regime, and measure the voltage across the SQUID as a function of an applied bias current (Fig. 4.2a). At low currents, the voltage across the device is zero, a clear indication of a proximity effect induced supercurrent. At a critical current of 24 nA, there is a switch to a finite voltage state. We attribute the large critical current in our junctions (12 nA per nanotube) to the high critical temperature of the superconducting metal leads ($T_C = 5.5$ K), the low contact resistance between the superconducting metal and the nanotube, and the clean electronic characteristics of the carbon nanotube. As shown in Fig. 4.2b, the critical current is strongly modulated by the gate through to gate dependence of the normal-state conductance [22]. Due to the high transparency of the superconductor-nanotube interface, the supercurrent in our device also remains finite in the valleys between the peaks in conductance.

To demonstrate that the device acts as a SQUID, we measure the critical current as a function of the flux through the loop. In practice, we do this by sweeping a large in-plane magnetic field to zero and then subsequently measure the critical current as a function of time. Due to creep in the superconducting magnet coil and the slight misalignment of the field to the sample plane, there is a small magnetic field component perpendicular to the surface that continues to change slowly after the sweep is completed. In such a measurement, shown in Fig. 4.2c, the observed critical current oscillates between a value of 24 nA and 2 nA. These oscillations result from quantum interference of the superconducting wavefunction traversing

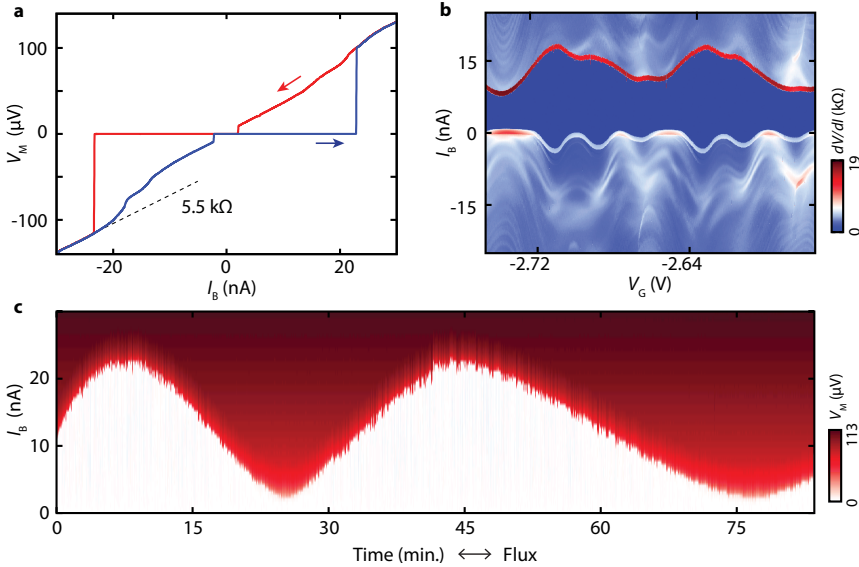


FIGURE 4.2: **A suspended carbon nanotube SQUID** **a**, Four-terminal current-voltage trace at $V_G = -1.1$ V. The onset of the resistive branch occurs at 24 nA, corresponding to a critical current of 12 nA per nanotube junction. The dashed line indicates the normal-state resistance of 5.5 kΩ ($G = 4.7 e^2/h$). The device is hysteretic, as can be seen from the forward (blue) and reverse (red) sweep directions [27]. **b**, Differential resistance dV_M/dI_B (color map) as a function of I_B and V_G (forward sweep direction). The critical current (red stripe at positive I_B) oscillates with V_G , following the modulation of the normal state conductance. **c**, SQUID voltage V_M as a function of applied current I_B and time, taken at $B = 0$ and $V_G = -1.1$ V. Flux creep in the superconducting magnet coil is used to apply a small time varying magnetic field. The critical current oscillates from 2 nA up to 24 nA as a function of the flux through the SQUID. The near complete suppression of I_C at the minima indicates that the SQUID has highly symmetric junctions.

the two junctions of the SQUID [27]. The large sensitivity of the critical current to the flux from the small magnetic field creep, together with the single periodicity, is consistent with a single large SQUID loop formed by one nanotube SNS junction across each trench, as shown in the SEM image of a typical device in Fig. 4.1a.

We now turn our attention to the behaviour of the device in the presence of a static in-plane magnetic field applied parallel to the trench. Figures 4.3a and 4.3b show the gate voltage dependence of the critical current with and without an external magnetic field. The measurements are taken intentionally with a coarse gate voltage resolution such that the measurement time is short compared to the timescale of the flux creep (see Supplementary Information for further details).

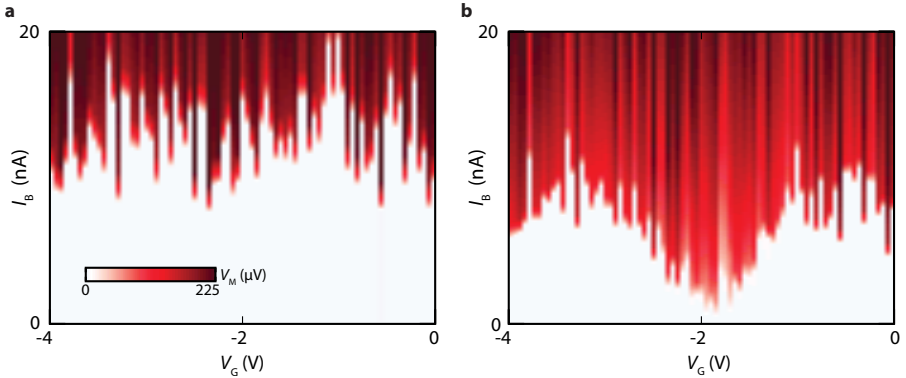


FIGURE 4.3: **A gate-voltage induced magnetic flux a**, Colormap of V_M as a function of I_B and V_G , taken at $B = 0$ T. The critical current I_C is defined by the onset of a finite voltage state, indicated by the red regions. The Fabry-Pérot modulation of the critical current (Fig. 2b) is visible as rapid fluctuations in I_C due to the large steps in V_G . The measurement is performed fast enough such that the magnetic field creep (Fig. 2c) can be neglected. **b**, Same measurement taken at $B = 250$ mT. An additional approximately sinusoidal modulation of the critical current is seen with a gate periodicity of $\Delta V_G = 2.5$ V.

The steps in gate voltage are much larger than the periodicity of the Fabry-Pérot conductance oscillations (Fig. 4.2a); consequently, these appear in Fig. 4.3a as (reproducible) single-pixel fluctuations. Figure 4.3b shows the same measurement taken at an external magnetic field of 250 mT. Here, an additional nearly sinusoidal modulation of the critical current can be seen as a function of gate voltage with a periodicity much longer than that of the Fabry-Pérot conductance oscillations.

In the following, we show how this additional gate modulation of the critical current arises from a change in magnetic flux induced by the d.c. gate voltage. The mechanism for such a gate induced flux is illustrated in Fig. 4.4b. Increasing the gate voltage, the nanotube is pulled towards the gate by the attractive electrostatic force between them. The nanotube displacement introduces an extra area ΔA of the SQUID loop perpendicular to the magnetic field aligned along the trench. This area change results in a flux change linearly proportional to the displacement, $\Delta\Phi \propto B\ell u$, where B is the in-plane magnetic field, ℓ is the nanotube length, and u is the vertical displacement of the nanotube. If the displacement u is linear in the gate voltage (as expected for certain gate voltage ranges, see Supplementary Information for further discussion), the critical current of the SQUID will then oscillate as a function of gate voltage with constant periodicity, as observed in Fig. 4.3b.

If this gate-voltage induced flux indeed arises from a mechanical displacement

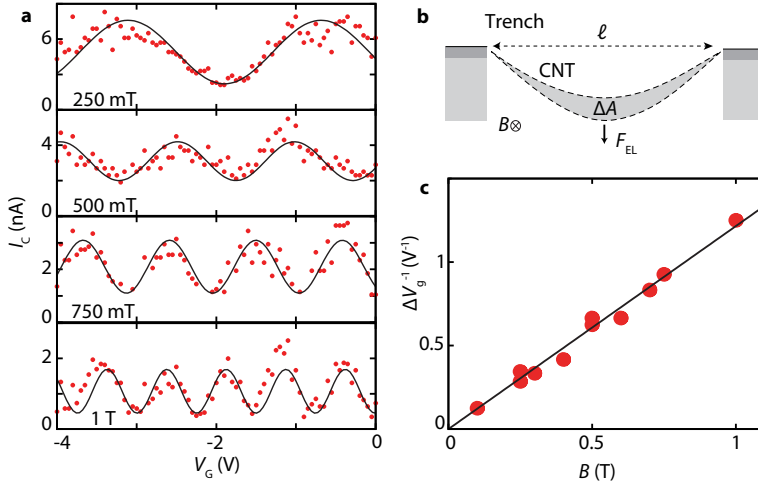


FIGURE 4.4: **Mechanical flux coupling** **a**, Extracted I_C (dots) as a function of V_G at four different magnetic fields. Lines show a sinusoidal fit to the data (red points) from which the periodicity ΔV_G^{-1} is extracted. At $B = 1$ T, five oscillations are visible corresponding to a flux change of $5 \Phi_0$. **b**, Vertical displacement of the nanotube due to the electrostatic force from the gate changes the area of the SQUID loop perpendicular to the in-plane magnetic field. This produces a gate-induced flux change proportional to the nanotube displacement, resulting in an I_C that oscillates with V_G . We estimate that the nanotube displaces by 7.4 nm as V_G is swept from 0 to -4 V ($\Delta A \sim 5.5 \times 10^{-3} \mu\text{m}^2$ per nanotube). **c**, ΔV_G^{-1} (dots) as a function of magnetic field with a linear fit (black line). At $B = 1$ T, the flux couples to the vertical displacement of the nanotube with a flux coupling of $0.36 \text{ m}\Phi_0/\text{pm}$.

of the nanotube, the flux coupling should scale linearly with the external magnetic field. Figure 4.4a shows the extracted I_C versus V_G for fields up to 1 T. To extract the gate periodicity of the flux oscillation, the critical current as a function of gate voltage is fit to a sinusoidal function in order to approximate the expected oscillatory SQUID response [27]. The resulting gate frequency V_G^{-1} is plotted as a function of magnetic field in Fig. 4.4c. The linear scaling of the periodicity with magnetic field demonstrates that the modulation is due to a flux originating from the mechanical displacement of the nanotube. At magnetic fields of 1 T, we couple the motion of the nanotube to the flux in the SQUID with a coupling strength of $0.36 \text{ m}\Phi_0/\text{pm}$ (see Supplementary Information).

4.2 DISCUSSION

In the previous section, we demonstrate a strong coupling of the flux in a SQUID to the displacement of the carbon nanotube NEMS device. The strong flux cou-

pling is, on its own, not unique to our device: for example, a larger mechanical flux responsivity was observed in a top-down fabricated SQUID [20]. What is unique to our device is the combination of such a flux coupling with a mechanical resonator with small mass (attogram) and large zero point fluctuations. This can be quantified in terms of the amount of flux noise the mechanical zero-point fluctuations would induce in the SQUID. The expected zero point motion of the nanotube is on the order of $u_{\text{ZPF}} = \sqrt{\hbar/2m\omega} = 3.6$ pm. Together with a quality factor of 3×10^4 and a mechanical resonance frequency of 125 MHz observed in this device (see Supplementary Information), this results in a peak in the flux noise spectrum of the SQUID at the mechanical resonance frequency with an amplitude of $16 \mu\Phi_0/\sqrt{\text{Hz}}$. This noise level, corresponding to the imprecision noise from the standard quantum limit for our device, is nearly two orders of magnitude larger than the $0.2 \mu\Phi_0/\sqrt{\text{Hz}}$ sensitivity that has been demonstrated coupling a SQUID to a superconducting resonator [28]. Doing so, we expect that such a high frequency suspended carbon nanotube SQUID can be used as a linear position detector with an imprecision noise below the standard quantum limit, enabling the detection of the quantum motion of a carbon nanotube.

Finally, the strong coupling between flux and nanotube displacement could also be used to implement a nanomechanical resonator coupled to a superconducting qubit. The important characterization of the coupling between the two quantum systems is the zero-phonon coupling rate g , given by the energy shift of the probe quantum system in response to the zero-point fluctuations of the mechanical device [11]. In order to have a coherent interaction between the probe and the mechanical system at the single-phonon level, the coupling rate g must be larger than the decoherence rates of quantum states of the mechanical system and probe system. Incorporating a nanotube SQUID into a transmon-qubit design would achieve a single-phonon coupling rate of $g = 7$ MHz (see Supplementary Information). Such a coupling strength would be within the single-phonon strong-coupling limit, providing a means for the readout and control of mechanical quantum states of a carbon nanotube.

4.3 METHODS

Measurements are performed in a dilution refrigerator at a base temperature of 25 mK. The device is connected via copper powder filters and low pass filters at base temperature to the measurement equipment at room temperature. Measurements are performed in either a 4-terminal current bias or a 2-terminal voltage bias configuration.

REFERENCES

- [1] B. H. Schneider, S. Etaki, H. S. J. van der Zant, and G. A. Steele, *Coupling carbon nanotube mechanics to a superconducting circuit*, Sci. Rep. **2** (2012).
- [2] D. Rugar, R. Budakian, H. J. Mamin, and B. W. Chui, *Single spin detection by magnetic resonance force microscopy*, Nature **430**, 329 (2004).
- [3] C. A. Regal, J. D. Teufel, and K. W. Lehnert, *Measuring nanomechanical motion with a microwave cavity interferometer*, Nature Phys. **4**, 555 (2008).
- [4] O. Usenko, A. Vinante, G. Wijts, and T. H. Oosterkamp, *A superconducting quantum interference device based read-out of a subattonewton force sensor operating at millikelvin temperatures*, Applied Physics Letters. **98**, 133105 (2011).
- [5] K. Jensen, K. Kim, and A. Zettl, *An atomic-resolution nanomechanical mass sensor*, Nature Nanotech. **3**, 533 (2008).
- [6] J. Chaste, A. Eichler, J. Moser, G. Ceballos, R. Rurali, and A. Bachtold, *A nanomechanical mass sensor with yoctogram resolution*, Nature Nanotech. **7**, 301 (2012).
- [7] K. C. Schwab and M. L. Roukes, *Putting mechanics into quantum mechanics*, Physics Today **58**, 36 (2005).
- [8] M. Poot and H. S. J. van der Zant, *Mechanical systems in the quantum regime*, Physics Reports **511**, 273 (2012).
- [9] A. D. O'Connell, M. Hofheinz, M. Ansmann, R. C. Bialczak, M. Lenander, E. Lucero, M. Neeley, D. Sank, H. Wang, M. Weides, et al., *Quantum ground state and single-phonon control of a mechanical resonator*, Nature **464**, 697 (2010).
- [10] J. D. Teufel, T. Donner, D. Li, J. W. Harlow, M. S. Allman, K. Cicak, A. J. Sirois, J. D. Whittaker, K. W. Lehnert, and R. W. Simmonds, *Sideband cooling of micromechanical motion to the quantum ground state.*, Nature **475**, 359 (2011), ISSN 0028-0836, [1103.2144](#).
- [11] J. Chan, T. P. M. Alegre, A. H. Safavi-Naeini, J. T. Hill, A. Krause, S. Gröblacher, M. Aspelmeyer, and O. Painter, *Laser cooling of a nanomechanical oscillator into its quantum ground state*, Nature **478**, 89 (2011).

- [12] J. D. Teufel, T. Donner, M. A. Castellanos-Beltran, J. W. Harlow, and K. W. Lehnert, *Nanomechanical motion measured with an imprecision below that at the standard quantum limit*, *Nature Nanotech.* **4**, 820 (2009).
- [13] J. Clarke and F. K. Wilhelm, *Superconducting quantum bits*, *Nature* **453**, 1031 (2008).
- [14] A. Naik, O. Buu, M. D. LaHaye, A. D. Armour, A. A. Clerk, M. P. Blencowe, and K. C. Schwab, *Cooling a nanomechanical resonator with quantum back-action*, *Nature* **443**, 193 (2006).
- [15] T. Rocheleau, T. Ndukum, C. Macklin, J. B. Hertzberg, A. A. Clerk, and K. C. Schwab, *Preparation and detection of a mechanical resonator near the ground state of motion*, *Nature* **463**, 72 (2009).
- [16] M. D. LaHaye, J. Suh, P. M. Echternach, K. C. Schwab, and M. L. Roukes, *Nanomechanical measurements of a superconducting qubit*, *Nature* **459**, 960 (2009).
- [17] V. Sazonova, Y. Yaish, H. Üstünel, D. Roundy, T. A. Arias, and P. L. McEuen, *A tunable carbon nanotube electromechanical oscillator*, *Nature* **431**, 284 (2004).
- [18] D. García-Sánchez, A. San Paulo, M. J. Esplandiú, F. Perez-Murano, L. Forró, A. Aguasca, and A. Bachtold, *Mechanical detection of carbon nanotube resonator vibrations*, *Phys. Rev. Lett.* **99**, 85501 (2007).
- [19] A. K. Hüttel, G. A. Steele, B. Witkamp, M. Poot, L. P. Kouwenhoven, and H. S. J. van der Zant, *Carbon nanotubes as ultrahigh quality factor mechanical resonators*, *Nano Lett.* **9**, 2547 (2009).
- [20] S. Etaki, M. Poot, I. Mahboob, K. Onomitsu, H. Yamaguchi, and H. S. J. van der Zant, *Motion detection of a micromechanical resonator embedded in a dc {SQUID}*, *Nature Phys.* **4**, 785 (2008).
- [21] E. Buks, S. Zaitsev, E. Segev, B. Abdo, and M. P. Blencowe, *Displacement detection with a vibrating rf superconducting interference device: Beating the standard linear limit*, *Phys. Rev. E* **76**, 26217 (2007).
- [22] P. Jarillo-Herrero, J. A. Van Dam, and L. P. Kouwenhoven, *Quantum supercurrent transistors in carbon nanotubes*, *Nature* **439**, 953 (2006).

- [23] J.-P. Cleuziou, W. Wernsdorfer, V. Bouchiat, T. H. Ondařu, and M. Monthieux, *Carbon nanotube superconducting quantum interference device*, Nature Nanotech. **1**, 53 (2006).
- [24] G. Liu, Y. Zhang, and C. N. Lau, *Gate-tunable dissipation and "superconductor-insulator" transition in carbon nanotube Josephson junctions*, Phys. Rev. Lett. **102**, 16803 (2009).
- [25] G. A. Steele, G. Gotz, and L. P. Kouwenhoven, *Tunable few-electron double quantum dots and Klein tunnelling in ultraclean carbon nanotubes*, Nature Nanotech. **4**, 363 (2009).
- [26] W. Liang, M. Bockrath, D. Bozovic, J. H. Hafner, M. Tinkham, and H. Park, *Fabry-Perot interference in a nanotube electron waveguide*, Nature **411**, 665 (2001).
- [27] J. Clarke and A. I. Braginski, *The SQUID handbook*, vol. 1 (Wiley Online Library, 2006).
- [28] M. Hatridge, R. Vijay, D. H. Slichter, J. Clarke, and I. Siddiqi, *Dispersive magnetometry with a quantum limited SQUID parametric amplifier*, Phys. Rev. B. **83**, 134501 (2011).

4.4 SUPPLEMENTARY INFORMATION

S1 DEVICE CHARACTERIZATION

In Fig. S1, we present electrical measurements characterizing the transport properties of the device, in which the Coulomb blockade and Fabry-Pérot transport regimes for different gate voltages can be seen, and from which the bandgap is estimated.

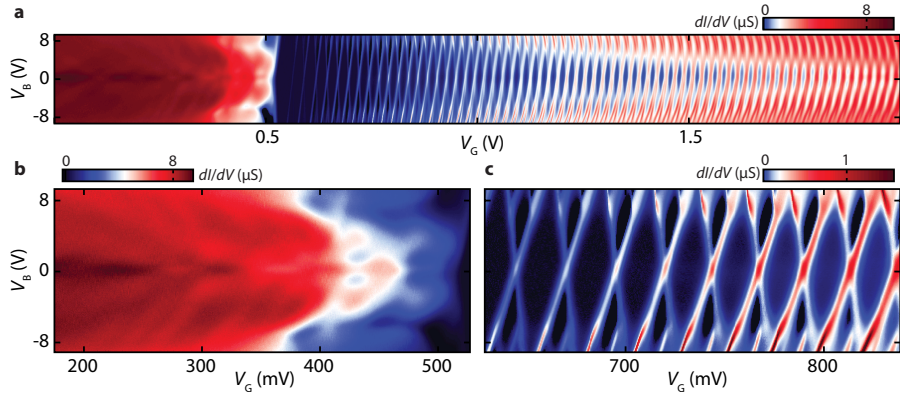


FIGURE 4.5: **Two-terminal differential conductance a**, as a function of the source-drain bias voltage V_B and gate voltage V_G , taken at 1.2 K (series resistance from wiring and filters has not been subtracted). This dataset was taken during an earlier cooldown of the device in a different cryogenic insert. As a result, there is a slight shift of the threshold gate voltage for hole conductance compared to Fig. 1c of the main text. We determine the bandgap of the device from the size of the empty Coulomb diamond by subtracting the average of the $1e/1h$ addition energies from the empty-dot addition energy. **b**, Zoom of the dataset showing the high-conductance Fabry-Pérot regime when doping the device with holes. **c**, Zoom of dataset showing Coulomb blockade when the device is doped with electrons. When doping the device with electrons, tunnel barriers naturally form from p-n junctions near the edge of the trench. The p-n junctions arise from a gate-independent p-type doping of the nanotube near the trench edge due to the work function difference between the nanotube and the metal contacts.

S2 DISCRIMINATING GATE-INDUCED FLUX FROM TIME-DEPENDENT FLUX CREEP

In this section, we present measurements which discriminate between time dependent magnetic flux creep (Fig. 2c in the main text) and gate-induced flux (Fig. 3b of the main text). This is done by plotting the time-dependent oscillations of I_C at different gate voltages. If the gate is inducing no flux in the SQUID, the oscillations at different gate voltages should all be in phase. If the gate is inducing a flux in the SQUID, there will be a phase shift between the oscillations at different gate

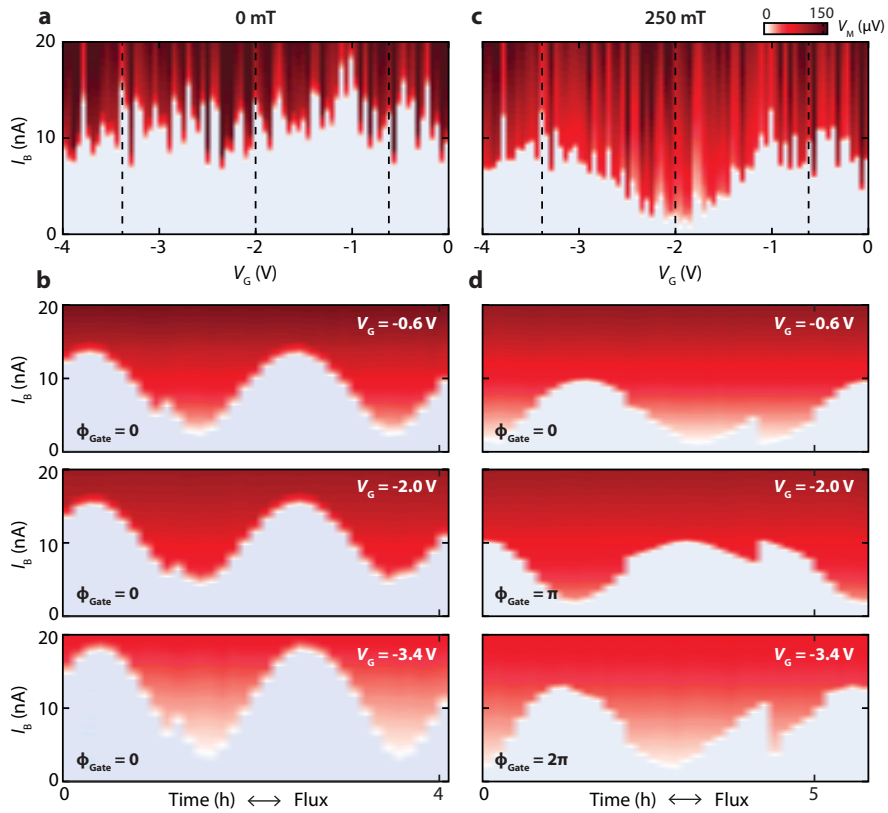


FIGURE 4.6: Gate-voltage induced flux observed by a gate-dependent shift of the phase of the time-dependent oscillations of I_{C_a} . Voltage V_M as a function of applied bias current I_B and gate voltage V_G at $B = 0$. **b**, V_M as a function of I_B and of time for three different gate voltages indicated by the dashed in **a**. **c,d** Same measurement as in **a,b**, but now taken in the presence of a parallel magnetic field of 250 mT. **d**, A gate dependent phase shift Φ_{Gate} of the oscillations of I_C is now observed, demonstrating that the gate voltage is inducing a magnetic flux in the SQUID.

voltages.

In Fig. S2, we demonstrate that at $B = 0$, the oscillations in time at different gate voltages are in phase, while $B = 250$ mT, they are shifted by the gate-induced flux. The data in Fig. S2 are extracted from a 3-D $(x, y, z) = (I_B, V_G, t)$ dataset (one at $B = 0$ and one at $B = 250$ mT). The measurements are performed by sweeping the bias current, stepping the gate voltage quickly, and then repeating this in time. The gate sweep is performed quickly enough such that the measurement time for a full gate sweep measurement, as shown in Fig. S2a, is fast compared to the external flux drift: the measurement time for such a gate sweep is $t_{meas} = 7$ min, while the external flux creep rate during these measurements is about $1 \Phi_0$ in two hours. Each gate sweep can therefore be considered to be taken at a fixed external flux. Note that in addition to the slow flux creep, we also sometimes observe sudden jumps in the external flux, such as can be seen at $t = 4.2$ hours in Fig. S2d. This results in a sudden jump in the phase of the oscillations. The gate induced phase shift, however, can still be tracked both immediately before and after the jump. The gate traces in Fig. S2 and Fig. 3 of the main text are extracted at timesteps where these flux jumps are not present.

Figure S2b shows I_C vs. time for three different gate voltages at $B = 0$. At zero external field, the oscillations of I_C measured at different gate voltages are all in phase, indicating no gate-induced flux. In Fig. S2d, we show I_C oscillations in time at $B = 250$ mT. The d.c. gate voltage now shifts the phase of the oscillations, as can be seen clearly in Fig. S2d. This gate-dependent phase shift demonstrates that the gate-induced sinusoidal modulation of I_C shown in Fig. S2c, and Fig. 3c of the main text, are indeed caused by a gate-voltage induced magnetic flux.

S3 EXPECTED STATIC DISPLACEMENT OF THE NANOTUBE WITH GATE VOLTAGE

When a constant voltage V_G is applied to the gate, the suspended nanotube segments are attracted to the gate by a Coulomb force, $F_C \propto V_G^2$. The equilibrium position of the nanotube corresponds to the position where this Coulomb force is balanced by the mechanical restoring force [2]. At small gate voltages, the bending rigidity of the nanotube dominates the mechanical restoring force, giving a static displacement $u \propto V_G^2$ (the weak bending regime). Beyond a certain gate voltage, induced tension in the nanotube becomes important in determining the mechanical restoring force, and there is a transition to a strong bending regime in which $u \propto V_G^{2/3}$. The transition between these two regimes depends on the dimensions of the nanotube, and can also be influenced by additional tension introduced, for example, by the fabrication process. In any case, the net result is that the displacement of the nanotube as a function of gate voltage is, to a good approximation,

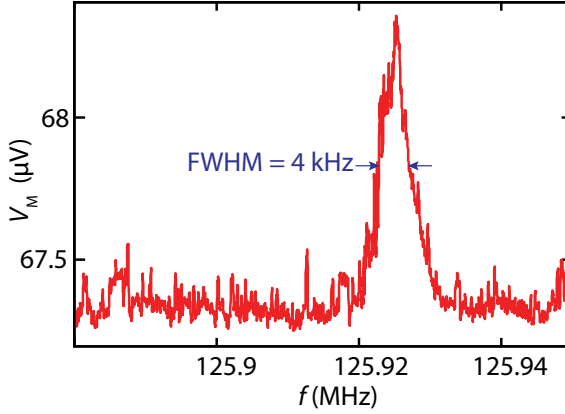


FIGURE 4.7: **Driven mechanical resonance of the nanotube** measured by applying a bias current above the critical current and using rectification readout technique introduced in [1]. We estimate the quality factor of the resonance from the full width at half maximum, Δf , of the measured curve. With $f_R = 126$ MHz and $\Delta f = 4$ kHz, we get $Q = f_R/\Delta f = 3 \times 10^4$.

linear over a relatively wide regime of voltages, as can be seen in Fig. 2 of Sapmaz *et al.* [2].

If the nanotube displacement was not linear in gate voltage, the periodicity of the I_C oscillations in gate voltage, ΔV_G^{-1} , would change slowly as a function of gate voltage. The relatively constant ΔV_G^{-1} we observe in Fig. 4a of the main text indicates that the nanotube displacement in our device is indeed approximately linear in the range of gate voltages we study.

Critical current oscillations in gate voltage were fitted to a cosine function:

$$f(x) = \frac{a+b}{2} + \frac{a-b}{2} \cos \left[(x - x_0) \frac{2\pi}{L} \right] \quad (4.1)$$

where a and b are the maximum and minimum of the modulation respectively, and where x_0 is the position at the maximum and L the periodicity.

S4 DEFINITION OF THE NANOTUBE DISPLACEMENT AND ESTIMATION OF THE FLUX RESPONSIVITY

In this section, we give a rigorous definition of the nanotube displacement, and use this definition to calculate the flux responsivity of the device. In particular, following Poot *et al.* [3], we define the displacement of a mode of the nanotube in such a way that we require only one total mass for all modes, avoiding the complication of having different effective masses for different modes.

The zero-frequency, or dc, flexural displacement $z_{\text{dc}}(x, y)$ of the carbon nanotubes towards the back gate (the $x - y$ plane), can be described by a single coordinate u_{dc} . The displacement per unit force and the change of area ΔA per unit displacement both depend on the chosen definition of u_{dc} . This is also true for the mechanical resonance modes of the nanotube, which form an eigenbasis for the nanotube displacement. Any periodic displacement of the nanotube with frequency f can be decomposed into a superposition of the eigenmodes:

$$z(x, y, t) = \sum_0^{\infty} u_n \xi_n(x, y) \cos(2\pi f t + \varphi_n), \quad (4.2)$$

where u_n is the displacement coordinate, $\xi_n(x, y)$ is the normalized mode shape, f_n is the eigenfrequency and φ_n is the phase offset of mode n . For a nanotube with length ℓ much larger than its cross-sectional diameter, $\xi_n(x, y)$ is usually integrated in the radial direction, such that the mode shape can be described as a function of only the distance along its length direction, x , i.e. $\xi_n(x, y) \rightarrow \xi_n(x)$. The dc displacement ($f = 0$) is related to the eigenmodes by:

$$z_{\text{dc}}(x) = \sum_0^{\infty} u_n \xi_n(x). \quad (4.3)$$

In general, the displacement, modeshapes and eigenfrequencies of the nanotube must be solved from its elastodynamic differential equations and depend on the nanotube geometry, its rigidity, any built-in tension, and the amount and distribution of applied forces. Once this is done, the definition of displacement depends on the choice of normalization for $\xi_n(x)$. A convenient normalization for $\xi_n(x)$ is:

$$\frac{1}{\ell} \int_0^{\ell} \xi_n(x)^2 dx = 1. \quad (4.4)$$

With this normalization, the displacement coordinate u_n is (spatial) root-mean-square displacement of mode n . The dynamical spring constant of each eigenmode now equals $k_n = m_{\text{R}}(2\pi f_n)^2$, where m_{R} is the nanotube mass. The change in area due to a d.c. nanotube displacement becomes:

$$\Delta A = \int_0^{\ell} z_{\text{dc}}(x) dx = \sum_0^{\infty} a_n \ell u_n, \quad (4.5)$$

$$a_n \equiv \frac{1}{\ell} \int_0^{\ell} \xi_n(x) dx. \quad (4.6)$$

To estimate the numerical coefficients a_n , we assume sinusoidal eigenmode shapes for the nanotubes: $\xi_n(x) = \sqrt{2} \sin(\pi n x / \ell)$ (based on [3]). The numerical coefficients then become $a_n = 0.9/n$ for odd n and $a_n = 0$ for even n (no net area

change). For a displacement due to a uniformly distributed dc force, the amplitude of each eigenmode is proportional to $(a_n/f_n)^2$, which means that the shape of the dc deflection is almost entirely determined by the fundamental eigenmode (f_n is roughly proportional to n). The dc spring constant is then equal to k_1 and the area change for both u_{dc} and u_1 is characterized by the same coefficient, $a_1 = 0.9$.

Having defined the displacement, we are now in a position to calculate the responsivity of the device. The flux responsivity Φ_u which we give in the main text is calculated by multiplying ΔA with the applied magnetic field B and dividing out the displacement u_{dc} :

$$\Phi_u \equiv \frac{d\Phi}{du_{dc}} \approx \frac{d\Phi}{du_1} = a_1 B \ell. \quad (4.7)$$

At a field of 1 T and a suspended nanotube length of 800 nm, we get a responsivity $\Phi_u = 0.35 \Phi_0/\text{nm}$ per suspended nanotube segment. The dc displacement of the nanotube due to the applied gate voltage can now be calculated based on Fig. 4a of the main text: At 1 T, we observe five oscillations of the SQUID critical current, i.e. $\Delta\Phi = 5\Phi_0$. With the calculated responsivity, the displacement of each nanotube segment over the full gate voltage range is $\Delta\Phi/\Phi_u = 7$ nm.

S5 ESTIMATION OF THE ZERO POINT MOTION

Quantum mechanical displacement fluctuations are dominant when a mechanical resonator with resonance frequency f_R is cooled to a temperature T such that its thermal energy is far less than the energy of a single phonon, i.e. $k_B T \ll hf_R$. Here, k_B is the Boltzmann constant and h is the Planck constant. In this regime, the resonator has an average phonon occupation which approaches zero, and displacement fluctuations are due to the quantum mechanical ground state energy of the resonator, which equals that of half a phonon. The root-mean-square value of the ground state displacement fluctuations is called the zero-point motion and is given by [3]:

$$u_{zpf} = \sqrt{\frac{hf_R}{2m_R(2\pi f_R)^2}} \quad (4.8)$$

The maximum power spectral density $S_{uu}(f)$ due to the zero-point motion occurs at the resonance frequency and is related to u_{zpf} according to [3]:

$$S_{uu}^{zpf}(f_R) = u_{zpf}^2 \left(\frac{\pi f_R}{2Q}\right)^{-1} = \frac{hQ}{\pi m_R(2\pi f_R)^2} \quad (4.9)$$

where Q is the quality factor of the resonator. In order to measure the zero-point fluctuations, the measurement sensitivity of the detector should be better (lower)

than $S_{uu}^{\text{zpf}}(f_R)$. The suspended carbon nanotubes in this paper each have a fundamental eigenmode with displacement in the direction of the back gate. Figure S3 shows a measurement of the mechanical response of the fundamental mode of one of the nanotubes to an applied driving force. From the response curve, we find a resonance frequency of 126 MHz and a quality factor $Q = 3 \times 10^4$. The mass of an 800 nm long single-walled carbon nanotube is approximately $m_R = 5 \times 10^{-21}$ kg (and the corresponding spring constant is thus $k = 3 \times 10^{-3}$ N/m). Using this lower bound for Q gives $u_{\text{zpf}} = 3.6$ pm and $\sqrt{S_{uu}^{\text{zpf}}(f_R)} = 45$ fm/ $\sqrt{\text{Hz}}$. With the above responsivity, the zero-point fluctuations of a single suspended nanotube segment result in a flux noise in the SQUID of $16 \mu\Phi_0/\sqrt{\text{Hz}}$.

S6 ESTIMATES OF COUPLING FOR A NANOTUBE TRANSMON QUBIT

The zero-phonon coupling rate g is given by the shift in the energy levels of the qubit in response to the zero-point fluctuations of the nanotube position [4, 5]. The zero point fluctuations of $u_{\text{zpf}} = 3.6$ pm together with the responsivity of 0.35 $m\Phi_0/\text{pm}$ gives a corresponding flux shift of $\Phi_{ZPF} = 1.3$ $m\Phi_0$. In the transmon limit, where the charging energy is much smaller than the Josephson energy ($E_C \ll E_J$), the energy splitting of the qubit is given by [6]:

$$E_{01} \approx \sqrt{8E_J E_C} \quad (4.10)$$

A small change in the qubit energy due to a change in the Josephson energy is then given by:

$$\delta E_{01} = \frac{E_{01}}{2} \frac{\delta E_J}{E_J} \quad (4.11)$$

We now need to estimate δE_J in response to the Φ_{ZPF} above. Our SQUID shows a near complete suppression of the critical current as a function of flux, allowing us to estimate the change in E_J on the slope of the flux oscillation as

$$\frac{dE_J}{d\Phi} \approx \frac{E_J^{\text{max}}}{0.5\Phi_0} \quad (4.12)$$

The coupling rate g , given by the shift of the qubit energy in response to the zero point fluctuations of the nanotube position, can then be estimated as:

$$g = \delta E_{01}^{\text{ZPF}} \approx \frac{E_{01}}{2} \frac{\Phi_{ZPF}}{0.5\Phi_0} \quad (4.13)$$

Assuming E_{01} is designed to be 6 GHz, and using $\Phi_{ZPF} = 1.3$ $m\Phi_0$, we estimate the coupling to be $g = 7$ MHz.

REFERENCES

- [1] Hüttel, A. *et al.* Carbon nanotubes as ultrahigh quality factor mechanical resonators. *Nano Lett.* **9**, 2547–2552 (2009).
- [2] Sapmaz, S., Blanter, Y., Gurevich, L. & Van Der Zant, H. Carbon nanotubes as nanoelectromechanical systems. *Physical Review B* **67**, 235414 (2003).
- [3] Poot, M. & van der Zant, H. Mechanical systems in the quantum regime. *Phys. Rep.* **511**, 273–335 (2012). URL <http://www.sciencedirect.com/science/article/pii/S0370157311003644>.
- [4] LaHaye, M., Suh, J., Echternach, P., Schwab, K. & Roukes, M. Nanomechanical measurements of a superconducting qubit. *Nature* **459**, 960–964 (2009).
- [5] Chan, J. *et al.* Laser cooling of a nanomechanical oscillator into its quantum ground state. *Nature* **478**, 89–92 (2011).
- [6] Koch, J. *et al.* Charge-insensitive qubit design derived from the cooper pair box. *Phys. Rev. A* **76**, 042319 (2007).

5

ENHANCED MECHANICAL TRANSDUCTION WITH A SUSPENDED CARBON NANOTUBE JOSEPHSON JUNCTION

We study the detection of the mechanical oscillation of a suspended carbon nanotube Josephson junction. A suspended nanotube contacted by superconducting electrodes acts as both a mechanical resonator and a superconducting weak link. Exciting the mechanical mode, we observe a strongly enhanced mechanical mixing signal due to nonlinearities of the superconducting junction. These nonlinearities, absent in devices without superconducting contacts, arise from subgap states formed in the ballistic channel. Future experiments with normal metal contacts could shed light on the states that enable the observed enhanced transduction of mechanical motion.

Nanomechanical resonators are promising applications for mass sensing[1, 2], force sensing[3], and potentially for exploring quantum motion of macroscopic objects[4]. Nanomechanical resonators made from suspended carbon nanotubes are attractive for such applications: they have very low mass, large mechanical quality factors and resonate at high frequencies. Using the nanotube itself as a mixer, this high frequency motion can be converted into low frequency voltages and currents, a technique used extensively to sense nanotube motion in suspended nanotube transistors[5] and quantum dots[6]. By contacting nanotubes with superconducting metals, one can make Josephson junctions via the proximity effect[7–9]. Making suspended carbon nanotubes with superconducting contacts[10, 11], one can also couple displacements to supercurrents through then nanotube junction, an approach that could theoretically reach the quantum limit of position sensitivity. In order to understand the feasibility of such approaches, it is important to understand the coupling of motion to supercurrents in such suspended nanotube Josephson junctions.

Here, we study the mechanical response of a suspended carbon nanotube with superconducting contacts. For hole-doping, the nanotube channel is highly conducting, and we observe a strong gate modulation of the critical current. Exciting the nanotube with an AC voltage, we observe an enhanced mechanical transduction at low bias currents that can lead to an order of magnitude enhancement of a mixing-type mechanical transduction compared to high bias currents. We find that the enhanced transduction arises strong nonlinearities in the current-voltage characteristics of the superconducting junction, acting as a probe of proximity effect superconductivity in the ballistic limit.

A SEM image of a typical device is shown in Fig. 5.1(a). The device fabrication is given in detail in[11]. The device is fabricated in a SQUID geometry in which a single nanotube falls across two trenches. The measurements presented here are performed at zero magnetic field, in which mechanical motion does not modulate the flux in the SQUID. Measurements are performed in a He3/He4 dilution refrigerator at a base temperature of 25 mK. The sample is configured in a four-terminal geometry (Fig. 5.1(b)) in which a bias current I is applied to the junction with a current source and the resulting voltage across the junction V is measured using a low-noise DC voltage amplifiers. All wiring to the junction is filtered using both cold RC filters and copper-powder filters, and enclosed in a copper can which acts as an electrical shield. Additionally, a RF antenna consisting of a open-ended coaxial cable is inserted into the copper can in order to drive the mechanical resonance.

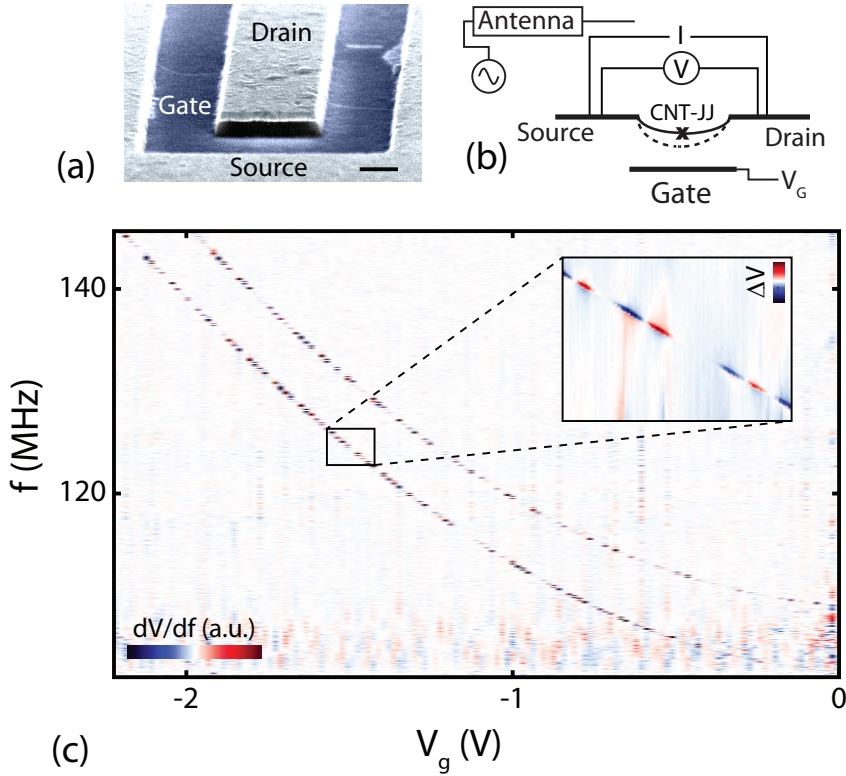


FIGURE 5.1: **Device and basic characterisation** (a) A scanning electron microscope (SEM) image of a typical device, showing a single nanotube falling across two trenches 800 nm wide. The source and drain electrodes are made from a superconducting MoRe alloy. Scale bar: 500 nm. (b) Schematic of the measurement setup. The device is biased with a current I from a current source and the voltage across the junction V is measured with a low-noise voltage amplifier. A radio frequency (RF) signal at frequency f and power P is applied to a nearby antenna in order to excite the mechanical resonance. (c) A colour-scale plot of dV/df as function of gate voltage at $I = 0$ and $P = -13$ dBm driving power, showing two mechanical resonances corresponding to the two suspended nanotube segments. The inset shows a zoomed plot of the ΔV , the difference between the resonant and non-resonance measured voltage, for the resonance studied here. The range of the colour-scale for the inset is $\pm 3 \mu V$.

Figure 5.1(c) shows mechanical resonances signals detected by measuring DC signals from the device as a function of the RF drive frequency and gate voltage. In the figure, two closely spaced mechanical resonances are observed running parallel to each other: as these are too closely spaced to be different mechanical modes, we interpret these as the separate mechanical resonance of each suspended segment of the nanotube. As experiments discussed here are performed at zero magnetic field, exciting the mechanical resonance of one of the nanotube segments does not modulate the flux through the SQUID, but is instead detected by its modulation of the normal state conductance of the nanotube segment that is resonating. Here, we will focus on the mechanical resonance of one of the two nanotube segments, shown in the inset of Fig. 5.1(c).

In previous works with similar DC detection schemes with quantum dots[6] without superconducting leads, we found that the dominant mechanism of mechanical detection was through a DC current arising from a ‘rectification’ of an effective AC voltage δV_g^{eff} coupled to the gate of the device, where δV_g^{eff} includes effects of both the AC voltages on the gate and the mechanical motion. In a current biased measurement such as performed here, the resulting mechanical signal becomes:

$$\Delta V^r = \frac{\partial^2 R}{\partial V_g^2} (\delta V_g^{eff})^2 I, \quad (5.1)$$

where ΔV^r is the mechanically induced change in the measured voltage V , I is the applied bias current, and R is a gate voltage dependent resistance.

In Fig. 5.2, we explore the mechanical transconduction signal in a suspended nanotube Josephson junction. Figure 5.2(a) shows the junction resistance $R = V/I$ at $I = 20$ nA (red curve), and the junction critical current I_c , as a function of gate voltage (blue curve). Both V/I and I_c oscillate as a function of gate voltage due to the modulation of the normal-state resistance of the nanotube channel. We will focus on the detection of the mechanical resonance signal at gate voltages corresponding to the slope between maximum at minimum critical current (triangle in Fig. 5.2(a)).

The red curve Fig. 5.2(b) shows the mechanical resonance signal change in voltage as a function of frequency f at $V_g = -1.478$ V and $I = 0$. In contradiction to the expectations of eq. 5.1, the mechanical signal at $I = 0$ does not vanish but remains finite. Furthermore, in the measurement at $I = 16$ nA (blue curve), the mechanical resonance is not visible at all, thus lower than the noise floor of $0.25 \mu\text{V}$. This is shown in more detail in the colour-scale plot of ΔV vs. I and f shown in Fig. 5.2(c). The data in Fig. 5.2(c) also contradicts eq. 5.1 in two additional ways: first, eq. 5.1 predicts a signal that will invert sign with the polarity of I , while the signal in the data in Fig. 5.2(c) has the same sign for positive and neg-

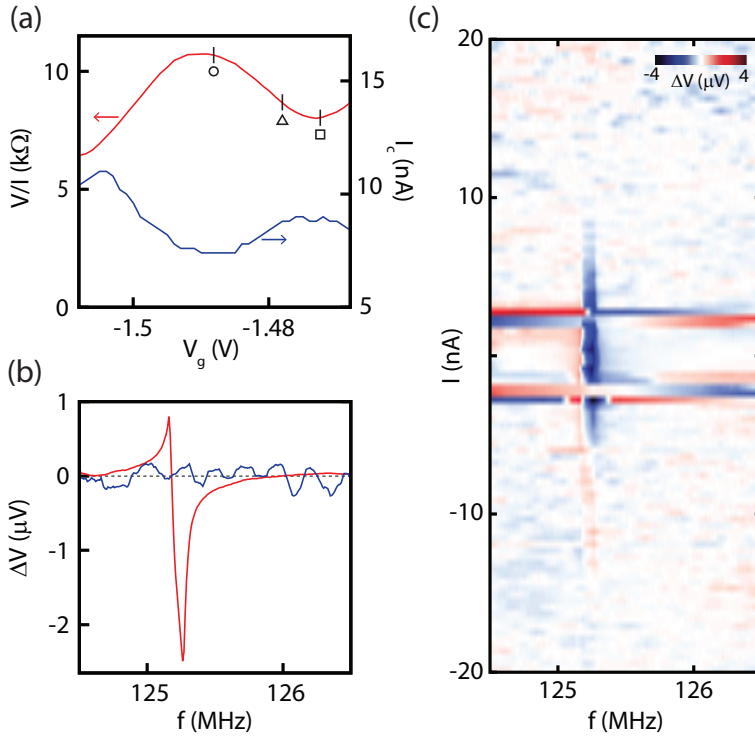


FIGURE 5.2: **Voltage response of the device with frequency, gate and current bias.** (a) Junction resistance V/I at a $I = 20$ nA (red) and junction critical current I_c (blue) as a function of gate voltage V_g . The vertical lines indicate $V_g = -1.488$ V (circle), $V_g = -1.478$ V (triangle), and $V_g = -1.4725$ V (square). As a function of V_g , both V/I and I_c oscillate due to the gate modulation of the normal state resistance of the nanotube channel. (b) ΔV as a function of drive frequency f for $I = 0$ nA (red) and $I = 13$ nA (blue) at $V_g = -1.478$ V. ΔV is defined as $\Delta V = V - V_0$, where V_0 is the measured voltage at f away from the mechanical resonance. At $I = 0$, there is a clear mechanical resonance, while at $I = 13$ nA, the resonance signal is no longer visible. (c) Colour-scale plot of ΔV as a function of f and I at $V_g = -1.478$ V (vertical line indicated by a triangle in (a)). At low bias, a clear mechanical resonance is visible, while at high bias, the resonance disappears. The two horizontal lines in the data at $I \sim \pm 3$ nA correspond to bias currents where a non-zero time-averaged supercurrent in the form of a Shapiro-step like plateau that survives the DC bias voltage and strong RF driving is applied to the junction.

ative I . Second, V_g is chosen on the slope between minimum and maximum R where the curvature $\partial^2 R / \partial V_g^2$ vanishes: according to eq. 5.1, the mechanical signal should vanish here for all values of I . The mixing signal at low bias (red curve) is $2.5 \mu\text{V}$, indicating an enhancement of the mechanical mixing signal in the (red curve) by at least a factor of 10.

To address the discrepancy with the experiment, we first note that the model in eq. 5.1 assumes that the AC voltage from the antenna couples only to the gate of the device. In practice, however, the antenna couples via asymmetries in the crosstalk capacitances to the DC wires[12], and will therefore also introduce an AC bias δI across the junction. In previous measurements, the effect of this AC bias across the junction was found to be negligible. Including this contribution, an additional contribution ΔV^m will arise that is similar to that used in two-source mixing experiments[5], but now at DC:

$$\Delta V^m = \frac{\partial R}{\partial V_g} \delta V_g^{eff} \delta I \quad (5.2)$$

Such a term has the same sign for positive and negative I , and does not vanish at $I = 0$, suggesting that the signal we present in Fig. 5.2(c) from such DC mixing type. A remaining discrepancy, however, is that eq. 5.2 would predict that the signal should be independent of I , whereas the signal shown in Fig. 5.2(c) is strong at low bias currents, but then vanishes at large bias currents.

Until now, we have considered only the case where the junction is acting only as resistor: in particular, we have not considered supercurrents through the junction, which should give rise to a zero-resistance branch of the junction IV curve. While this is not justified for junctions with no RF irradiation, under the large and low-frequency RF excitation we use here to excite the mechanical resonator, the junction IV curves, shown in Fig. 5.3, no longer show any signs of supercurrent. This can be understood from the behaviour of Josephson junctions exposed to RF radiation[13]. For high frequencies ($\hbar\omega > kT$), the IVs would show a staircase of Shapiro steps with plateaus at voltages $V = n\hbar\omega/2e$ with a slope corresponding to the sub-gap resistance. For the low frequencies used here, $\hbar\omega \ll kT$, these plateaus are no longer resolved due to thermal broadening. Thus, we can effectively treat the device as a resistor, neglecting effects of time-averaged supercurrent. We find this holds for nearly all bias currents, aside from a small residual plateau-like feature visible at $I \approx 5 \text{ nA}$ in Fig. 5.3(b) and at $I \approx 3 \text{ nA}$ in Fig. 5.2(c).

Neglecting supercurrent effects, the enhanced mechanical mixing signal at low bias currents shown in Fig. 5.2(c) can be understood by looking at the IV curves of the nanotube SNS junctions at different gate voltages, shown in Fig. 5.3. Figure 5.3(a) shows the IV of the RF driven junction at a gate voltage of $V_g = -1.488 \text{ V}$, near the minimum critical current (circle in Fig. 5.2 (a)). Particularly striking is the

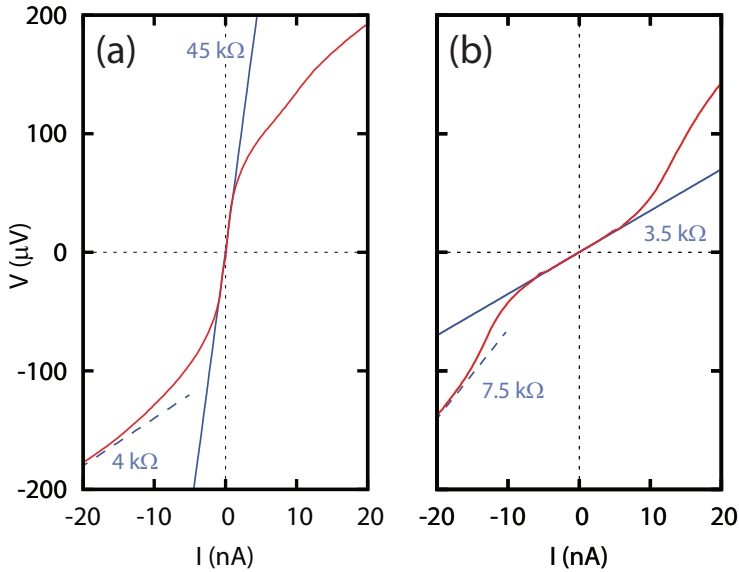


FIGURE 5.3: (a) IV curve (red line) of the driven suspended nanotube Josephson junction at $V_g = -1.488$ V near the minimum I_c (circle in Fig. 5.2(a)). Solid (dashed) blue line: slopes corresponding to 45 k Ω (4 k Ω) resistance. (b) IV curve (red line) at $V_g = -1.4725$ V near the maximum I_c (square in Fig. 5.2(a)). Solid (dashed) blue line: slopes corresponding to 3.5 k Ω (7.5 k Ω) resistance. The driven junction shows a significantly enhanced modulation of the resistance for $V < 80$ μ V, resulting in an enhanced detection of the mechanical resonance signal.

steep slope of the IV curve for $V < 100$ μ V, corresponding to a differential resistance of 50 k Ω at low bias currents. For gate voltages corresponding to the maximum critical current ($V_g = -1.4725$ V, square in Fig. 5.2(a)), the IV curve shows a resistance of 3.5 k Ω at low bias currents. At high bias, the slope of the IV curve is very similar at the two gate voltages. The net effect is that the resistance of the nanotube Josephson junction shows considerably more modulation with gate voltage (45 k Ω to 5 k Ω) for low bias currents than for high bias currents (8 k Ω to 4 k Ω), and it is this that results in the enhanced mechanical mixing signal we observe.

This can also be seen clearly in a plot of the differential resistance dV/dI of the junction as a function of bias current and gate voltage, shown in Fig. 5.4(a). Signatures of residual time-averaged supercurrent can be seen as a narrow, gate dependent band of suppressed differential resistance (dark blue), as well as a

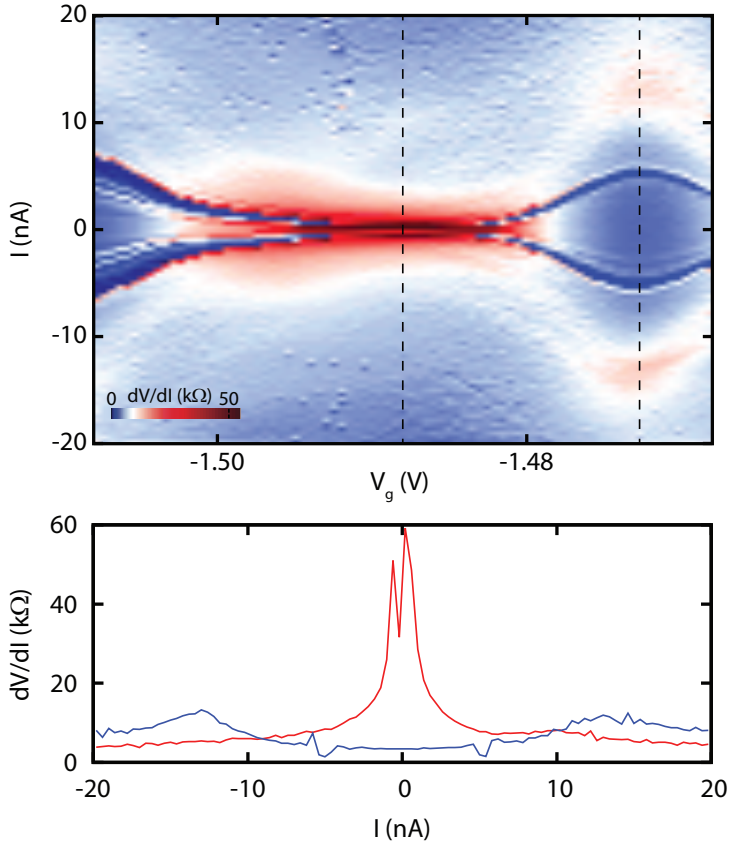


FIGURE 5.4: (a) Differential resistance dV/dI of the driven junction as a function of V_g and I . As can be seen in the IVs in Fig. 5.3, the junction shows a significantly enhanced modulation of the differential resistance at low bias currents. Two bands of small dV/dI along with some sharp lines slightly below the bands originate from non-vanishing time-averaged supercurrent (see text for further discussion). Dashed lines indicate positions of line cuts shown in (b). (b) Vertical line cuts showing dV/dI vs. I for $V_g = -1.488$ V (red line) and $V_g = -1.4725$ V (blue line).

few sharp lines occasionally occurring below this band, both of which are weak surviving Shapiro-step like features. In addition to these, there are also much broader features in the dV/dI plot, such as the red patch near zero bias between $V_g = -1.50$ and $V_g = -1.48$ V, and a broad feature around $V_g = -1.475$ V at larger bias ($I \sim 14$ nA). In Fig. 5.4(b), we show line cuts of dV/dI vs I for $V_g = -1.488$ and $V_g = -1.4725$, corresponding to the IV curves show in Fig. 5.3. Note that at even the highest bias currents in the plot, $I = 20$ nA, the voltage $V \approx 200$ μ V across the junction is still much smaller than the superconducting gap ($\Delta = 1.37$ meV for $T_C = 4.5$ K).

We would like to emphasise that nonlinearities on the 80 μ V scale are not a feature off the normal-state IV curve of the nanotube. The highly transparent contacts of the nanotube to the source and drain lead imply that the normal state junction would be deep in the Fabry-Pérot regime of conductance, and would only begin to show non-linearities of its IV characteristics on the energy scale of the confinement energy $h\nu_F/L \sim 2.1$ meV for a 800 nm long trench. By suppressing superconductivity in the junction with a magnetic field, the IV of the nanotube is linear up to mV voltages, allowing us to exclude the normal state conductance as an origin of the nonlinearities in the IV that we observe. Instead, these nonlinearities arise from the subgap features of the superconducting nanotube junction, resulting in an enhanced transduction giving a large low-bias mechanical mixing signal.

While the enhanced mechanical mixing signal is clearly understood phenomenologically from the features of the IV curves, the microscopic origin of these features is difficult to ascertain in our experiment. In particular, superconducting junctions are known to host a wide range of features in their IV characteristics, such as Shapiro steps, self-induced steps such as Fiske steps[14], photon-assisted tunnelling[13], multiple Andreev reflection[15–17] and Andreev bound states[18]. To distinguish between these, however, a realistic model of the driven nanotube superconducting junction in the finite voltage state would be required.

From the perspective of modelling, the device we study here presents an new interesting parameter regime: in particular, in contrast to recently studied nanowire junctions, nanotube junctions represent an extreme clean limit where the ballistic length is much longer than the junction length, and in which are in the extreme single-sub-band limit, with higher transverse sub-bands are separated in energy by hundreds of meV. Our device is also in an interesting limit in that many of the relevant energy scales are comparable: the single-particle level spacing is $h\nu_F/L \sim 2.1$ meV, the superconducting gap is $\Delta \sim 1.37$ meV, and the tunnel coupling to the leads is $\Gamma \sim 1.0$ meV. From measurements in the Coulomb blockade regime, the charging energy of the 800 nm suspended nanotube segment is considerably larger than any of these ($E_C \sim 20$ meV), although charge quantisation is suppressed in the

Fabry-Pérot regime due to quantum fluctuations with the leads. This coincidence of many energy scales, however, presents a challenge for the modelling of subgap states in our junctions.

While modelling our junction may be challenging, an understanding of the subgap states that give rise to the enhanced Josephson transconductance could potentially be achieved by studying nanotube devices with one superconducting contact and one normal metal contact, as has been recently studied in nanowire and semiconductor quantum dot experiments. The use of a normal metal contact to act as a weakly coupled tunnel probe [18–20] considerably simplifies the interpretation of the IV characteristics as it avoids effects of oscillating junction phases from the AC Josephson effect in the spectroscopy of the junction. For such devices, nanotubes could present some significant advantages: in particular, using multiple gates, it is possible to tune the transparency of tunnel junctions in these clean nanotubes with exquisite precision [21, 22]. By making such hybrid N/S devices, it could be possible to study in more detail the proximity-effect superconductivity in these ballistic single-channel devices, and potentially understand the microscopic origin of the observed Josephson transconductance and mechanical mixing signals.

We can further test the device capabilities of amplifying an signal. To do this, two radio frequencies should be applied to the N/S hybrid device, while measuring an AC voltage across the device. One antenna, which prepares the nonlinearities in the device (shapirosteps at low frequencies), and a second, weak probe signal to the gate, which mixes with the mechanical motion of the CNT (thermally driven) at a difference frequency.

REFERENCES

- [1] K. Jensen, K. Kim, and A. Zettl, *An atomic-resolution nanomechanical mass sensor*, *Nature Nanotech.* **3**, 533 (2008).
- [2] J. Chaste, A. Eichler, J. Moser, G. Ceballos, R. Rurali, and A. Bachtold, *A nanomechanical mass sensor with yoctogram resolution*, *Nature Nanotech.* **7**, 301 (2012).
- [3] C. A. Regal, J. D. Teufel, and K. W. Lehnert, *Measuring nanomechanical motion with a microwave cavity interferometer*, *Nature Phys.* **4**, 555 (2008).
- [4] K. C. Schwab and M. L. Roukes, *Putting mechanics into quantum mechanics*, *Physics Today* **58**, 36 (2005).
- [5] V. Sazonova, Y. Yaish, H. Üstünel, D. Roundy, T. A. Arias, and P. L. McEuen,

- A tunable carbon nanotube electromechanical oscillator*, Nature **431**, 284 (2004).
- [6] A. K. Hüttel, G. A. Steele, B. Witkamp, M. Poot, L. P. Kouwenhoven, and H. S. J. van der Zant, *Carbon nanotubes as ultrahigh quality factor mechanical resonators*, Nano Lett. **9**, 2547 (2009).
- [7] A. F. Morpurgo, J. Kong, C. M. Marcus, and H. Dai, *Gate-controlled superconducting proximity effect in carbon nanotubes*, Science **286**, 263 (1999).
- [8] A. Y. Kasumov, R. Deblock, M. Kociak, B. Reulet, H. Bouchiat, I. I. Khodos, Y. B. Gorbatov, V. T. Volkov, C. Journet, and M. Burghard, *Supercurrents through single-walled carbon nanotubes*, Science **284**, 1508 (1999).
- [9] P. Jarillo-Herrero, J. A. Van Dam, and L. P. Kouwenhoven, *Quantum supercurrent transistors in carbon nanotubes*, Nature **439**, 953 (2006).
- [10] B. Reulet, A. Y. Kasumov, M. Kociak, R. Deblock, I. I. Khodos, Y. B. Gorbatov, V. T. Volkov, C. Journet, and H. Bouchiat, *Acoustoelectric effects in carbon nanotubes*, Phys. Rev. Lett. **85**, 2829 (2000).
- [11] B. H. Schneider, S. Etaki, H. S. J. van der Zant, and G. A. Steele, *Coupling carbon nanotube mechanics to a superconducting circuit*, Sci. Rep. **2** (2012).
- [12] H. B. Meerwaldt, G. Labadze, B. H. Schneider, A. Taspinar, Y. M. Blanter, H. S. J. van der Zant, and G. A. Steele, *Probing the charge of a quantum dot with a nanomechanical resonator*, Phys. Rev. B. **86**, 115454 (2012).
- [13] M. Tinkham, *Introduction to superconductivity* (McGraw Hill (New York), 1996).
- [14] D. D. Coon and M. D. Fiske, *Josephson ac and step structure in the supercurrent tunneling characteristic*, Phys. Rev. **138**, A744 (1965).
- [15] M. R. Buitelaar, W. Belzig, T. Nussbaumer, B. Babic, C. Bruder, and C. Schönenberger, *Multiple Andreev reflections in a carbon nanotube quantum dot*, arXiv preprint cond-mat/0304233 (2003).
- [16] E. Vecino, M. R. Buitelaar, A. Martín-Rodero, C. Schönenberger, and A. Levy Yeyati, *Conductance properties of nanotubes coupled to superconducting leads: signatures of Andreev states dynamics*, Solid State Commun. **131**, 625 (2004).

- [17] A. Eichler, M. Weiss, S. Oberholzer, C. Schönenberger, A. L. Yeyati, J. C. Cuevas, and A. Martín-Rodero, *Even-odd effect in Andreev transport through a carbon nanotube quantum dot*, Phys. Rev. Lett. **99**, 126602 (2007).
- [18] J. D. Pillet, C. H. L. Quay, P. Morfin, C. Bena, A. L. Yeyati, and P. Joyez, *Andreev bound states in supercurrent-carrying carbon nanotubes revealed*, Nature Phys. **6**, 965 (2010).
- [19] W. Chang, V. E. Manucharyan, T. S. Jespersen, J. Nygård, and C. M. Marcus, *Tunneling Spectroscopy of Quasiparticle Bound States in a Spinful Josephson Junction*, Phys. Rev. Lett. **110**, 217005 (2013).
- [20] A. Kumar, M. Gaim, D. Steininger, A. L. Yeyati, A. Martín-Rodero, A. K. Huettel, and C. Strunk, *Temperature dependence of Andreev spectra in a superconducting carbon nanotube quantum dot*, arXiv preprint arXiv:1308.1020 (2013).
- [21] G. A. Steele, G. Gotz, and L. P. Kouwenhoven, *Tunable few-electron double quantum dots and Klein tunnelling in ultraclean carbon nanotubes*, Nature Nanotech. **4**, 363 (2009).
- [22] J. Waissman, M. Honig, S. Pecker, A. Benyamini, A. Hamo, and S. Ilani, *Realization of pristine and locally tunable one-dimensional electron systems in carbon nanotubes*, Nature Nanotech. **8**, 569 (2013).

6

DECOHERENCE IN A CARBON NANOTUBE MECHANICAL RESONATOR

In physical systems, decoherence originates from dissipative and dephasing processes. In mechanical resonators, the driven frequency response measures a combination of both, while time domain techniques can separate the two. We report on time domain ringdown measurements of a carbon nanotube mechanical resonator at low temperatures. Comparing frequency and time domain measurements of the mechanical quality factor, we find a spectral quality factor four times smaller than that measured in ringdown, demonstrating dephasing induced decoherence of the nanomechanical motion. This decoherence is seen to arise at high driving powers, pointing to a non-linear dephasing mechanism. Our results highlight the importance of time-domain techniques for understanding dissipation in nano-mechanical resonators, and the relevance of decoherence mechanisms in nanotube mechanics.

6.1 INTRODUCTION

Dissipation and decoherence are fundamentally different processes that can play a role in mechanical resonators. The distinction between decoherence and dissipation[1–3] is often overlooked when studying the Q factor of a mechanical resonator. The mechanical response is typically characterised by the quality factor Q , which is measured from either a spectral response or by a ringdown measurement. In a spectral response measurement, the driving frequency of the resonator is swept and the steady-state oscillation amplitude is measured. From the width of the response peak, Q factor is extracted. In a ringdown measurement, Q is determined by the envelope of the transient of the resonator after a driving force is switched off.

Despite the fact that they are both given the same symbol Q , the quality-factor as obtained from these two types of measurements are sensitive to different physical processes. The quality-factor measured in the spectral response, Q_S , is sensitive to both dissipation (energy loss) and pure dephasing (such as fluctuations of the resonators resonance frequency), similar to T_2 time in a Ramsey experiment with a qubit[4]. The quality factor Q_R measured in a ringdown experiment is sensitive only to dissipation (energy loss), similar to a T_1 measurement on a qubit[5]. In qubits, it is well-known that the T_1 and T_2 can be very different: an extreme example is a GaAs spin qubit, in which T_2 can be as short as 10 ns, while T_1 can be as long as 1 s[6, 7].

Decoherence in mechanical resonators has been studied earlier in a piezoelectric resonator coupled to a superconducting circuit[8], recently in atomically thin drum resonators[9] and two coupled modes of a mechanical resonator[10]. In these experiments, no pure dephasing was observed and the coherence of the motion was limited by dissipation. In experiments with mass sensing[11], excess phase noise was observed that which was attributed to surface diffusion of molecules[12]. In comparison to NEMS, carbon nanotube resonators are very sensitive to their environment. Due to a low mass and spring constant, nanotube mechanical resonators show a strong dispersion with the gate voltage[13] are sensitive to the force of a single electron charge[14, 15], exhibit strong mode coupling[16, 17], and strong nonlinearities[18]. These strong coupling effects may give rise to dephasing, making them an interesting candidate for exploring mechanical decoherence.

Currently mechanical dissipation in carbon nanotubes is not well understood. It has been proposed that low Q factors could originate from thermal induced spectral broadening[19], clamping losses[20–22], or from symmetry breaking[23]. Until now, reports of the quality factor in carbon nanotubes have been based only on spectral measurements [14, 18, 24]. To distinguish dissipation processes from dephasing, additional measurements, such as a mechanical ringdown must be

performed.

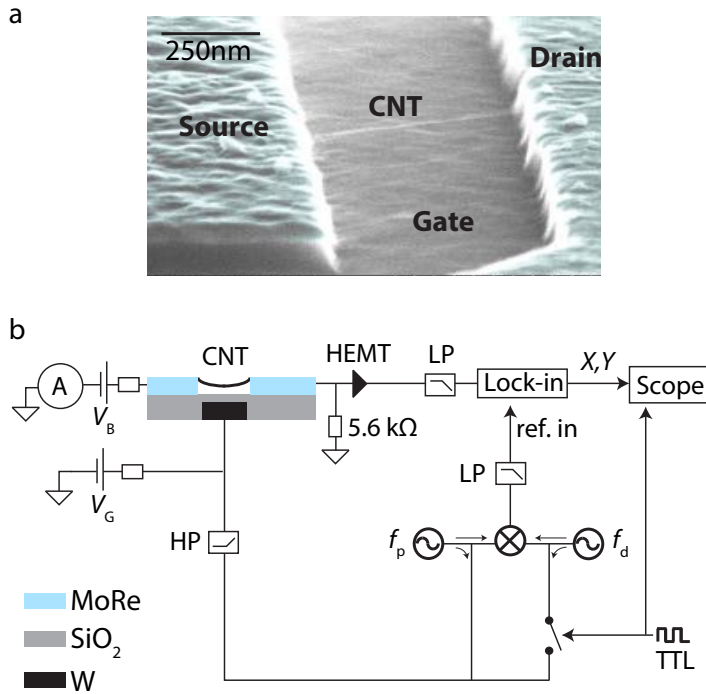


FIGURE 6.1: Device and measurement setup **a** Colorised scanning electron microscope image of a typical device, showing a suspended CNT in contact with source and drain electrodes. **b** Schematics of the measurement setup. Two frequency signal generators are used: one for the drive and one for the probe signal. The probe signal is 7 MHz detuned from the drive signal. A switch is used to turn on and off the drive signal to the gate. A mixing signal is generated with a mixer at room temperature which serves as a reference signal for the lock-in amplifier. At the CNT at 2 K, a second mixing signal is generated, which is impedance matched by a HEMT and detected by a lock-in amplifier. The X and Y quadrature outputs from the lock-in are recorded in sync with the switch by an oscilloscope.

Here, we use a recently developed fast detection scheme to measure the ring-down of a carbon nanotube mechanical resonator[25]. Doing so, we gain access to both the dissipation and decoherence processes in a carbon nanotube. At low driving power, we find that Q_S and Q_R have the same value, indicating that dephasing processes are not significant. At higher driving power, however, we find that spectral response becomes significantly broader, with a drop in Q_S by a factor of four, while Q_R remains constant. This demonstrates that non-linear dephasing and decoherence can have a strong effect on the spectral line width of a nanomechanical

resonator.

6.2 RESULTS

A suspended single-walled carbon nanotube (CNT) mechanical resonator is fabricated as described previously[25]. Briefly, fabrication starts with an intrinsic silicon wafer, on which a gate electrode is patterned. On top, a 200 nm thick silicon oxide layer is deposited, followed by 70 nm thick MoRe source and drain electrodes. Finally, a CNT is grown across the 500 nm trench that separates the electrodes. The distance between the gate and the CNT is 270 nm. Figure 6.1(a) shows a scanning electron microscope (SEM) image of the device. Figure 6.1b shows the schematic of the circuit used to measure the conductance of the CNT as a function of gate voltage (Fig. 6.2a). A high conductance is observed for negative gate voltages, when the CNT is doped with holes. When a positive gate voltage is applied, a low conductance region (small band gap) is followed by weak conductance oscillations due to Coulomb blockade. This overall behaviour is typical for a clean single CNT in contact with MoRe electrodes[26].

To find the mechanical resonance and to characterise its gate dependence, we first measure the nanotube motion using the rectification technique outlined in Ref.[15]. Figure 6.2b shows the current as a function of frequency f_d and V_G at a bias voltage of 1 mV. The frequency at which the mechanical signal is detected shows a quadratic dependence with gate voltage, tuning the fundamental mode frequency between 300 and 315 MHz. This behaviour is characteristic for a carbon nanotube mechanical resonator[13].

In figure 6.3, we measure response of the mechanical resonator in the time domain. The schematic of the detection circuit used here is shown in Fig. 6.1b. Two signal generators are used to generate a drive (f_d) and a probe (f_p) signal. The probe signal is 7 MHz detuned from the drive frequency and a mixer is used to generate a 7 MHz reference signal for the lock-in. The CNT resonator is driven by applying the drive and probe signals to the gate. The transconductance of the CNT leads to the mixing of these two signals. Note that this is slightly different than conventional two-source mixing where one signal is applied to the source and the other to the gate. At cryogenic temperatures the nonlinear response of the nanotube conductance with gate voltage $G(V_G)$ allows us to use a similar mixing-type detection [13] with only applying signals to the gate. To impedance match a signal coming from the nanotube, a HEMT is located in close proximity to the CNT, so that the motion can be detected with a bandwidth of 62 MHz[25]. Here we use a high-frequency lock-in amplifier to detect the signal from the HEMT amplifier, in which case our readout scheme can detect motion on μs timescales.

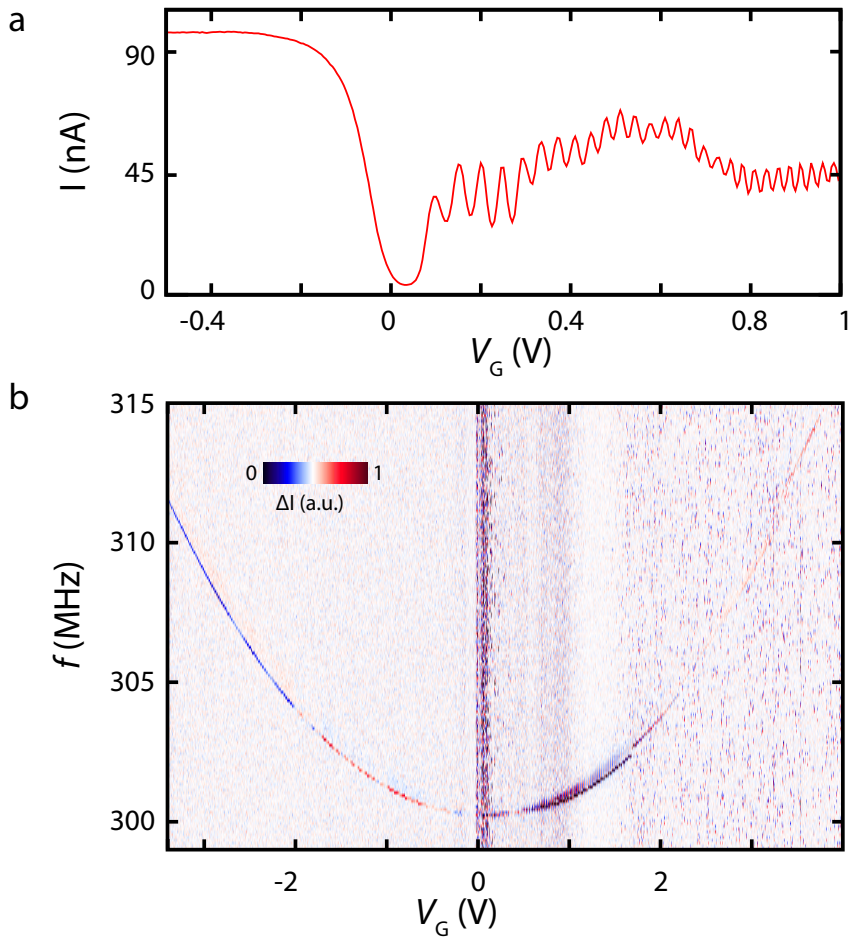


FIGURE 6.2: Device characterisation. **a** Conductance as a function of gate voltage, V_G , at 2 Kelvin and at $V_B = 4$ mV. For $V_G < 0$ V the conductance is high while for $V_G > 0$ V the conductance is low, exhibiting weak Coulomb blockade. **b** Resonance frequency as a function of gate voltage, showing that the suspended CNT acts as a gate tuneable mechanical resonator.

To measure the mechanical ringdown, we use the following pulsed excitation and measurement scheme. A switch in the circuit controls the drive signal (f_d) which is connected to the gate of device. With the switch on, the CNT resonator is driven. When the switch is turned off, only the probe and the mechanical resonance signal are present. These two signals are mixed by the CNT, and the resulting signal is amplified by the HEMT and detected by the lock-in amplifier. When the switch is turned off, we use the difference frequency $f_d - f_p$ as a reference signal for the lock-in amplifier. The envelope of the mechanical ringdown signal is detected as a function of time.

Figure 6.3a shows the transient response measured by the lock-in after the CNT resonator has been driven at resonance ($f_d = f_0$). The gate voltage is fixed at $V_G = 0.4$ V. The drive signal is switched off at $t = 0$ μ s. The output quadratures from the lock-in have been averaged by repeating switch pulses (TTL pulse) applied to the microwave switch (Fig. 6.3a) turning the drive signal on and off. At the same time the quadratures of the lock-in amplifier are measured by an oscilloscope. The oscilloscope is triggered by the same (TTL) pulse which drives the switch, the quadrature components are averaged over 10000 times. The electrical mixing signal, has been subtracted, and the quadratures have been rotated (SI), such that the data represent the amplitude of the mechanical signal.

It is interesting to investigate the ringdown behaviour when the resonator is driven off-resonance[27]. In Fig. 6.3a, the red curve shows the ringdown when the drive frequency is detuned $\Delta f \sim 70$ kHz from the mechanical resonance frequency of the CNT. In this case the signal oscillates below the relative zero position while decreasing in amplitude. This oscillation frequency matches the frequency detuning relative to the mechanical resonance frequency ($\Delta f = f_0 - f$). This oscillation occurs when the mechanical resonator resonates at its own fundamental resonance frequency when the detuned driving is switched off, resulting in a mismatch in the measured and reference frequency of the lock-in amplifier.

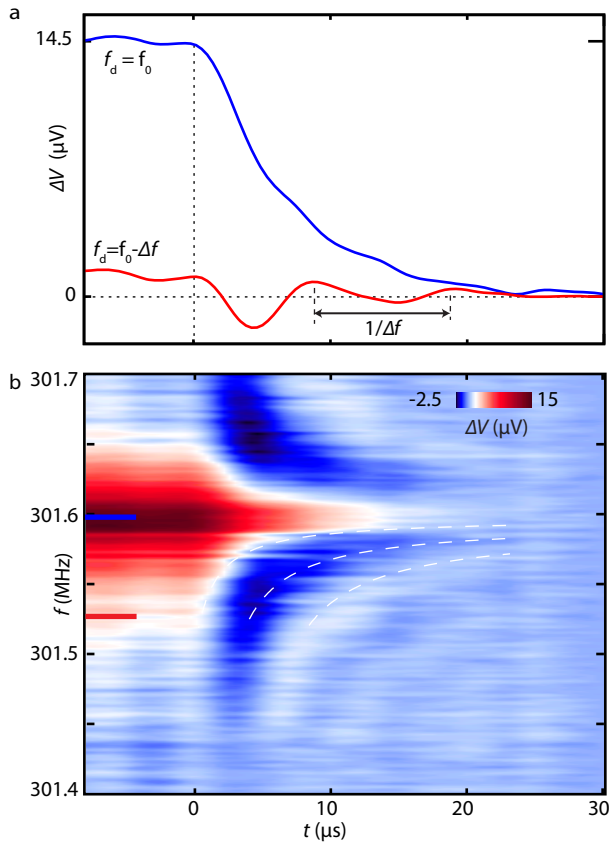


FIGURE 6.3: Time domain response of the CNT. **a** Recorded response of the lock-in amplifier when switching off the drive signal for an on resonance (blue) and off-resonance (red) drive frequency. The red curve shows the mechanical response of the CNT when the drive signal is detuned by Δf from the mechanical resonance position. An oscillation on top of the ringdown signal (for $t > 0$) is visible. The oscillation periodicity matches $P = \frac{1}{2\pi\Delta f}$. **b**, Colour-scale map of the mechanical ring-down signal as a function of time and drive frequency. A white contour on top of the colour-scale map indicates the peak and dip positions due to the detuning from the fundamental mechanical resonance frequency. The red and blue markers on the bottom indicate the positions where the line-cuts a and b are extracted from.

To further investigate this behaviour, we plot in figure 6.3b a two-dimensional colour-scale representation of the measured amplitude as a function of time and drive frequency. While keeping the gate voltage $V_G = 0.4$ V fixed we slowly step the drive and probe signal across the mechanical resonance of the CNT. For each point in frequency we record and average the X and Y quadratures with the oscilloscope. On top of the colour-scale map, a contour map with white dashed lines is shown, to indicate the positions of the peaks and dips of the ring-down signals that are recorded off-resonance. The dashed lines match the expected peak and dip positions with a periodicity of $\frac{1}{2\pi\Delta f}$, where $\Delta f = f_0 - f_d$ is the detuning relative from the mechanical resonance position. As can be seen from the 2D colour map, the dashed lines follow the peak/dip positions very well, confirming that the oscillating ringdown signal off-resonance is indeed from the mechanical resonator.

6.3 RINGDOWN Q_R FACTOR

To extract the ringdown quality factor Q_R , we fit the measured time response of device for resonant driving. An important detail is that in the experiment, the trace averaging we perform with the oscilloscope is on the amplitude quadrature. To describe the quadrature measurements, we introduce a model that includes the effects of dephasing (SI). From this model, which is constrained by the independently observed Q_S , we determine Q_R . In Fig. 6.4, we use this technique to independently extract the dephasing and dissipation contributions to the mechanical quality factor. The upper panels show the spectral response and the time domain response for a low driving power. Fitting the datasets, we find that both Q_S and Q_R are well-described by a single number ($Q_S = Q_R \sim 6250$) indicating that dephasing does not play a role at this driving power.

In the lower panel, we show the mechanical response at higher driving powers. At higher driving powers, the spectral response is still well-described by the line-shape of an harmonic oscillator (SI) with no sign of hysteresis, indicating that the amplitude of the motion is small enough that nonlinear restoring forces (which would lead to a Duffing response) are not significant. Although the response still fits well to a line-shape of an harmonic oscillator, it has significantly increased in line-width, now exhibiting a $Q_S \sim 1400$. In the right panels, we show the simultaneously measured time-domain response. What is remarkable is that although the spectral line-width has increased significantly, the ringdown response decays on a timescale comparable to the dataset at a lower power with a $Q_S \sim 6250$. Fitting the data to the model, we find $Q_R \sim 6140$, the same value found in the lower power dataset. Although increasing the drive power significantly reduces the spectral line-width Q_S , the observed value of Q_R shows that dissipation is unchanged. The observation of $Q_R \gg Q_S$ demonstrates the importance of dephasing and de-

coherence in the dynamics of the carbon nanotube motion.

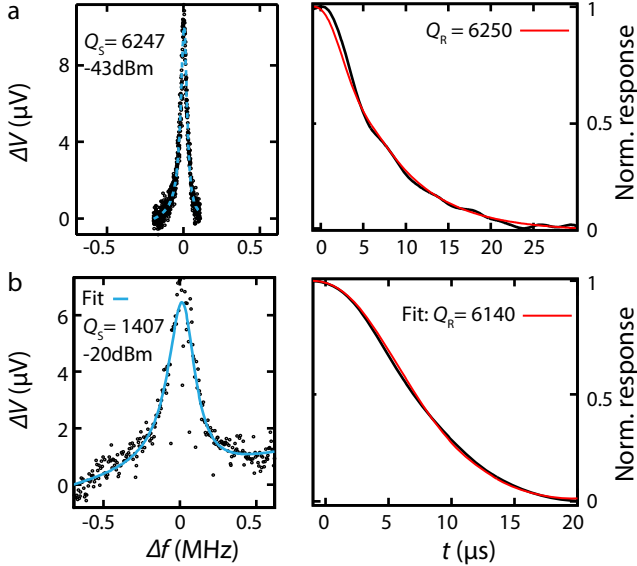


FIGURE 6.4: Measurements of the spectral and ringdown quality factors for different driving powers. The gate voltage $V_G = 0.4$ V and the temperature is 1.9 K. The drive power and fitted quality factor are indicated in the panels. In **a**, the probe power is -28 dBm and the resonance position $f_0 = 301.6$ MHz. In **b** the probe power is -8 dBm and the resonance position $f_0 = 299.69$ MHz. Note, the phase was rotated to represent the amplitude (SI) and the frequency spans were aligned.

6.4 DISCUSSIONS

In the observations presented here, dephasing appears with increased amplitude of the mechanical motion, indicating a non-linear dephasing mechanism. We note that a similar observation of an increasing spectral line-width with increased driving power was recently reported as an indication of nonlinear damping. Our results here show that such effects in the spectral quality factor Q_S can also arise from a power dependent dephasing mechanism, and that fast time-domain measurements such as those presented here are able to distinguish between the two.

Having established the presence of non-linear dephasing in our device, it is interesting to consider what mechanisms could lead to such an effect. One possible source is an excess voltage noise on our gate: since the mechanical frequency is gate voltage dependent, noise on the gate would give rise to random fluctuations in mechanical frequency, which would produce a Q_S from spectral (inhomogeneous)

broadening. From the dispersion of the mechanical frequency with gate voltage, we estimate that the gate peak to peak voltage noise needed to produce the observed spectral broadening is 45 mV. A gate voltage noise larger than the Coulomb peak spacing, is significantly higher than the noise level in our setup, suggesting we can rule out gate voltage noise as the origin of the observed effects. Another possibility is effects from the relatively weak Coulomb blockade in our device, in which fluctuating force from the tunnelling of single electrons could dephase the mechanical motion[28]. Although we did not observe any strong dependence of Q_S as the gate voltage was swept across the weak Coulomb blockade features here, future experiments at lower temperature where Coulomb blockade effects become more significant could shed light on this mechanism. A third possible source is dephasing from coupling to the stochastic motion of other mechanical modes[19, 29], which could be explored in future experiments through detailed temperature dependence studies.

In summary, we have used a high-speed readout technique to measure the mechanical ringdown of a carbon nanotube. Using this technique, we demonstrate decoherence and dissipation of the mechanical motion from an amplitude-dependent dephasing process. Future studies of motion in the time domain could potentially identify the origin of this dephasing and explore dissipation and decoherence in carbon nanotube motion.

REFERENCES

- [1] A. N. Cleland and M. L. Roukes, *Noise processes in nanomechanical resonators*, J. Appl. Phys. **92**, 2758 (2002).
- [2] F. Marquardt and A. Püttmann, *Introduction to dissipation and decoherence in quantum systems*, arXiv preprint arXiv:0809.4403 (2008).
- [3] L. G. Remus, M. P. Blencowe, and Y. Tanaka, *Damping and decoherence of a nanomechanical resonator due to a few two-level systems*, Phys. Rev. B **80**, 174103 (2009).
- [4] N. F. Ramsey, *A molecular beam resonance method with separated oscillating fields*, Phys. Rev. **78**, 695 (1950), ISSN 0031899X.
- [5] F. Bloch, *Nuclear induction*, Phys. Rev. **70**, 460 (1946), ISSN 0031899X.
- [6] J. R. Petta, A. C. Johnson, J. M. Taylor, E. A. Laird, A. Yacoby, M. D. Lukin, C. M. Marcus, M. P. Hanson, and A. C. Gossard, *Coherent manipulation of coupled electron spins in semiconductor quantum dots*, Science **309**, 2180 (2005).

- [7] S. Amasha, K. MacLean, I. P. Radu, D. M. Zumbühl, M. A. Kastner, M. P. Hanson, and A. C. Gossard, *Electrical control of spin relaxation in a quantum dot*, Phys. Rev. Lett. **100**, 46803 (2008).
- [8] A. D. O'Connell, M. Hofheinz, M. Ansmann, R. C. Bialczak, M. Lenander, E. Lucero, M. Neeley, D. Sank, H. Wang, M. Weides, et al., *Quantum ground state and single-phonon control of a mechanical resonator*, Nature **464**, 697 (2010).
- [9] R. van Leeuwen, A. Castellanos-Gomez, G. A. Steele, H. S. J. van der Zant, and W. J. Venstra, *Time-domain response of atomically thin MoS2 nanomechanical resonators*, arXiv preprint arXiv:1405.5666 (2014).
- [10] T. Faust, J. Rieger, M. J. Seitner, J. P. Kotthaus, and E. M. Weig, *Coherent control of a classical nanomechanical two-level system*, Nature Phys. **9**, 485 (2013).
- [11] Y. T. Yang, C. Callegari, X. L. Feng, and M. L. Roukes, *Surface adsorbate fluctuations and noise in nanoelectromechanical systems*, Nano Lett. **11**, 1753 (2011).
- [12] J. Atalaya, A. Isacsson, and M. I. Dykman, *Diffusion-induced dephasing in nanomechanical resonators*, Physical Review B - Condensed Matter and Materials Physics **83** (2011), ISSN 10980121, [1010.4330](#).
- [13] V. Sazonova, Y. Yaish, H. Üstünel, D. Roundy, T. A. Arias, and P. L. McEuen, *A tunable carbon nanotube electromechanical oscillator*, Nature **431**, 284 (2004).
- [14] B. Lassagne, Y. Tarakanov, J. Kinaret, D. Garcia-Sanchez, and A. Bachtold, *Coupling mechanics to charge transport in carbon nanotube mechanical resonators*, Science **325**, 1107 (2009).
- [15] G. A. Steele, A. K. Hüttel, B. Witkamp, M. Poot, H. B. Meerwaldt, L. P. Kouwenhoven, and H. S. J. van der Zant, *Strong coupling between single-electron tunneling and nanomechanical motion*, Science **325**, 1103 (2009).
- [16] A. Eichler, M. del Álamo Ruiz, J. A. Plaza, and A. Bachtold, *Strong coupling between mechanical modes in a nanotube resonator*, Phys. Rev. Lett. **109**, 25503 (2012).
- [17] A. Castellanos-Gomez, H. B. Meerwaldt, W. J. Venstra, H. S. J. van der Zant, and G. A. Steele, *Strong and tunable mode coupling in carbon nanotube resonators*, Phys. Rev. B. **86**, 41402 (2012).

- [18] A. Eichler, J. Moser, J. Chaste, M. Zdrojek, I. Wilson-Rae, and A. Bachtold, *Non-linear damping in mechanical resonators made from carbon nanotubes and graphene*, Nature Nanotech. **6**, 339 (2011).
- [19] A. W. Barnard, V. Sazonova, A. M. van der Zande, and P. L. McEuen, *Fluctuation broadening in carbon nanotube resonators*, Proceedings of the National Academy of Sciences **109**, 19093 (2012).
- [20] G. D. Cole, I. Wilson-Rae, K. Werbach, M. R. Vanner, and M. Aspelmeyer, *Phonon-tunnelling dissipation in mechanical resonators*, Nat. Commun. **2**, 231 (2011).
- [21] J. Rieger, A. Isacsson, M. J. Seitner, J. P. Kotthaus, and E. M. Weig, *Energy losses of nanomechanical resonators induced by atomic force microscopy-controlled mechanical impedance mismatching*, Nat. Commun. **5** (2014).
- [22] M. Aykol, B. Hou, R. Dhall, S.-W. Chang, W. Branham, J. Qiu, and S. B. Cronin, *Clamping Instability and van der Waals Forces in Carbon Nanotube Mechanical Resonators*, Nano Lett. (2014).
- [23] A. Eichler, J. Moser, M. I. Dykman, and A. Bachtold, *Symmetry breaking in a mechanical resonator made from a carbon nanotube*, Nat. Commun. **4** (2013).
- [24] A. K. Hüttel, G. A. Steele, B. Witkamp, M. Poot, L. P. Kouwenhoven, and H. S. J. van der Zant, *Carbon nanotubes as ultrahigh quality factor mechanical resonators*, Nano Lett. **9**, 2547 (2009).
- [25] H. B. Meerwaldt, S. R. Johnston, H. S. J. van der Zant, and G. A. Steele, *Submicrosecond-timescale readout of carbon nanotube mechanical motion*, Appl. Phys. Lett. **103**, 53121 (2013).
- [26] B. H. Schneider, S. Etaki, H. S. J. van der Zant, and G. A. Steele, *Coupling carbon nanotube mechanics to a superconducting circuit*, Sci. Rep. **2** (2012).
- [27] T. Antoni, K. Makles, R. Braive, T. Briant, P-F. Cohadon, I. Sagnes, I. Robert-Philip, and A. Heidmann, *Nonlinear mechanics with suspended nanomembranes*, Europhys. Lett. **100**, 68005 (2012).
- [28] H. B. Meerwaldt, G. Labadze, B. H. Schneider, A. Taspinar, Y. M. Blanter, H. S. J. van der Zant, and G. A. Steele, *Probing the charge of a quantum dot with a nanomechanical resonator*, Phys. Rev. B. **86**, 115454 (2012).
- [29] W. J. Venstra, R. van Leeuwen, and H. S. J. van der Zant, *Strongly coupled modes in a weakly driven micromechanical resonator*, Appl. Phys. Lett. **101**, 243111 (2012).

6.5 SUPPLEMENTARY INFORMATION

6.5.1 FABRICATION OF THE DEVICE

Local gates are the first step in the fabrication process. These are fabricated by sputtering 50 nm tungsten across the whole substrate and etching this layer using an SF₆/He plasma and using a 300 nm thick NEB-22 resist mask. The local gates are then covered under a 200 nm plasma enhanced chemical vapour deposited silicon dioxide layer. Subsequently, 35 nm molybdenum and 35 nm rhenium are co-sputtered on top. Using a four-layer etch mask source and drain electrodes are defined. After catalyst deposition and growth using chemical vapour deposition at 900°C. the CNTs are grown[1].

6.5.2 THEORY: RINGDOWN OF A RESONATOR

To understand what type of response to expect from the CNT, we analyse the response of a linear resonator with the equation of motion including damping and a driving force. The corresponding equation of motion [see also[2]] reads:

$$m\ddot{u} = -k_R u - m\dot{u}/\tau + F(T), \quad (6.1)$$

where m is the mass of the CNT with a displacement u relative to the equilibrium position, a spring constant k_R , a decay time τ and a driving force $F(T)$.

By taking the Fourier transformation ($\mathfrak{F}[x(t)] = \int_{-\infty}^{\infty} x(t) \exp(-i\omega_d t) dt$) of the equation of motion (Eq. 6.1) and the driving force $F(t) = F_0 \cos(\omega_d t)$, the following transfer function is obtained ($\omega_d = 2\pi f_d$):

$$H_{HO}(\omega_d) = k_R \frac{u(\omega_d)}{F(\omega_d)} = \frac{\omega_0^2}{\omega_0^2 - \omega_d^2 + i\omega_d \omega_0 / Q} \quad (6.2)$$

Driven response

In continuous driving with a driving force $F(t) = F_0 \cos(\omega_d t)$ a solution for the equation of motion is:

$$u(t) = X_d \cos(\omega_d t) + Y_d \sin(\omega_d t), \quad (6.3)$$

where $X_d = A \cdot \cos(\phi)$, $Y_d = -A \cdot \sin(\phi)$, $A = |H_{HO}(\omega_d)|$ and $\phi = \angle H_{HO}(\omega_d)$ is a phase angle of the response function, which gives the relative phase between the oscillating motion and the driving force. Figure 6.5 shows time and spectral response of a linear resonator with $F(t) = F_0 \cos(\omega_d t)$. In Fig. 6.5a the resonator is driven at resonance frequency. The displacement $u(t)$ lags behind the driving force $F(t)$ by a phase difference of $-\pi/2$. This phase offset between drive and displacement of

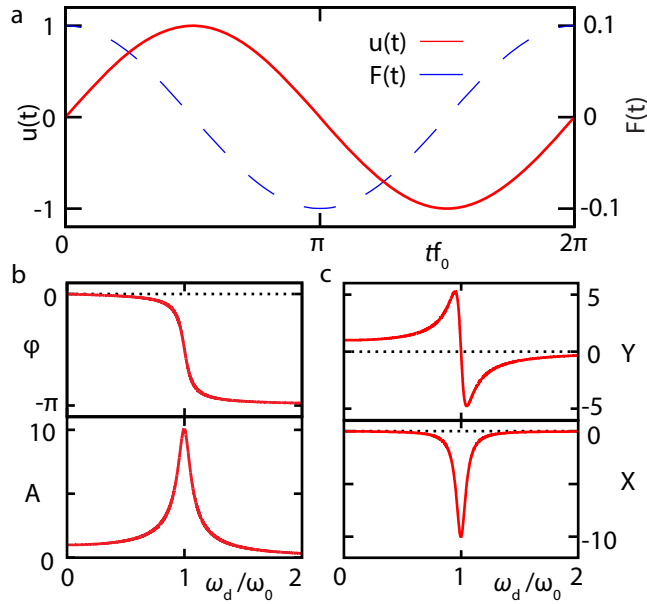


FIGURE 6.5: **Time and spectral response of a linear resonator with $Q = 10$.** **a** shows the displacement of the resonator $u(t)$ (Eq. 6.3) (red line) and a continuous on resonance driving force $F(t) = \cos(\omega_d t)$ (blue line) versus time. **b** The top panel shows the phase (ϕ) and the bottom the magnitude (A) with drive frequency. **c** The top panel shows the real (Y) and the bottom the imaginary (X) part of $H_{HO}(\omega_d)$.

the resonator depends on the drive frequency ω_d . In the top panel of Fig. 6.5b the phase lag of the displacement with respect to the actuation frequency is plotted; The bottom panel shows the amplitude response of the resonator. With changing drive frequency the phase ϕ changes from 0 to $-\pi$ across its resonance position. At resonance the amplitude A has its maximum while the phase lags behind the driving force by $-\pi/2$.

Switching the drive off

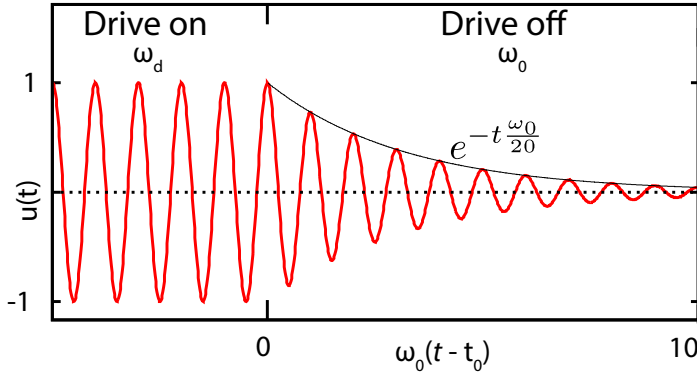


FIGURE 6.6: **Ring down of the displacement of a linear resonator with $\phi = 0$.** The resonator is continuously driven at resonance until a point in time $t = t_0$ at which the driving is switched off. From that time onwards the amplitude of the resonator decays while it is still resonating at its own fundamental resonance frequency ω_0 .

In this section we will consider an harmonic oscillator that is driven by a constant driving force $F(t) = F_0 \cos(\omega_d t)$ for $t < 0$ and undergoes free evolution with $F = 0$ for $t > 0$. For $t < 0$ $u(t)$ is given by equation 6.3. For $t > 0$, using the equation of motion (Eq. 6.1) with $F = 0$ and assuming $Q > 1$, $u(t)$ is given by the following equation;

$$u(t) = [X_0 \cos(\omega_0 t) + Y_0 \sin(\omega_0 t)] e^{-\frac{t}{2\tau}}. \quad (6.4)$$

The constants X_0 and Y_0 are determined by matching the position u and velocity \dot{u} of the two solutions at $t = 0$, giving $X_0 = X_d$ and $Y_0 = Y_d \frac{\omega_d}{\omega_0}$. Figure 6.6 shows the displacement evolution $u(t)$ of a linear resonator with time. The resonator is driven with a resonant driving force in (Fig.6.6a), and then switched off at $t = t_0$. It is interesting to note that for $t > 0$ the displacement of the resonator $u(t)$ oscillates at its natural frequency ω_0 independent of the initial driving frequency ω_d . Fig. 6.6 shows the ring down a resonator driven driven at $\omega_d = \omega_0$ for $t < 0$. In this example, the decay time $\tau = 10/\omega_0$ and $Q = \tau\omega_0 = 10$. For $t < 0$ $u(t)$ oscillates with constant amplitude and for $t > 0$ the amplitude of the oscillations decay with a time constant $\tau = Q/\omega_0$. To summarise, the equations describing the mechanical motion of the resonator at any given drive frequency can be written as:

$$u(t) = \begin{cases} t \leq 0 & , X(t) \cos(\omega_d t) + Y(t) \sin(\omega_d t) \\ t > 0 & , X(t) \cos(\omega_0 t) + Y(t) \sin(\omega_0 t) \end{cases} \quad (6.5)$$

, where $X(t)$ and $Y(t)$ are given by:

$$X(t) = \begin{cases} t \leq 0, & X_d, \\ t > 0, & X_d \cdot e^{-\frac{t}{2\tau}}, \end{cases}$$

$$Y(t) = \begin{cases} t \leq 0, & Y_d \\ t > 0, & Y_d \frac{\omega_d}{\omega_0} \cdot e^{-\frac{t}{2\tau}} \end{cases}$$

6.5.3 SIGNAL FROM THE CNT

To measure the mechanical response of the carbon nanotube, we use a variant of a two source mixing technique. In this technique, we apply two RF signals to the gate electrode at frequency ω_d and ω_p . The signal at ω_d is used to drive the mechanical resonator and the signal at ω_p is used to probe the mechanical response. The signal ω_p is detuned from ω_d by an amount $\omega_{ref} = \omega_p - \omega_d$. We have chosen $\omega_{ref} \sim 2\pi \times 7$ MHz, which is much larger than the mechanical line width. Therefore the CNT will not be driven by the probe signal at ω_p .

We will now consider the transduction of the mechanical motion, given by eq. 6.5, into a signal that is detected in the experiment. The total electrostatic voltage δV_G^e is given by:

$$\delta V_G^e = \begin{cases} t \leq 0, & V_G^{ac,d} \cos(\omega_d t) + V_G^{ac,p} \cos(\omega_p t) \\ t > 0, & V_G^{ac,p} \cos(\omega_p t) \end{cases} \quad (6.6)$$

where $V_G^{ac,d}$ and $V_G^{ac,p}$ are the amplitude of the drive and probe signals, respectively. The effect of the mechanical motion can be captured by considering an effective oscillating gate voltage given by:

$$\delta V_G^m = \frac{V_G}{C_G} \frac{dC_G}{du} \cdot u(t), \quad (6.7)$$

where C_G is the CNT-gate capacitance. It is important to note that δV_G^m has a frequency of ω_d for $t \leq 0$, and ω_0 for $t > 0$. To analyse the electrical signals generated by the carbon nanotube we can treat it as a normal electrical mixing experiment which now includes an oscillating gate voltage:

$$\delta V_G = \delta V_G^e + \delta V_G^m. \quad (6.8)$$

The displacement of the CNT is represented by $u(t)$. We assume that the CNT is a linear resonator. The displacement $u(t)$ is then given by eq. 6.5.

Now we will consider a generic case when the current through the nanotube is an arbitrary function of the gate voltage V_G : $I = I(V_G)$. We include two effects of the AC gate voltage by doing a Taylor expansion of the current through the CNT: The first three terms of the Taylor expansion of the current are:

$$I(\delta V_G) = I_0 + \frac{dI}{dV_G} \delta V_G + \frac{1}{2} \frac{d^2 I}{dV_G^2} (\delta V_G)^2 \quad (6.9)$$

,where I_0 is a dc current. We now need to consider what will be measured by the lock-in amplifier. The lock-in measures only components of the signal that are within the lock-in measurement bandwidth ($\frac{1}{\tau_L}$) around the reference frequency (ω_{ref}) as illustrated in figure 6.7.

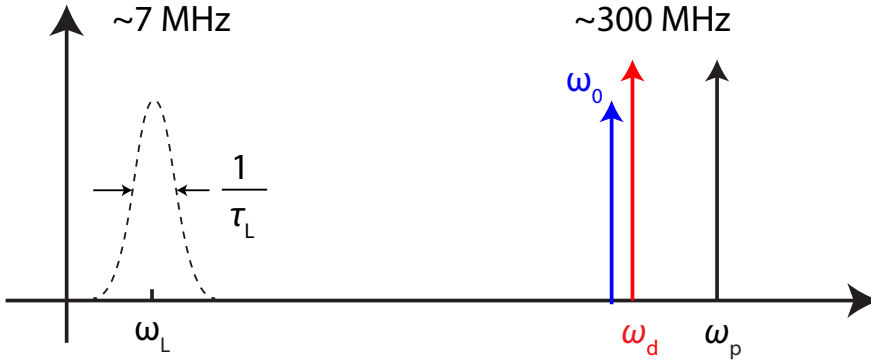


FIGURE 6.7: Frequency analysis of the lock-in measurement scheme.

The lock-in is not sensitive to DC currents, therefore we can neglect the first term. Also, since $\omega_0, \omega_d, \omega_p \gg \omega_{ref} = \omega_p - \omega_d$, the first two terms in equation 6.9 will not give any signals, that will be detected in the experiment. The third term will include products of cosines and sines and therefore can include mixed down signals detected by the lock-in. By substituting Eq. 6.8 into the third term, we get:

$$\Delta I = \frac{1}{2} \frac{d^2 I}{dV_G^2} [(\Delta V_G^e)^2 + 2\delta V_G^m \delta V_G^e + (\delta V_G^m)^2] \quad (6.10)$$

Here we can see two contributions that will give a signal near to ω_l : the first is from $(\delta V_G^e)^2$ term, which will give an electrical background from the electrical mixing of the probe and drive voltages. The third term $(\delta V_G^m)^2$ will not contribute to the lock-in signal as it only contains DC and $\sim 2\omega_0$ frequencies.¹ The middle term

¹This is the term used for previous DC rectification experiments.

$2\delta V_G^m \delta V_G^e$ gives us an AC current. To summarise the current that will be measured by the lock-in we get:

$$\Delta I_L = \frac{1}{2} \frac{d^2 I}{dV_G^2} \begin{cases} t \leq 0, & (\Delta V_G^e)^2 + 2\delta V_G^m \delta V_G^e \\ t > 0, & 2\delta V_G^m \delta V_G^e \end{cases} \quad (6.11)$$

6.5.4 INPUT SIGNAL AT THE LOCK-IN

In the following we will first consider a signal without any electrical background $(\Delta V_G^e)^2$, which is present when the resonator is driven. For a time ($t > 0$) the lock-in measures a signal ΔI_L^{mech} which comes from the mechanical motion of the carbon nanotube:

$$\Delta I_L^{mech} = \frac{1}{2} \frac{d^2 I}{dV_G^2} 2\delta V_G^m \delta V_G^e \quad (6.12)$$

$$\delta V_G^e = V_G^{ac,p} \cos(\omega_p t) \quad (6.13)$$

$$\delta V_G^m = \alpha \cdot u(t) \quad (6.14)$$

$$\alpha = \frac{V_G}{C_G} \frac{dC_G}{du} \quad (6.15)$$

, where α is a factor which translates the displacement of the carbon nanotube into a voltage. The lock-in signal becomes:

$$\Delta I_L^{mech} = \frac{d^2 I}{dV_G^2} \alpha [X(t) \cos(\omega_0 t) + Y(t) \sin(\omega_0 t)] \cdot V_G^{ac,p} \cos(\omega_p t) \quad (6.16)$$

By expanding the products $\cos(\omega_0 t) \cos(\omega_p t)$ and $\sin(\omega_0 t) \cos(\omega_p t)$, and discarding the frequencies at $\omega_0 + \omega_p$, the signal at $\Delta\omega = \omega_p - \omega_0$ becomes:

$$\Delta I_L^{mech} = \frac{d^2 I}{dV_G^2} V_G^{ac,p} \alpha [X(t) \cos(\Delta\omega t) + Y(t) \sin(\Delta\omega t)] \quad (6.17)$$

This signal is at frequency $\Delta\omega$ and is read out at the lock-in with respect to the reference signal $\omega_{ref} = \omega_p - \omega_d$.

Quadrature signals from the lockin

Remaining high frequency components are filtered at the lockin ² such that $\Delta\omega$ remains. Then the two outputs of the lock-in are the following:

$$X_L^{mech} = \frac{d^2 I}{dV_G^2} V_G^{ac,p} \alpha [X(t) \cos(\omega_{beat} t) + Y(t) \sin(\omega_{beat} t)] \quad (6.18)$$

$$Y_L^{mech} = \frac{d^2 I}{dV_G^2} V_G^{ac,p} \alpha [X(t) \sin(\omega_{beat} t) + Y(t) \cos(\omega_{beat} t)], \quad (6.19)$$

where $\omega_0 - \omega_d = \omega_{beat}$. For the case of $\omega_d = \omega_0$, ($\cos(\omega_{beat} t) = 1$), the quadrature outputs of the lockin directly represents the time dependent amplitudes $X(t)$ and $Y(t)$ of the mechanical motion.

When the resonator is driven ($t > 0$), for a linear resonator, the resonance frequency is the same as the drive frequency $\omega_0 = \omega_d$. For our mechanical resonator the lock-in X and Y quadratures (without any electrical mixing $(\Delta V_G^e)^2$), the outputs simplify to:

$$X_{Ld}^{mech} = \frac{d^2 I}{dV_G^2} V_G^{ac,p} \alpha X_d \quad (6.20)$$

$$Y_{Ld}^{mech} = \frac{d^2 I}{dV_G^2} V_G^{ac,p} \alpha Y_d \quad (6.21)$$

When the driving signal is switched off ($t > 0$), ω_d is not always equal to ω_0 , The X and Y quadrature outputs of the lock-in become:

$$X_{Lr}^{mech} = \frac{d^2 I}{dV_G^2} V_G^{ac,p} \alpha \left[X_d \cos(\omega_{beat} t) + Y_d \frac{\omega_d}{\omega_0} \sin(\omega_{beat} t) \right] e^{-\frac{t}{2\tau}} \quad (6.22)$$

$$Y_{Lr}^{mech} = \frac{d^2 I}{dV_G^2} V_G^{ac,p} \alpha \left[X_d \sin(\omega_{beat} t) + Y_d \frac{\omega_d}{\omega_0} \cos(\omega_{beat} t) \right] e^{-\frac{t}{2\tau}} \quad (6.23)$$

, X_{Lr}^{mech} and Y_{Lr}^{mech} are valid for any time t after the driving signal is switched off.

Now we consider the signal contribution by the electrical background which is present when the the resonator is driven. The effect of the electrical background is

²See lock-in user manual of SR830 [3] and of HF2LI Lock-in Amplifier (Zurich Instruments, Zurich, Switzerland).

a constant offset in the signal, when the resonator is being driven:

$$\Delta I_L^{elec} = \frac{1}{2} \frac{d^2 I}{dV_G^2} V_G^{ac,p} V_G^{ac,d} \cos(\omega_{ref} t) \quad (6.24)$$

$$X_L^{elec} = \frac{d^2 I}{dV_G^2} \frac{1}{2} V_G^{ac,p} V_G^{ac,d} \quad (6.25)$$

$$Y_L^{elec} = \frac{d^2 I}{dV_G^2} \frac{1}{2} V_G^{ac,p} V_G^{ac,d} \quad (6.26)$$

We summarise the equations describing the output of the lock-in amplifier, including the electrical background:

$$X_L = \begin{cases} t \leq 0, & X_{Ld}^{mech} + X_L^{elec} \\ t > 0, & X_{Lr}^{mech} \end{cases} \quad (6.27)$$

$$Y_L = \begin{cases} t \leq 0, & Y_{Ld}^{mech} + Y_L^{elec} \\ t > 0, & Y_{Lr}^{mech} \end{cases} \quad (6.28)$$

which is:

$$X_L = \begin{cases} t \leq 0, & \beta \cdot X_d + X_L^{elec} \\ t > 0, & \beta \cdot \left[X_d \cos(\omega_{beat} t) + Y_d \frac{\omega_d}{\omega_0} \sin(\omega_{beat} t) \right] e^{-\frac{t}{2\tau}} \end{cases} \quad (6.29)$$

$$Y_L = \begin{cases} t \leq 0, & \beta \cdot Y_d + Y_L^{elec} \\ t > 0, & \beta \cdot \left[X_d \sin(\omega_{beat} t) + Y_d \frac{\omega_d}{\omega_0} \cos(\omega_{beat} t) \right] e^{-\frac{t}{2\tau}} \end{cases} \quad (6.30)$$

$$\beta = \frac{d^2 I}{dV_G^2} V_G^{ac,p} \alpha \quad (6.31)$$

, where X_L^{elec} and Y_L^{elec} are constant voltage offsets independent of time and drive frequency.

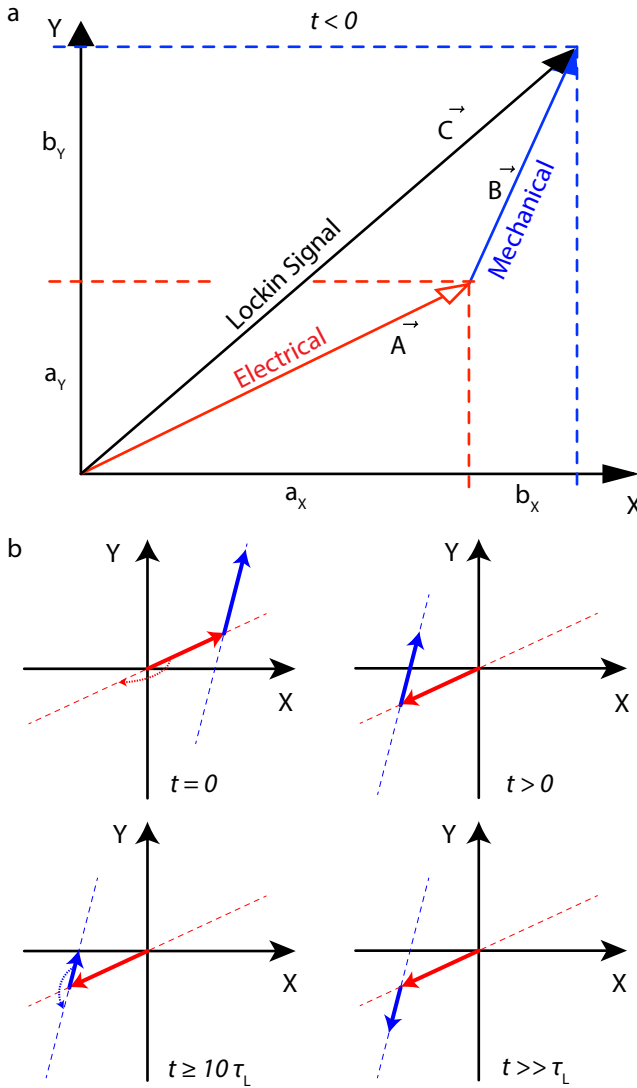


FIGURE 6.8: **Vector diagram of the mechanical and electrical signal composition**, The detected signal at the lock-in amplifier is represented as a vector \vec{C} . The signal vector \vec{C} is separated into two vectors one, \vec{A} representing the electrical signal and \vec{B} representing the mechanical signal.

Figure 6.8a illustrates the two recorded quadratures of the lock-in amplifier

while driven on resonance. X_L^{elec} and Y_L^{elec} describe the electrical mixing of the probe and drive signal at the CNT. This is an electrical background signal which is independent of the motion of the CNT, (red arrow in Fig. 6.8a). X_L^{mech} and Y_L^{mech} describe the mixing of the mechanical motion with the probe signal. The amplitude of the signal is proportional to $(|H_{HO}(\omega)|)$, which is frequency dependent and has its maximum at resonance ($\omega = \omega_0$). As soon as the drive signal is switched off, X_L^{elec} and Y_L^{elec} decay over time with the lock-in time constant (Γ_{Lockin}). If the lock-in time constant is smaller than the mechanical time constant $\tau_L < \tau$ the mechanical signal remains such that X_L^{mech} and Y_L^{mech} is detected. From equation (Eq. 6.4), we see that the amplitude of this signal decays with $e^{-\frac{t}{2\tau}}$ in time.

Figure 6.8b is a smaller version of (Fig.6.8a) for ($t < 0$), it shows four different stages in time. At a time $t = 0$ the drive is switched off; both the electrical (red arrow) and the mechanical signal (blue arrow) are present. The black dotted lines indicate the angle of the vectors. As time progresses $0 < t < \tau_L$, the electrical signal (red) decays at a much faster rate than the mechanical signal (blue). For $t \geq 10 \cdot \tau_L$ the electrical signal does not change any further with time. From now on the mechanical ring down of the CNT is recorded by the Y quadrature of the lock-in. At a time $t \gg 10\tau$, the mechanical signal settles. Finally both arrows, for the mechanical and the electrical components are inverted. We think that this inversion is due to common mode noise, see Section 6.5.9.

6.5.5 SPECTRAL MEASUREMENTS

We first turn to the driven motion, Fig. 6.10a we plot the X and Y quadratures of the lock-in as a function of drive frequency f . The gate voltage is fixed at 0.4 V. The plot is obtained by slowly stepping the drive (and probe) signal across the mechanical resonance of the CNT, while recording the X and Y quadratures of the lock-in output signal. The data can be fitted to the following equation:

$$f_{sp}(\omega) = a|H_{HO}(\omega)|e^{i\phi} + (b + c\omega)e^{i\theta} , \quad (6.32)$$

where ϕ is the phase from the mechanical and θ from the electrical signal. The real and imaginary parts of $f_{sp}(\omega)$ are fitted to the X and Y quadratures respectively. The spectral quality factor, resonance position and phase are obtained from this fit.

Phase rotation of the data

For analysis the data, it is important that the phase offset between reference and input signal is discounted for. This can be done by introducing a rotation matrix:

$$\begin{aligned} X1 &= X \cos(\phi) - Y \sin(\phi) , \\ Y1 &= X \sin(\phi) + Y \cos(\phi) , \end{aligned} \quad (6.33)$$

where X_1 and Y_1 are the new quadratures and ϕ is the phase by which the two recorded X and Y quadratures are rotated by. In Fig. 6.9 the (adjusted) quadratures are shown for four different phase offsets. The phase is rotated from $\phi = -\pi$ to $\phi = \pi/2$ showing how the X quadrature changes. When $\phi = 0$ the response is similar to the one of Fig. 6.5c (X), which represents the linear response of a mechanical resonator. The corresponding Y quadrature (exactly the same as the one shown for $\phi = -\pi/2$) looks similar to (Y) in Fig. 6.5c.

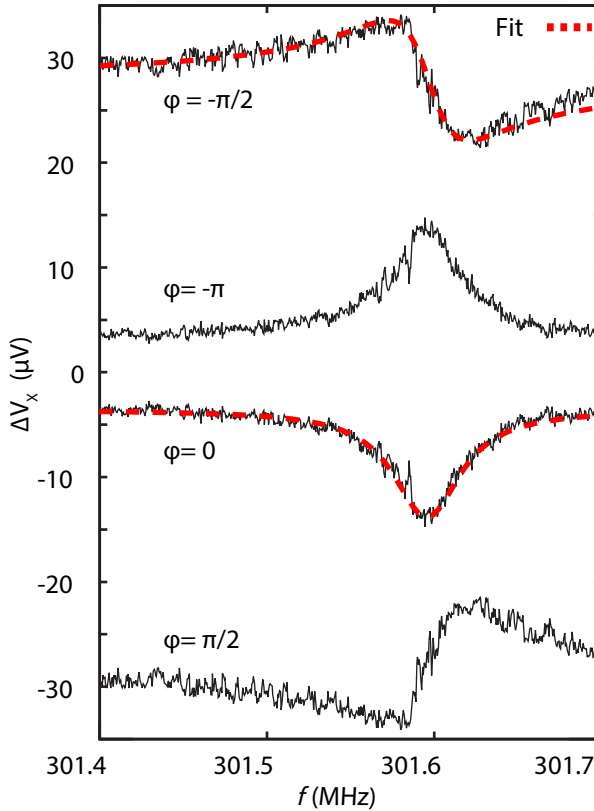


FIGURE 6.9: **Signal line shape as a function of phase rotation** (Eqn. 6.33). The signal was recorded at a fixed gate voltage $V_G = 0.4$ V and a fixed bias voltage $V_B = -0.5$ mV. The dashed red curve is a Lorentzian fit to the data yielding $Q_S = 6192$.

We have taken this as the X quadrature which presents the amplitude of the carbon nanotube motion. For all measurements we have performed this rotation

matrix procedure to correct the phase offset between reference and input signals. It is important to work with the X and Y quadratures to avoid complications in the subtraction of the offset signal. The convenience of working with quadratures is that you can always rotate the phase to get a lorentzian like quadratures, as long as the response is linear, in contrast to working with amplitude and phase, at which any additional offset in the background results in an asymmetric Fano line shape.

From the two curves which are rotated to $\phi = 0$ and $\phi = -\pi/2$ (Fig. 6.9) we can determine the resonance frequency and quality factor by fitting the response to $f_{sp}(\omega)$. The fit is shown as a red dashed line through the data. We find $f_{res} = 301.596$ and $Q_S = 6192$. This Q_S is what we call the spectral Q factor of the resonator.

6.5.6 RINGDOWN MEASUREMENTS

To obtain the response while being on resonance, the following procedure was used: Repeating switch pulses are applied to the switch (see circuit Fig. 1 of the main text) turning the drive signal on and off. At the same time the quadratures of the lock-in amplifier are measured by an oscilloscope. The oscilloscope is triggered by the same pulse which drives the switch. Which is also used to average the quadrature components (typically 10000 times).

Fig 6.10 shows the result for the rotated X quadrature for two cases: the lower curve shows the response for which the resonator was off-resonance ($f = 301.4$ MHz), whereas the upper curve shows the response for which the resonator was actuated on-resonance ($f = 301.596$ MHz). Both curves have been offset in the y-direction such that they approach zero with time. The off-resonance curve $f = 301.4$ MHz shows the lock-in related ring down of the electrical background, independent of the mechanical resonance

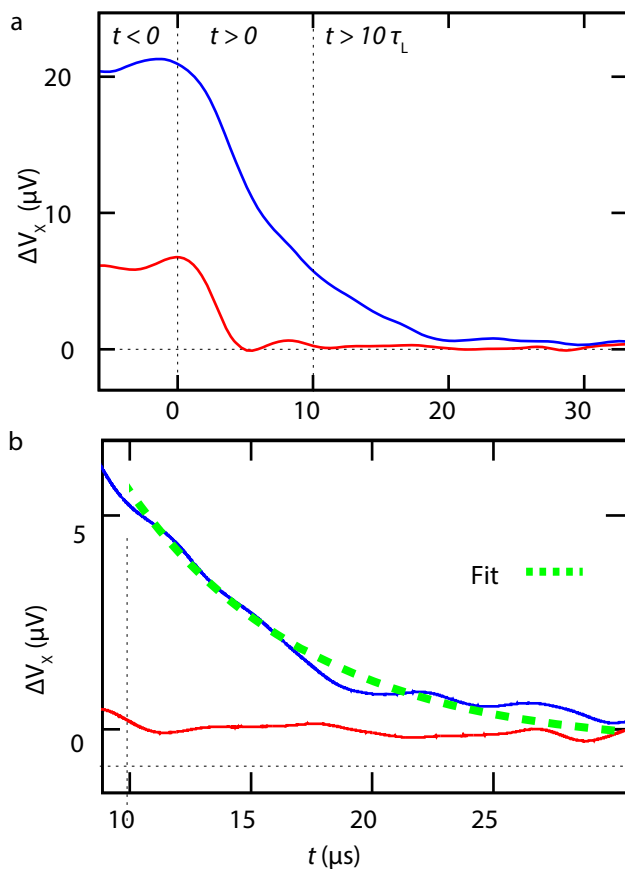


FIGURE 6.10: **Mechanical ring down of the carbon nanotube resonator. a,b** Measured response of the rotated quadrature versus time. The gate voltage is fixed at $V_G = 0.4$ V, and the phase has been rotated to ($\phi = 0$) such that ΔV_X represents the amplitude. For the blue curve the drive signal is tuned to the mechanical resonance ($\omega_d = \omega_0 = 301.596$ MHz). For the red curve the drive signal is far detuned from resonance ($\omega_d \neq \omega_0 = 301.4$ MHz). The detuning is large enough such that the red curve dominantly represents the electrical mixing signal. At $t = 0$ the drive signal is switched off (dashed line). The lock-in time constant is 900 ns. **b** Zoomed section, the dashed green line through the data represent an exponential fit (Eqn. 6.34) which yields $\tau = 3.44\mu\text{s}$ and $Q_R = 6513$. The fit was extracted from $t > 10\mu\text{s}$.

Region selection for fitting

Indicated by dashed lines in Fig. 6.10, we identify three distinct times; at $t < 0$ during which the resonator is driven, $t > 0$ the time required for X_L^{elec} and Y_L^{elec} to decay into a constant offset and $t > 10\tau_L$ during which the mechanical signal decays. In order to avoid effects from the finite constant of the lock-in; We discard times $t < 10\tau_L$. This also discards the first part of the mechanical ring down, which also contains the ring down of the electrical mixing signal (which is present because of the time constant of the lock-in filter). For more than $10 \mu\text{s}$ after switching off the drive signal, effects from the lock-in filter (with a time constant of 900 ns) are found to be negligible. After this time ($t > 10 \mu\text{s}$), we extract the ring down Quality factor.

Fitting the ringdown Q factor

Clearly the upper curve shows the exponential decay associated with the mechanical ring down of the resonator. To extract the ring down quality factor (Q_R) the data was fitted to:

$$A(t) = A_0 e^{-(t)/(2T_1)} + B \quad (6.34)$$

where $T_1 = \frac{Q_R}{2\pi f_0}$, A_0 and B are fitting constants. The quality factor at the mechanical resonance yields $Q_R = 6513$. The uncertainty for all data shown here using this fit were found to be within 10%.

6.5.7 MODEL FOR RINGDOWN

The fitting method described in the previous subsection 6.5.6 is good to obtain a ringdown Q_R factor for multiply averaged quadrature and amplitude data with a small amounts of dephasing and negligible electrical offsets. Electrical offsets can be accounted for by measuring and averaging both quadratures components. However, large amounts of dephasing become a problem if one averages the quadrature outputs of the lockin which oscillates in time (see eq. 6.29 and 6.30). This oscillation occurs because the frequencies of the reference and the mechanical response do not match, which can happen when the resonator changes its original resonance frequency position to a different one, due to dephasing. We can assume that the dephasing (a change in resonance position) happens at a frequencies less then the time required for the resonator to ring down. Knowing this, allows us to model an averaged ringdown response, including dephasing, which we can fit to the measured data. Additionally we can convolve the simulated data with the exact same measured lockin response function, allowing us to fit the the simulated data to the full ringdown time, including times less than 10 times the lockin time constant.

Modelling of quadrature data

We consider the signals for the X and Y quadrature components which exit the lockin, before they are averaged by the oscilloscope and we only consider a signal originating from the mechanical response of the resonator without any noise. For now, we also ignore effects due to the lockin time constant. For times where the resonator is driven the amplitude response for a given frequency is constant. Specifically the real and imaginary component of equation 6.2 are proportional to the X and Y quadrature magnitudes (which are then measured by the oscilloscope).

$$H_{HO}(\omega) = k_R \frac{u(\omega)}{F(\omega)} = \frac{\omega_0^2}{\omega_0^2 - \omega^2 + i\omega\omega_0/Q} \quad (6.35)$$

From the measured data we can fit the spectral Q_S and resonance frequency of the resonator using eqn. 6.32. By inserting the fitted results for the spectral Q_S and resonance frequency ω_0 into eq. 6.35, we can calculate the real ($X_d(\omega_d)$) an imaginary ($Y_d(\omega_d)$) results as a function of drive frequency. These results for $X_d(\omega_d)$ and $Y_d(\omega_d)$ are are proportional to these X and Y quadratures, for times when the driving is activated:

$$X_{Ld}^{mech} \propto X_d(\omega_d) \quad (6.36)$$

$$Y_{Ld}^{mech} \propto Y_d(\omega_d) \quad (6.37)$$

Let us define the time $t = 0$ where we switch the driving frequency off. Such that for times $t < 0$ the X and Y quadratures are simply given by eq. 6.36 and 6.37, respectively. For times $t > 0$, driving is switched off. During this regime the two important effects happen to the mechanical signal; First the amplitude decays with time given by the ringdown Q_R factor. Second for off resonance driving frequencies, the resonators response frequency will be at ω_0 instead of at ω_d , which results in an oscillation of the X and Y quadrature signals. By using the same method as before by using $X_d(\omega_d)$ and $Y_d(\omega_d)$ the equations 6.29 and 6.30 derived in section 6.5.2 now become:

$$X_{Lr}^{mech} \propto \left(X_d(\omega_d) \cos(\Delta\omega_{0d}t) + Y_d(\omega_d) \frac{\omega}{\omega_0} \sin(\Delta\omega_{0d}t) \right) e^{-\frac{\omega t}{2Q}} \quad (6.38)$$

$$Y_{Lr}^{mech} \propto \left(X_d(\omega_d) \sin(\Delta\omega_{0d}t) + Y_d(\omega_d) \frac{\omega}{\omega_0} \cos(\Delta\omega_{0d}t) \right) e^{-\frac{\omega t}{2Q}} \quad (6.39)$$

, where $e^{-\frac{\omega t}{2Q}} = e^{-\frac{t}{2\tau}}$. By using these four equations we can obtain a numerical result of an amplitude which is proportional to the X and Y quadrature output of the lockin (assuming the lockin time-constant is equal to zero). , for any point in time and drive frequency ω_d . For times $t < 0$ equations 6.36 and 6.37 are used to obtain values proportional to the X and Y quadratures, respectively. For times $t \geq 0$ equations 6.38 and 6.39 are used.

Modelling of dephasing and averaged quadrature data

We model the dephasing and averaging of the oscilloscope by using the method described above. For the dephasing we assume a lorentzian distribution, (same line-shape as the resonator). The procedure is as following: From the spectral fit of the measured data, we obtain the resonance frequency and spectral Q_S factor. Using this resonance frequency and choosing a ringdown Q_R factor we can calculate a quadrature response map as a function of drive frequency and time. The spectral Quality factor of this map will be equal to Q_R . To get a Spectral quality factor which matches the fitted Q_S , we add dephasing to it by convolving this map with a lorentzian distribution along the frequency axis with a dephasing quality Q_D factor constrained by the following equation:

$$Q_D = \frac{1}{Q_S^{-1} - Q_R^{-1}} \quad (6.40)$$

, where Q_S is the fitted spectral quality factor from the measured data and Q_R is now a variable which can be changed or fitted for. The spectral quality factor of the resulting matrix is equal to the fitted spectral Q_S .

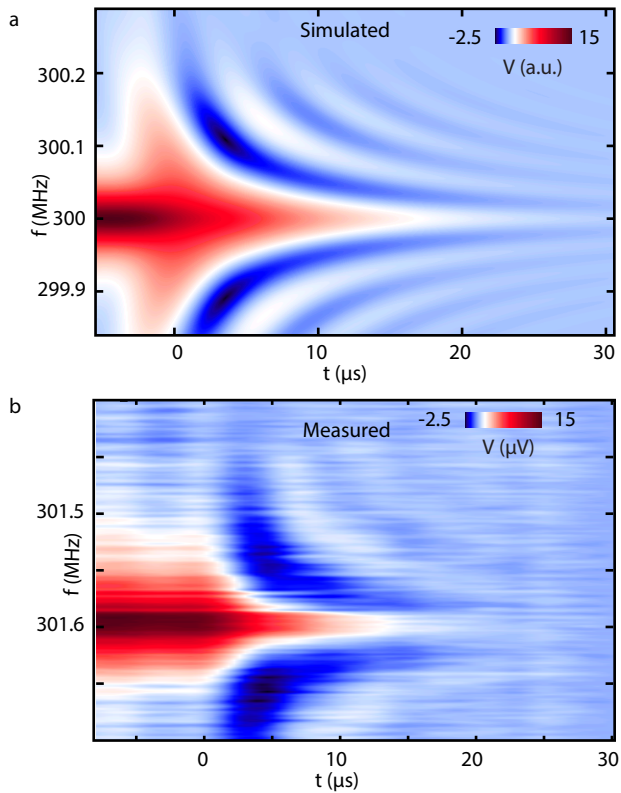


FIGURE 6.11: **a** Simulated data set **b** Measured data set (see Fig.6.3)

Extracting the locking time constant

To complete the simulated data set we add the effects due to the lockin time constant. The time constant defines the shape of the filter function of the lockin in the time domain. First we need to obtain the exact filter-function, which was used by the lockin. To obtain the filter function, we generate a step function signal which is mixed by a reference signal from the lockin amplifier. This signal is then fed into the input of the lockin and the two quadratures X and Y from the lockin output are recorded by the oscilloscope, alongside the step function. By taking the derivative of the output step function recorded by the oscilloscope, we obtain our filter function. To verify that this filter function is correct, we convolve the recorded step function and see if the shape of the signal matches that of the measured signal. (Al-

ternatively we can also deconvolve the recorded step function and compare that to the input signal). Once the correct filter functions are obtained, we convolve the simulated data set with it along the time axis. Figure 6.11 shows such a simulated data set.

Fitting Q_R using the modelled data

In order to fit the ringdown Q_R factor. The previous steps have been repeated for different ringdown quality and dephasing factors, while comparing the time domain at the resonance positions. By extracting a linecut at resonance from the simulated and the measured data set, we can subtract both from each other and minimise χ^2 as a function of Q_R . Figure 6.12 shows such a plot, which was recorded to obtain a rough estimate in fitting error.

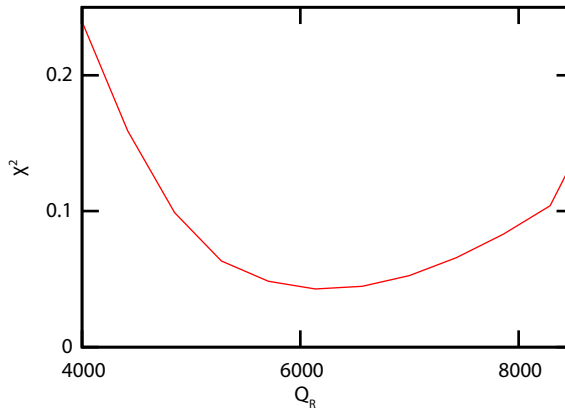


FIGURE 6.12: χ^2 as a function of Q_R This is the fitting result for the data set presented in the main text Fig. 6.4a. The spectral $Q_S=1407$, the fitted ringdown is found to be around $Q_R \sim 6140$.

A python code doing this, is available on Github here:

https://github.com/benschneider/dephasing_ringdown_sim

6.5.8 GATE DEPENDENT MEASUREMENTS

Figure 6.13 shows the electronic and mechanical DC response of the region.

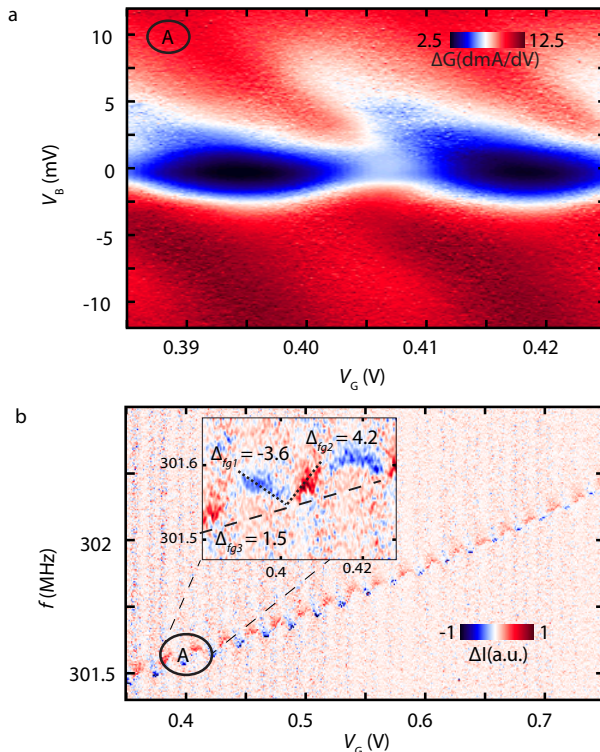


FIGURE 6.13: **Two high detailed colour-scale maps, showing electronic and mechanical response of the CNT in region A:** **a**, Colour-scale-map of the measured differential conductance as a function of V_G and V_B . Area A goes across two coulomb peaks, this measurement was taken at a temperature of 2 Kelvin. **b**, Measured change in rectification current (colour) as a function of gate and drive frequency. The inset is a magnification of region A, taken by a second measurement. Dashed lines and the values $\Delta_{fg1} = -3.6 \frac{\text{MHz}}{\text{V}}$, $\Delta_{fg2} = 4.2 \frac{\text{MHz}}{\text{V}}$ and $\Delta_{fg3} = 1.5 \frac{\text{MHz}}{\text{V}}$ indicate the slopes of the frequency change as a function of V_G .

6.5.9 RESIDUAL DRIVING WHEN THE SWITCH IS OFF

When turning the switching off, we find that there still is a small residual AC voltage on the gate driving the resonator with a signal, that appears to be 180° phase shifted. We think, that this arises from insufficient AC grounding in the setup, resulting in a common-mode signal. In figure 6.14, we explain the effect of the resid-

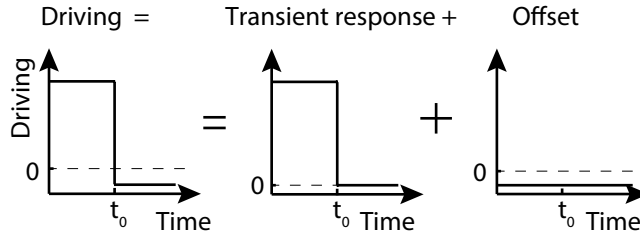


FIGURE 6.14: **Schematics showing the decomposition of the driving amplitude in the presence of a residual driving signal.** From Left to Right: In the presence of a residual driving signal with a 180° phase shift, the signal drops to a negative offset, after turning the switch off. This can be decomposed into two components: One is the transient regime, that when the driving is switched off it drops to zero. The other component is a constant negative offset. For a linear resonator the displacement $u(t)$ is then also a linear combination of both effects:

ual driving on the dynamic response. For a linear response, this results in a constant background signal, when the switch is off.

For a linear resonator the displacement $u(t)$ is then also a linear combination of both effects. The motion of the resonator for $t > 0$ becomes:

$$u(t) = A \cos(\omega_0 t) + B_2 \sin(\omega_0 t) e^{-\frac{t}{2\tau}} - C(A \cos(\omega t) + B \sin(\omega t)) \quad (6.41)$$

where C is a constant. As a result of this the lock-in returns a signal containing an offset.

REFERENCES

- [1] B. H. Schneider, S. Etaki, H. S. J. van der Zant, and G. A. Steele, *Coupling carbon nanotube mechanics to a superconducting circuit*, Sci. Rep. **2** (2012).
- [2] M. Poot and H. S. J. van der Zant, *Mechanical systems in the quantum regime*, Physics Reports **511**, 273 (2012).
- [3] M. SR830, *from Stanford Research Systems, Inc.(USA)* (2011).

7

SPECTROSCOPY OF CARBON NANOTUBE SUPERCONDUCTING JUNCTIONS

As grown carbon nanotubes, suspended between molybdenum rhenium contacts, can form a Josephson junction which can carry a supercurrent of 15 nA. This high critical current allows us to investigate in detail spectroscopic features, related to superconducting effects. We report on electronic spectroscopy measurements of carbon nanotube Josephson junctions. The devices have the same geometry and are made in the same way as those described in chapter 4. From characterisations at room and low temperatures, we identify as-grown carbon nanotube Josephson junctions. We find a supercurrent in the Coulomb blockade and in the Fabry-Pérot regime. In the Fabry-Pérot regime, we observe features which suggest the presence of phase averaged Andreev bound states. And in the Coulomb blockade regime, we observe negative differential conductance.

During our measurements with carbon nanotube Josephson junction devices, we came across a range of different phenomena, seen in the current voltage (IV) measurements. Here we present a brief overview of some of these phenomena. The electronic spectroscopy measurements are done in two ways: One is by measuring a current passing through the device while applying a bias and gate voltage, and the second one is by measuring a voltage while applying a current across the device and changing the gate voltage.

7.1 BASIC CHARACTERISATION OF THE DEVICES

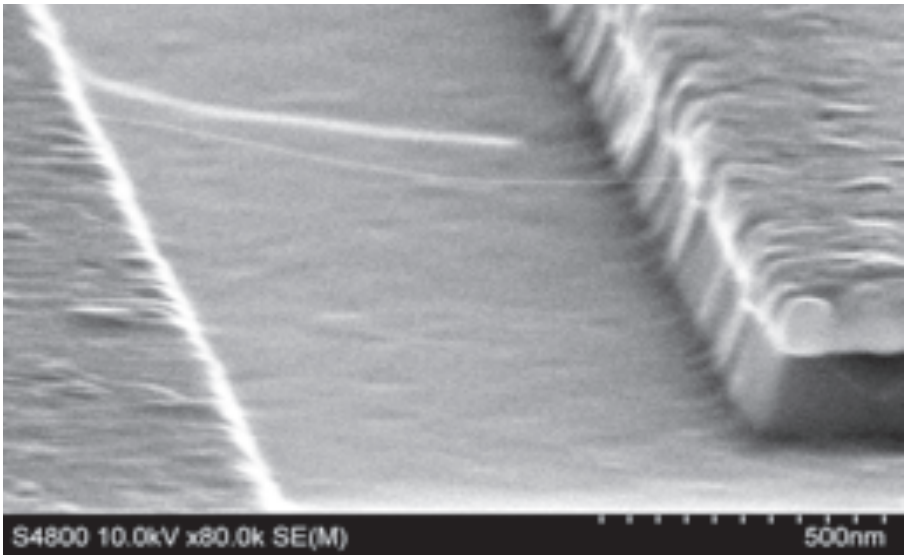


FIGURE 7.1: Scanning electron microscope image a CNT grown across a 800 nm wide and 250 nm deep MoRe trench.

The devices consist of a suspended CNT with superconducting contact leads and a back-gate which is ~ 285 nm located underneath the suspended nanotube segment (Fig. 7.1). The superconducting contact leads are made of an Molybdenum-Rhenium (Mo-Re) alloy (each 40 nm thick). Fabrication of these devices is described in detail in chapter 3. After fabrication, the devices are initially characterised at room temperature (RT) and selected devices are cooled down at cryogenic temperatures (typically 25 mK). Figure 7.2 shows the measured conductance at RT as a function of gate voltage V_G for a fixed bias voltage of 10 mV. A small dip

in the conductance is visible close to a zero gate voltage, which we often found to be a good indication for a clean small band gap CNT.

In this chapter we present measurements of three devices with the exact same geometry and fabrication procedure. The geometry is the same as presented in Ref.[1]; two trenches separate the source from the drain such that a single carbon nanotube can grow and make contact across both trenches. For the purpose of clarification we will indicate in the figures which device and during which cool-down the presented data was measured. Namely the device with 'D1', 'D2' and 'D3' and the cool-down with 'C1', 'C2' and 'C3', such that 'D1C2' indicates that the measured data originated from device 1 during the second cool-down. The measurements presented, were taken without an applied magnetic field.

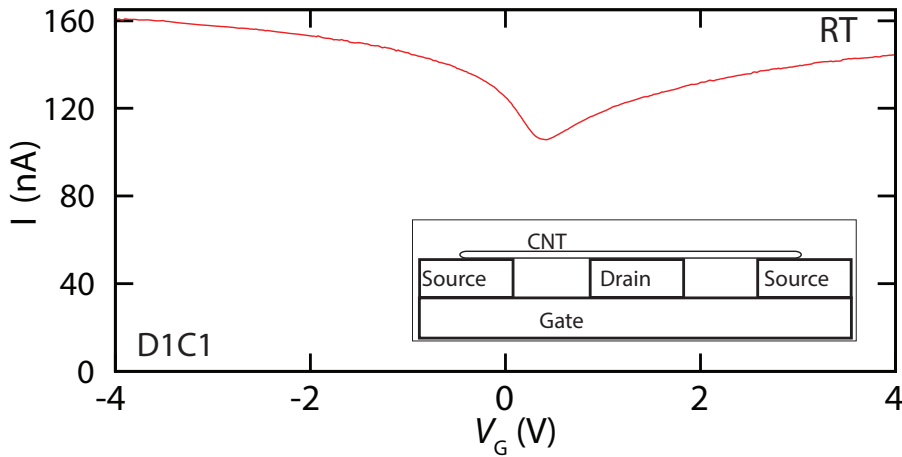


FIGURE 7.2: **Electric spectroscopic characterisation of a double SNS junction at room temperature.** Two-terminal current I as a function of V_G at a source-drain voltage bias $V_B = 10$ mV of device D1C1.

Once wire bonded, the device is cooled down to 25 mK in a dilution fridge. Exactly as for the device described in chapter 4, low-pass and copper-powder filters are used for direct current (DC) connections to the device. Figure 7.3a shows the measured conductance as a function of gate voltage, for a fixed bias voltage of 5 mV. Instead of a small dip at zero gate voltage we can now clearly see a drop in the conductance at $V_G \sim 0.25$ V. For negative gate voltages we have a high conductance with Fabry-Pérot (FP) oscillations. For positive gate voltages ($V_G > 0.25$ V) we see sharp conductance peaks, indicating Coulomb blockade (CB).

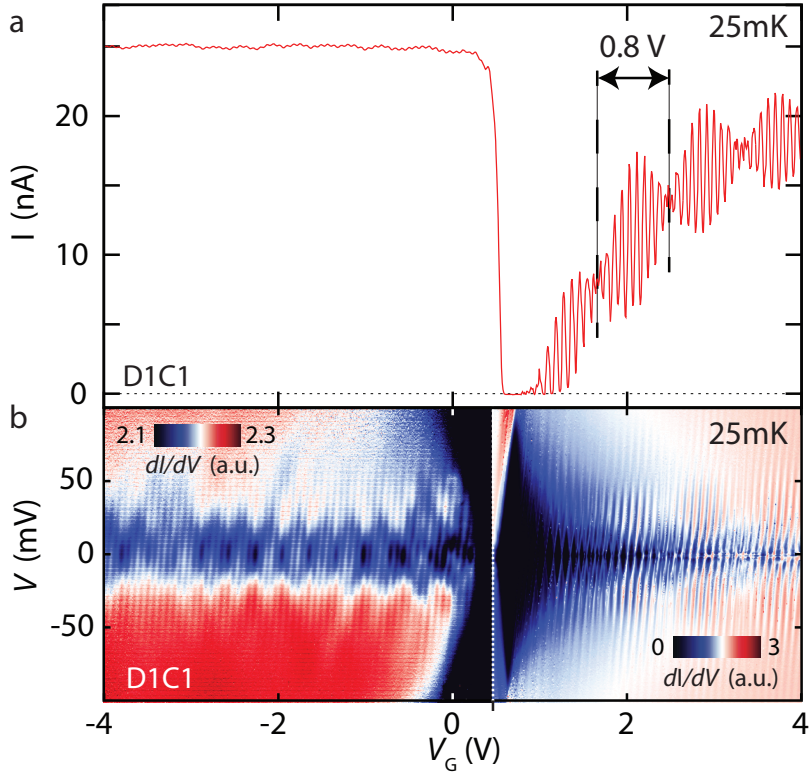


FIGURE 7.3: **Electric spectroscopic characterisation of a double SNS junction at 25 mK.** Two-terminal current I as a function of V_G and source-drain voltage bias (V_B) of device D1C1. **a** Current as a function of V_G at $V_B = 1.52$ mV at 25 mK. For negative V_G , the conductance is high with small oscillations (Fabry-Pérot regime), for positive V_G the conductance is low with large oscillations (Coulomb blockade). The beat periodicity $V_G = 0.8$ V is indicated by two dotted lines. **b** Differential conductance (dI/dV) colour-map as a function of V_G and bias voltage. In order to highlight all features two different colour scales are used, one for the high-conductance region (left side) and one for the low conductance region (right side).

Figure 7.3b is a two colour map of the differential conductance as a function of gate and bias voltage. The left panel highlightst the Fabry-Pérot regime and the right panel the Coulomb blockade regime. So far, all our clean CNT devices with MoRe contacts (which have been cooled down and measured), have shown this type of separation of CB for positive gate voltages and a FP regime for negative gate voltages. In the Coulomb blockade regime, we observe a periodic set of peaks which follow a beat periodicity in peak height (Fig. 7.3a). This suggests that the measured current is shaped from a linear combination of two regular sets of peaks coming from two CNT junctions in parallel: A difference in the capacitance from the gate to the CNT in both suspended junctions probably leads to this beat pattern with a beat periodicity of ~ 0.8 V. Furthermore, from the location, shape and the similar regularity of the conductance peaks in the CB regime, we suspect, that the two CNT junctions are formed from the same CNT which is suspended between both trenches.

7.2 SUPERCURRENT IN AS-GROWN CNT JUNCTIONS

Instead of measuring the current passing through the device to ground, we now measure the voltage across the device as a function of applied current bias and gate voltage. Figure 7.4 shows the voltage as a function of current bias for a fixed gate voltage of $V_G = -2.625$ V (which is in the Fabry-Pérot regime), the current is swept from negative to a positive current values. We measure zero voltage for a current bias range of -2 nA to +18 nA. From this we conclude that the critical current $I_C = 18$ nA. (Further measurements of forward and reverse sweeps also indicate that the superconducting CNT junctions are hysteretic (see chapter 4).)

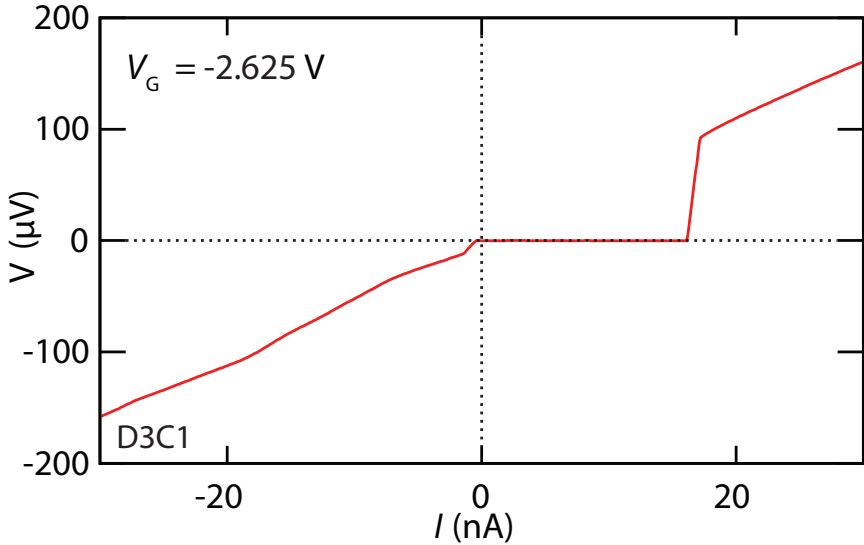


FIGURE 7.4: **Superconductivity in the FP region.** Voltage measured in a four-wire configuration as a function of current bias (I) at a fixed gate voltage $V_G = -2.625$ V. A zero-voltage is observed in the range of -2 nA to 18 nA. (The sweep direction is from negative to positive values)

Figure 7.5a shows a two-dimensional differential resistance colour map as a function of gate voltage and bias current. The black dashed vertical line indicates the gate voltage position at which the curve shown in fig. 7.4 was measured. A zero-voltage across the device (i.e. a supercurrent) is measured in the central blue region which is surrounded by a red onset to a regime which has a finite voltage. The onset of the supercurrent at positive values has been extracted from this plot and is plotted in figure 7.4b. This line thus indicates that the critical current oscillates with gate voltage. Further inspection of the data reveals, that the critical current follows the FP conductance oscillations of the CNT with gate voltage [1].

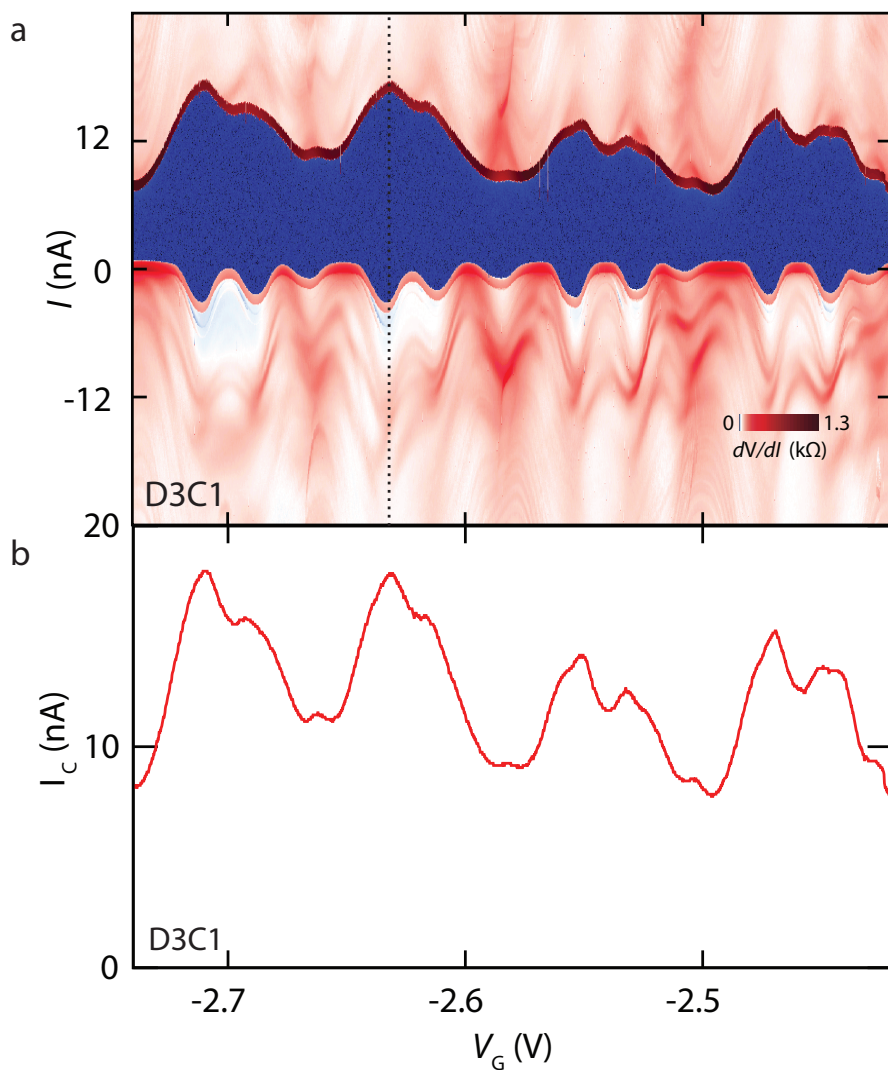


FIGURE 7.5: **Gate dependent superconductivity in the FP region.** **a** Differential resistance dV/dI colour-map as a function of V_G and current bias I (forward sweep direction). The dashed line indicates the gate position at which the curve Fig. 7.4 was taken. **b** Critical current as a function of V_G , extracted from the positive voltage onset of the upper figure. The critical current oscillates with V_G , following the modulation of the normal state conductance.

In the Coulomb regime we also see a supercurrent for high gate voltages, where the tunnel barriers become more transparent and the conductance of the device increases. Figure 7.6 shows a curve of the voltage as a function of applied bias current for a fixed gate voltage of $V_G = 2.71$ V. We measure a zero voltage response (indicating a supercurrent) for a current bias range of -0.3 nA to 2 nA.

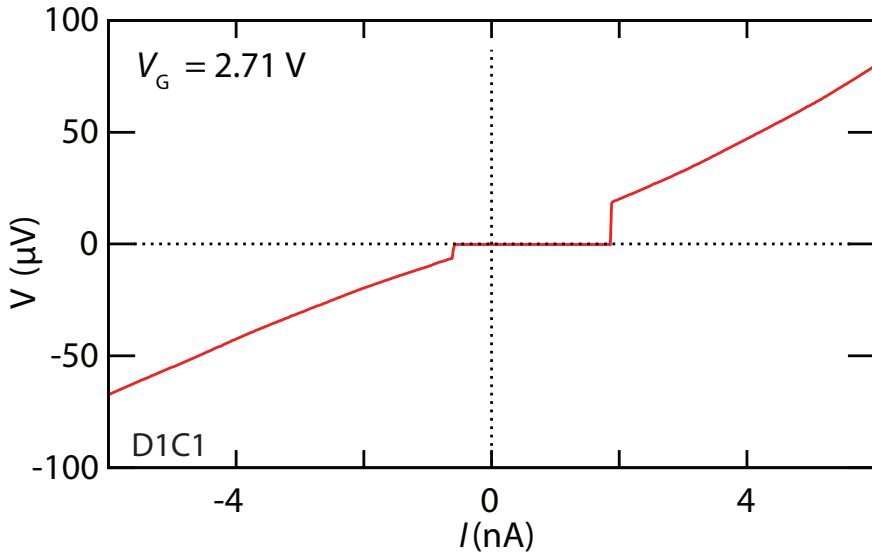


FIGURE 7.6: **Superconductivity in the QB region** Voltage (V) measured in a four-wire configuration as a function of current bias (I) at a fixed gate voltage $V_G = +2.71$ V. A supercurrent is present in the current bias range of -0.3 nA to 2 nA (forward sweep direction).

Figure 7.7a is a two dimensional colour map of the differential resistance as a function of gate voltage and bias current. The vertical dashed line indicates the gate voltage position at which the curve shown in Fig. 7.6 was measured. Figure 7.7b shows the critical current as a function of gate voltage. As in the case of the FP regime, the critical current I_C changes with gate voltage. The critical current detected in the CB regime appears to follow the CNT conductance given by the Coulomb blockade peaks, such that a high critical current is detected at a conductance peak and little or no supercurrent is detected in the Coulomb diamond itself.

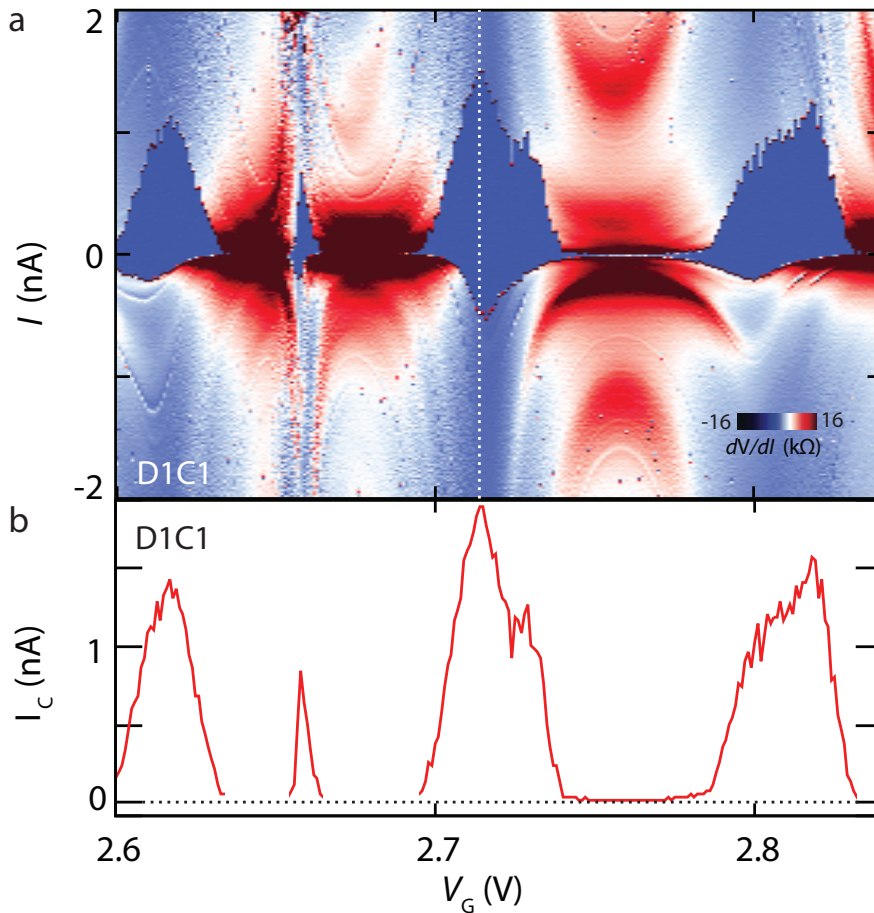


FIGURE 7.7: **Gate dependent superconductivity in the QB region.** **a** Colour map of the differential resistance dV/dI as a function of V_G and current bias I (forward sweep direction). The dashed line indicates the gate position at which the curve in Fig. 7.6 was taken. **b** Critical current as a function of V_G , extracted from Fig. **a**. The critical current oscillates with V_G , following the Coulomb oscillations of the conductance as a function of gate voltage.

7.3 ANALYSIS OF SUPERCONDUCTING IV CURVES

Until now, we have been discussing the switching current separating the zero-voltage state from a state with $V \neq 0$. In addition to an abrupt switch at I_C , the superconducting IV curves in our device present a rich set of features above I_C ; present as plateaus and kinks in them. In this section, we will take a look at these features in more detail.

Figure 7.8 shows the differential resistance (dV/dI) as a colour map as a function of gate voltage and current bias. The gate is tuned into the FP region and the blue area in the centre of the plot indicates the superconducting region. The data was recorded in a forward current bias sweep. The dashed black line indicates the gate position $V_G = -2.59$ V, at which the line cut (shown in Fig. 7.9a and b) was extracted. Figure 7.9a shows the voltage (V) as a function of bias current at the gate voltage and Fig. 7.9b shows the differential resistance (dV/dI) of this curve. As we can see from this plot, the CNT junction shows a wide range of features such as lines and plateaus in the IV , leading to pronounced dips and peaks in the dV/dI . From the colour scale plot (Fig.7.9a) we conclude that these features are modulated in gate voltage.

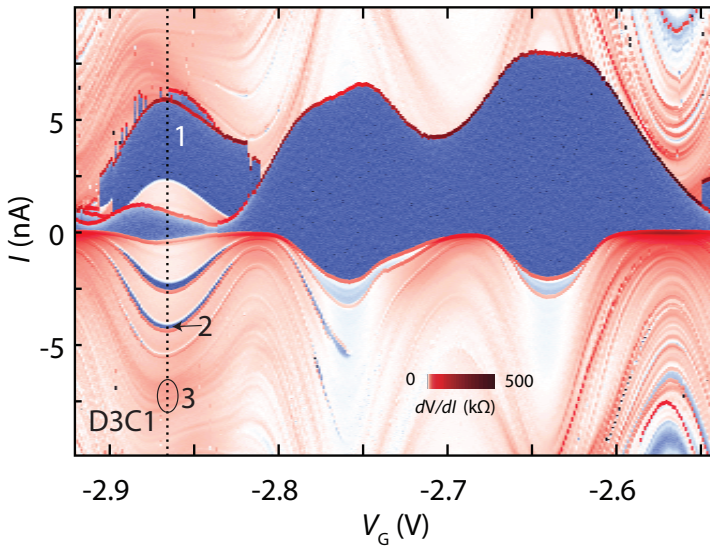


FIGURE 7.8: **Spectroscopic features in the superconducting FP regime.** a Differential resistance dV/dI colour-map as a function of V_G and current bias I (forward sweep direction).

From the curve shown in Fig. 7.9a we identify nonzero voltage plateaus of

which two are indicated by the numbers 1 and 2. In the differential resistance curve dV/dI (Fig 7.9b) we can further identify a number of smaller peaks. Both features change or oscillate with gate voltage as illustrated in Fig. 7.8.

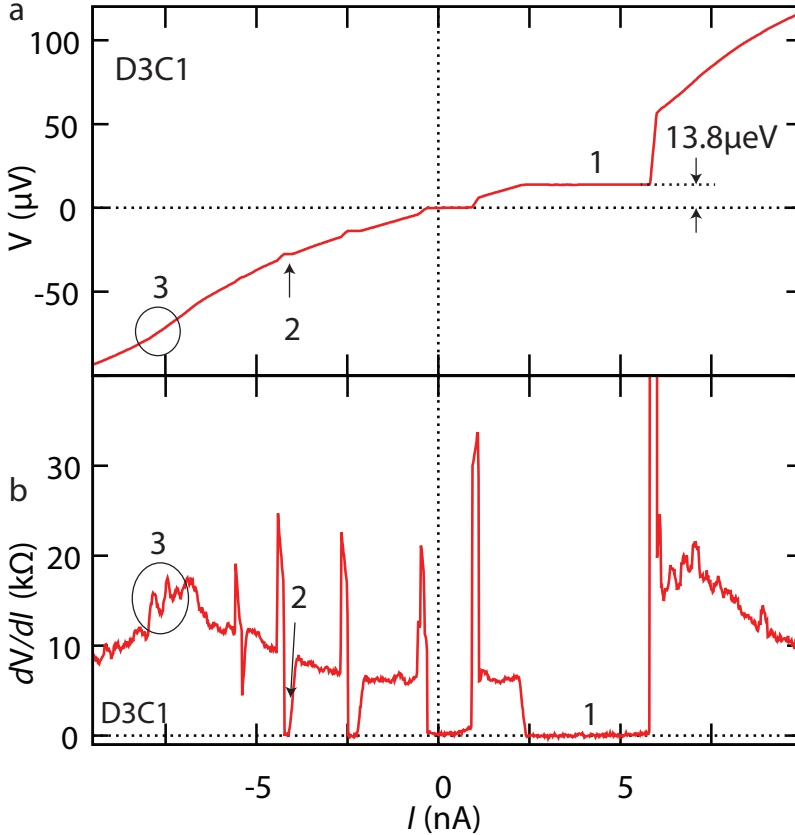


FIGURE 7.9: **Spectroscopic features in the superconducting FP regime.** **a** Voltage as a function of current bias at a fixed gate voltage $V_G = -2.59$ V. A vertical black dashed line in Fig. 7.8 indicates where this line-cut is from. The numbers '1' and '2' indicate the location of plateaus in the figures. The voltage measured of the first plateau indicated by '1' is $13.8 \mu\text{V}$, the voltage spacing between different smaller plateaus such as indicated by '2' also correspond to $13.8 \mu\text{V}$. **b** Differential resistance dV/dI as a function of current bias at $V_G = -2.59$ V. We find peaks in the differential resistance, at a negative voltage of -7.5 nA, The location is indicated by number '3' in the plots. The current bias positions of the features indicated by the numbers appear to change with gate voltage.

7.4 CONVERSION OF IV INTO VI PLOTS

In order to further analyse these features, we have replotted the data, converting voltages to bias currents. for each position in gate. The result is a two dimensional map with the applied bias current I as a function of voltage V and gate voltage V_G . Of this new map we can take the derivative such that the colour scale is the differential conductance dI/dV , i.e. this is thus a map where the two dimensional dV/dI plot shown in figure 7.10a is converted into an dI/dV plot shown in figure 7.10b.

This conversion, allows us to see what happens to the features as a function of gate voltage and the voltage (Fig. 7.10b), instead of the applied current bias (Fig. 7.10a). Features indicated by the numbers 1 and 2 remain constant with gate as they appear as horizontal lines in Fig. 7.10b. Indicated by position 3, we see a broader band-like (white) dip in Fig. 7.10b, which appears to consist of several (red) thin lines in Fig. 7.10a. This feature appears to move or disperse in both plots with gate voltage. Most features are not visible at higher voltages (white areas), a higher bias current would be needed to reveal them.

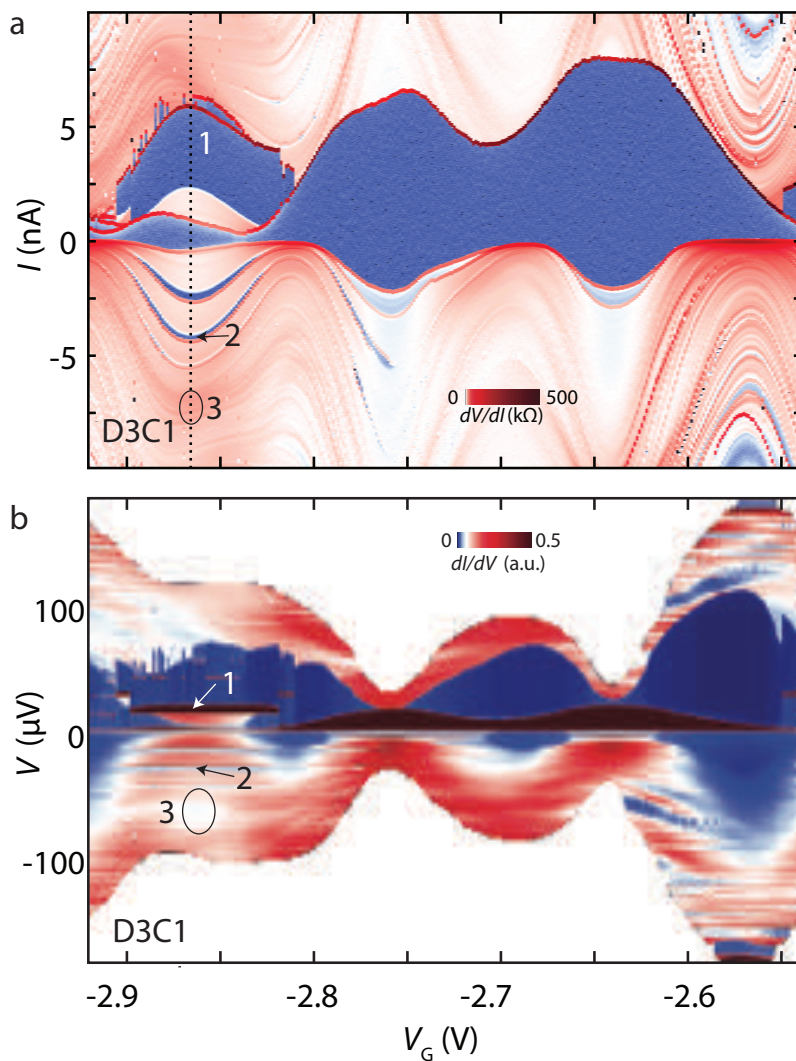


FIGURE 7.10: Spectroscopic features below 10 nA as a function of measured and gate voltage. **a** Differential resistance dV/dI map as a function of V_G and applied current bias I . **b** Remapped differential conductance dI/dV map as a function of V_G and measured voltage V . From this figure it is possible to identify features which change or do not change in voltage when the gate voltage is tuned.

To further identify the origin of these 'broader' features (seen at position '3' in Fig. 7.10), we investigated IV curves at higher bias currents. Figure 7.11a shows a two-dimensional differential resistance map with a current bias of up to 150 nA. Figure 7.11b shows the remapped differential conductance of this figure. The method used to remap the measured voltage and the applied bias current is the same as describe before.

At higher bias currents (~ 50 nA to 100 nA) and around (~ 130 nA), we identify features appearing as an array of white and blue stripes (position indicated by number '4'). These features oscillate in current bias position as a function of gate voltage (see Fig. 7.11a). In figure 7.11b (voltage bias), they appear as two different sets of steps (see supplementary information (SI) for further details). One set visible at measured voltages less than 0.5 mV, indicated by '4b') have a voltage step size of $\Delta V_{step1} = 13.8 \mu\text{V}$. The other set (visible for voltages larger than 0.5 mV, indicated by '4a') have a voltage step size of $\Delta V_{step1} = 21 \mu\text{V}$. The last (highest voltage) step of each set is the most visible one. With gate voltage, the position of the highest and most visible voltage step changes. This behaviour is different from the step-like features seen in Fig. 7.10 indicated by number 1 and 2. Because of their sharp nature and the fact that they show no gate voltage dependence, we attribute these to higher order Shapiro steps. To estimate the frequency and wavelength we use the following equation:

$$\Delta V_{step} = \frac{hf}{2e} \quad (7.1)$$

$$f = \frac{c}{\lambda}, \quad (7.2)$$

where ΔV_{step} is the measured voltage, the plank constant $h = 6.626 \cdot 10^{-34}$ Js and the electron charge $e = 1.6 \cdot 10^{-19}$ coulombs and $c = 2.998 \cdot 10^8 \frac{m}{s}$ is the speed of light. The frequency corresponding to a $13.8 \mu\text{V}$ step is $f \sim 6.7$ GHz with a wavelength of $\lambda \sim 4.5$ cm. The sample is located inside a copper can with an diameter of ~ 4 cm. The distance from the sample to the wall is ~ 2.2 cm, which is very close to a distance corresponding to $\lambda/2$. We think that these steps are Fiske-like steps, generated by the current bias across the JJ and the copper can surrounding it which acts as a cavity at low temperatures. The voltage difference for each step is independent of gate voltage, however we find that the step order, that has the highest visibility is gate voltage dependent (see also Fig.7.25 in the SI.), the reason for this is unclear. The gate dependence might be related to the change in the Fermi energy level in the CNT, as it increases with gate voltage.

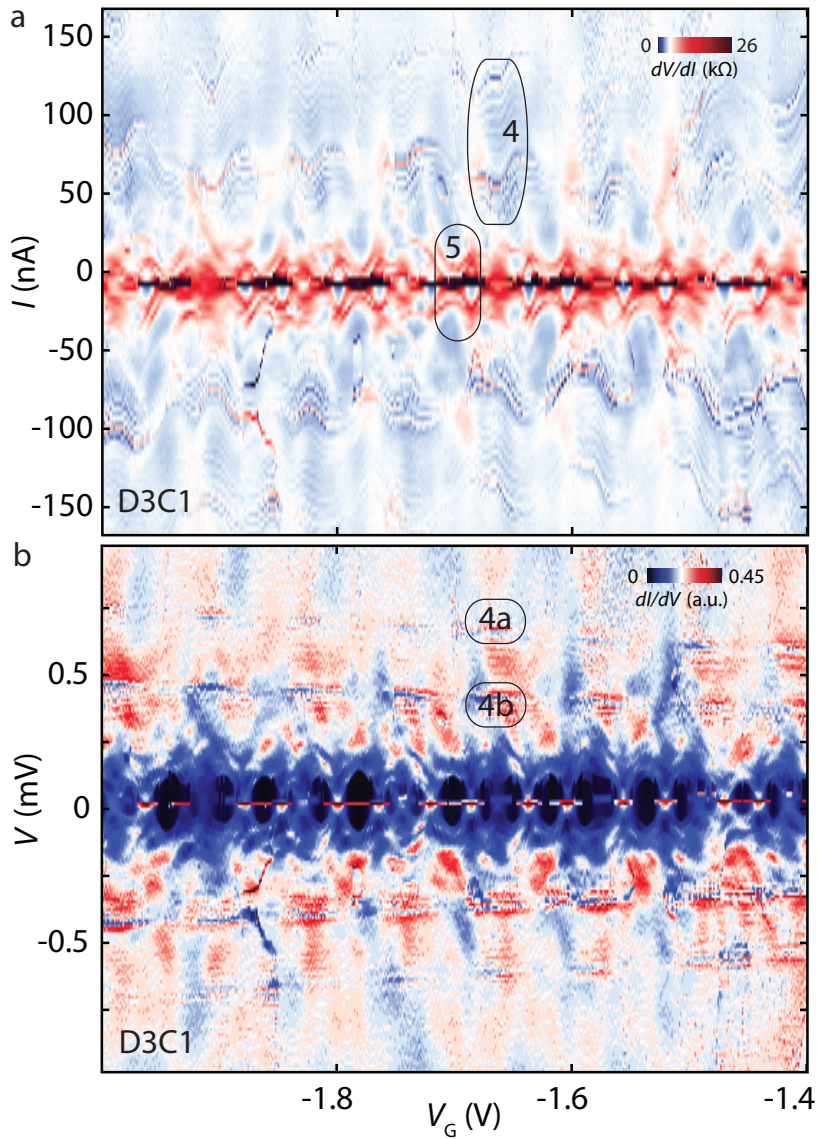


FIGURE 7.11: **Spectroscopic features up to 150 nA.** **a** Differential resistance dV/dI colour-scale map as a function of V_G and current bias I . **b** Remapped differential conductance dI/dV colour-scale map as a function of V_G and measured voltage V .

Around lower bias currents (± 25 nA) we recognise features (indicated by number 5 in Fig. 7.11 as those seen previously in the low current bias figure 7.10 at the position indicated by number 3. They are visible in the voltage range of ± 0.25 mV (Fig. 7.11b). A zoomed version around this voltage is shown in Fig. 7.12. These features appear to disperse in both, voltage and bias current position as a function gate voltage (Fig 7.11 a and b). This is in contrast to superconducting-insulating-superconducting (SIS) junctions and to multiple Andreev reflections (MAR) in (SNS) superconducting-normal-superconducting junctions[2], both of which do not show gate dependence. In figure 7.12 and 7.13, we marked some of these gate dependent and dispersive features with black dashed lines. From the data presented in the SI (Fig. 7.22) we believe that $\Delta V_G = 83$ mV corresponds to the addition energy of adding four electrons to the CNT junction. The features repeat themselves every ΔV_G change in gate voltage (Fig. 7.13).

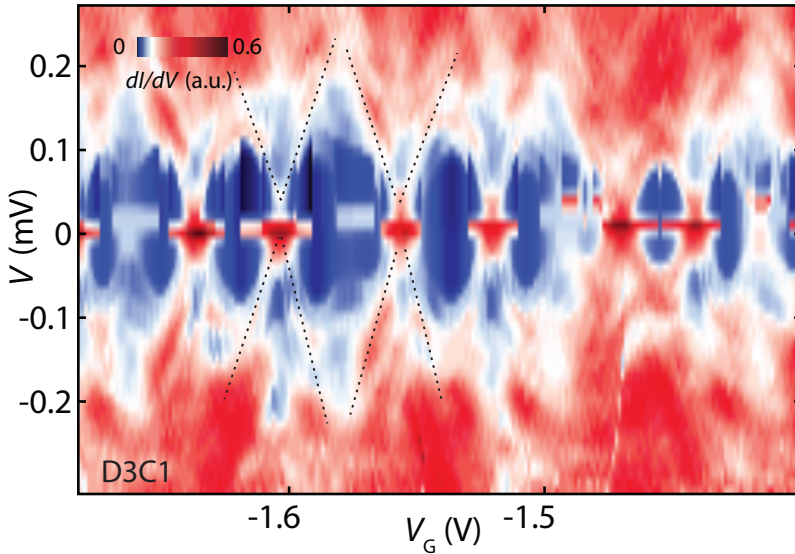


FIGURE 7.12: **Zoomed version of Fig. 7.11b.** Remapped differential conductance dI/dV colour-scale map as a function of V_G and measured voltage V .

We speculate that the low-bias features in Fig. 7.12 and 7.13 might be related to Andreev bound states (ABS). It appears that these features appear when a FP single particle (SP) energy level enters a low enough bias voltage. The dispersive nature shows a clear repeating gate dependent pattern which is similar to that seen in chapter 2 (Fig. 2.15). In contrast to the theory plots shown in chapter 2 (Fig.2.15b),

the lines here appear blurred (which will be discussed later). ABS resonances appear inside the superconducting gap when single particle levels get close to the Fermi energy of the leads (see SI) [3]. To check this, we should show that these features (indicated by the black dashed lines in Fig. 7.12 and 7.13), are indeed the FP single particle (SP) energy levels, crossing through the Fermi energy of the leads, into the superconducting gap. To identify the superconducting gap and see the FP SP energy levels, we need to go to higher bias currents.

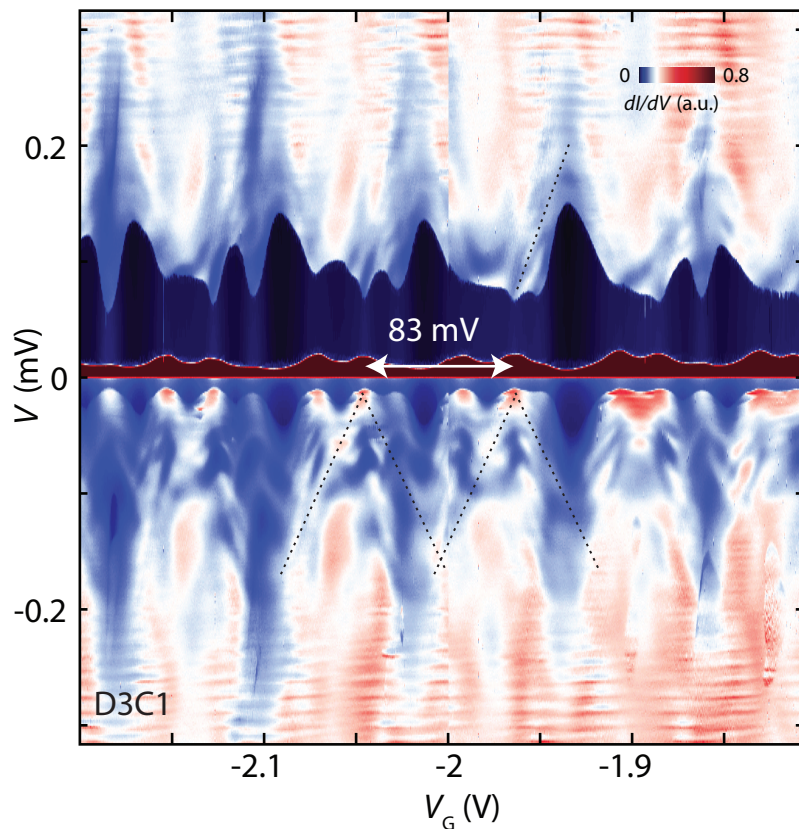


FIGURE 7.13: **Zoomed version of Fig. 7.11b, with a much slower and higher resolution forward sweep rate.** Remapped differential conductance dI/dV colour-scale map as a function of V_G and measured voltage V . This data was recorded at a different gate voltage with a much slower and higher resolution forward sweep (additional data in the SI Fig. 7.25).

7.5 SPECTROSCOPY UP TO 2 μA CURRENT BIAS

To establish the presence of FP transport through our device and to identify the gate voltage positions where these FP energy levels align with the Fermi energy, we now show the differential conductance and resistance map for applied bias currents up to $I_B = \pm 2 \mu\text{A}$.

In Fig. 7.14a we show the differential resistance as a function of gate voltage and current bias of up to $I_B = \pm 2 \mu\text{A}$. The figure shows a new different pattern oscillating with gate for current biases larger than $\pm 250 \text{ nA}$. The visibility of these pattern decreases for current biases larger than $\pm 1 \mu\text{A}$. Figure 7.14b shows the remapped differential conductance dI/dV as a function of gate voltage and voltage. From this figure we can recognise the previously described periodic pattern (for currents larger than 250 nA) as Fabry-Pérot interference oscillations. The visibility of these patterns are highest for voltages around 2 mV. A zoomed window (of Fig. 7.14b) showing these FP oscillations more clearly is shown in Fig. 7.15.

From Figure 7.15, we can estimate the FP SP energy level spacing and find that $\Delta_{SP} = 2.1 \text{ meV}$. The capacitive gate to CNT coupling (α) can be extracted from:

$$\Delta_{SP} = \alpha \cdot 83 \text{ meV}, \quad (7.3)$$

so that $\alpha \approx 1/40$. The CNT is suspended across an 800 nm long trench size. The corresponding expected FP energy level spacing is:

$$\Delta_{SP} = \frac{hV_F}{2L} = 2.1 \text{ meV}, \quad (7.4)$$

where $V_F = 8.1 \times 10^5 \text{ m/s}$ is the electron Fermi velocity in a metallic CNT, h is Planks constant and L is the length of the suspended nanotube segment. The measured and the expected value for the FP energy level spacing match very well. Note that in the CB regime the Coulomb peak to Coulomb peak gate voltage is 21 mV; This value thus corresponds to the addition energy of one electron. Four times 21 mV is in good agreement with the 83 mV value found in the FP regime. This also indicates that the length of the quantum dot is approximately the same as that of the suspended carbon nanotube segment.

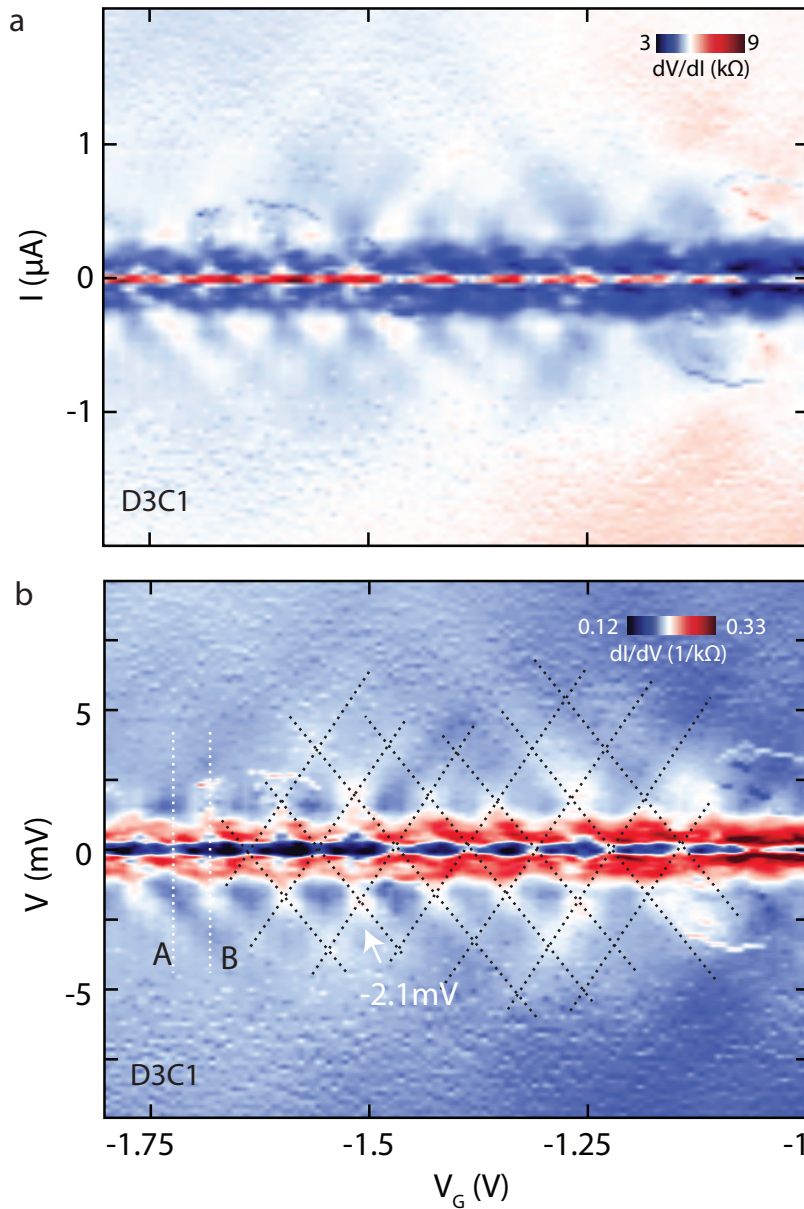


FIGURE 7.14: **Spectroscopic features up to $2 \mu\text{A}$.** **a** Differential resistance dV/dI (colour) as a function of V_G (horizontal axis) and current bias I (vertical axis). **b** Remapped differential conductance dI/dV (colour) as a function of V_G (horizontal axis) and measured voltage V (vertical axis). The black dashed lines indicate conductance peaks due the FP oscillations. The two vertical white dashed lines labeled A and B indicate positions at which a line cut was extracted from (shown in Fig. 7.17).

7.5.1 CONCLUSION

The spectroscopic features seen in Fig. 7.13 are likely associated with the FP single particle levels crossing the Fermi energy. We therefore speculate that the features indicated by the black dashed lines in Fig. 7.12 and 7.13, correspond to the ABS spectroscopy in a ballistic carbon nanotube-SNS junction.

The phase in an SNS-Josephson junction is $\phi = \phi_0 + \frac{2eV}{\hbar} t$. This means that during our spectroscopic measurements, the phase is oscillating much faster than the time scales in the measurement. This is in contrast to the ABS seen by [3], where the phase could be carefully tuned with an magnetic field and did not oscillate much faster than the measurement. Since the ABS disperse with phase [3], this suggests that the measurements represent a phase averaged density of states (DOS) of the ABS levels. Understanding this phase averaged measurement in an SNS junction is currently a topic of active theoretical investigation.

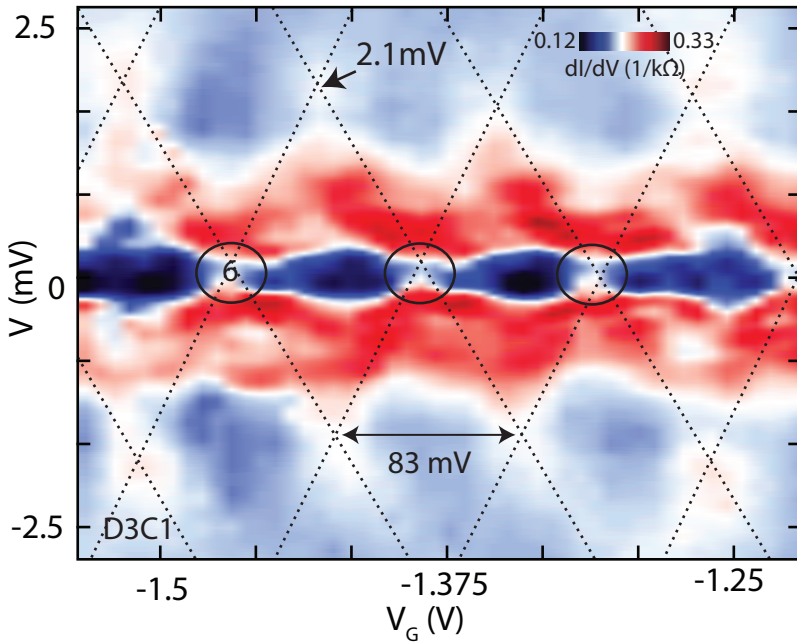


FIGURE 7.15: **Zoomed figure of Fig. 7.14.** From this figure we obtain $\Delta = \frac{\hbar V_F}{2L} = 2.1$ meV and $\Delta = \alpha \cdot 83$ meV.

The data shown in Fig. 7.14b can also be used to estimate the effective D.O.S. of our device. Figure 7.17a shows the differential conductance dI/dV as a function

of voltage for two different gate positions (vertical line cuts indicated in Fig. 7.14b, A and B). Graph A is located at a gate position where I_C is large and graph B is at a gate position where I_C is small. Figure 7.17b shows a graph of the differential conductance dI/dV versus the voltage which was created by averaging across gate positions seen in Fig. 7.14b. From Fig. 7.17c (which is a zoom of b), we see superconducting "mini gap"-like features[4–6] which appear as a suppression around $V = 0$ mV with a width of $2\Delta_{mini} = 0.5$ meV. The estimated superconducting gap of the Molybdenum-Rhenium alloy film with[7]:

$$\Delta = 3.528 k_B T_C, \quad (7.5)$$

where $k_B = 1.38 \cdot 10^{-23} \text{ JK}^{-1}$ is the Boltzmann constant and with a $T_C = 4.5$ K, we get $\Delta = 1.37$ meV. From Fig 7.17 it is clear that electrons in our CNT-Junction are not tunnelling in and out of a superconductor with a 'hard' BCS gap. Such soft 'minigaps' have been observed before in superconductors in which the superconductivity is induced by the proximity effect[8, 9]. The inset in Figure 7.17c shows a schematic for a likely explanation for the origin of the 'mini gap' - like features we observe. From previous pioneering work on Josephson junction interfaces[10–12], we assume that our superconducting leads consists themselves of "proximity induced" nanotube segments (S') on top of the superconducting metal (S). As shown in the drawing (Fig. 7.16), an electron traveling from the CNT would first 'see' an interface to an proximity induced superconducting nanotube before it sees the superconductor.

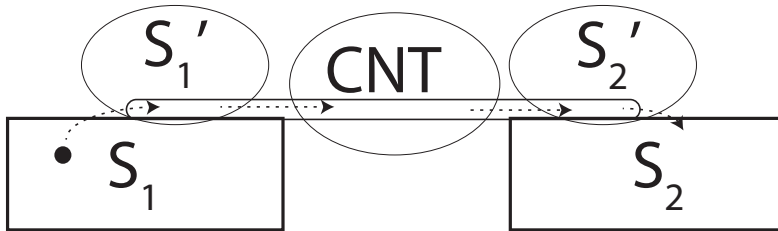


FIGURE 7.16: Drawing illustration proximity induced nanotube segments.

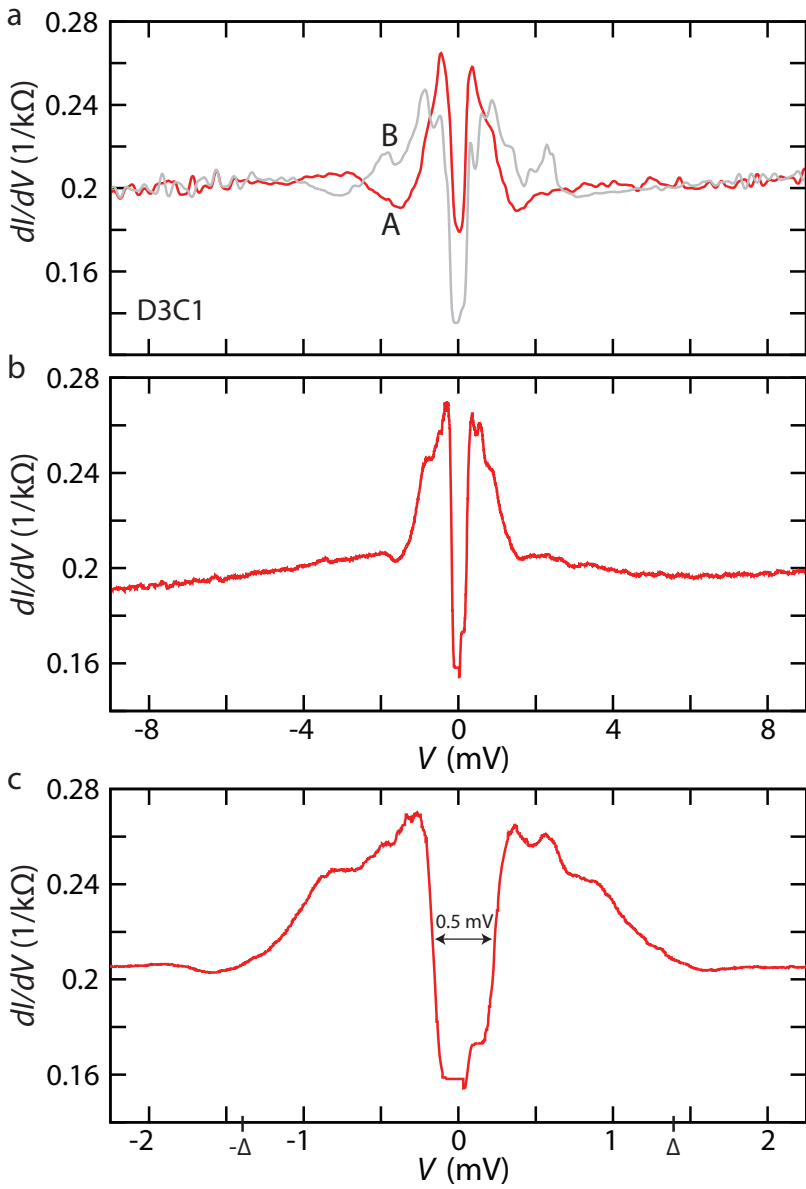


FIGURE 7.17: **Extracted line cuts from Fig 7.11b.** **a** extracted line-cut at position A and B. **b** averaged line-cut along all positions in gate. **c** magnification around ± 2 mV of **b**.

7.6 SPECTROSCOPY IN THE COULOMB BLOCKADE REGIME

Now we present data in the Coulomb blockade regime. For our CNT devices with MoRe contact leads we find that at low temperatures, in general, we see Coulomb blockade for positive gate voltages.

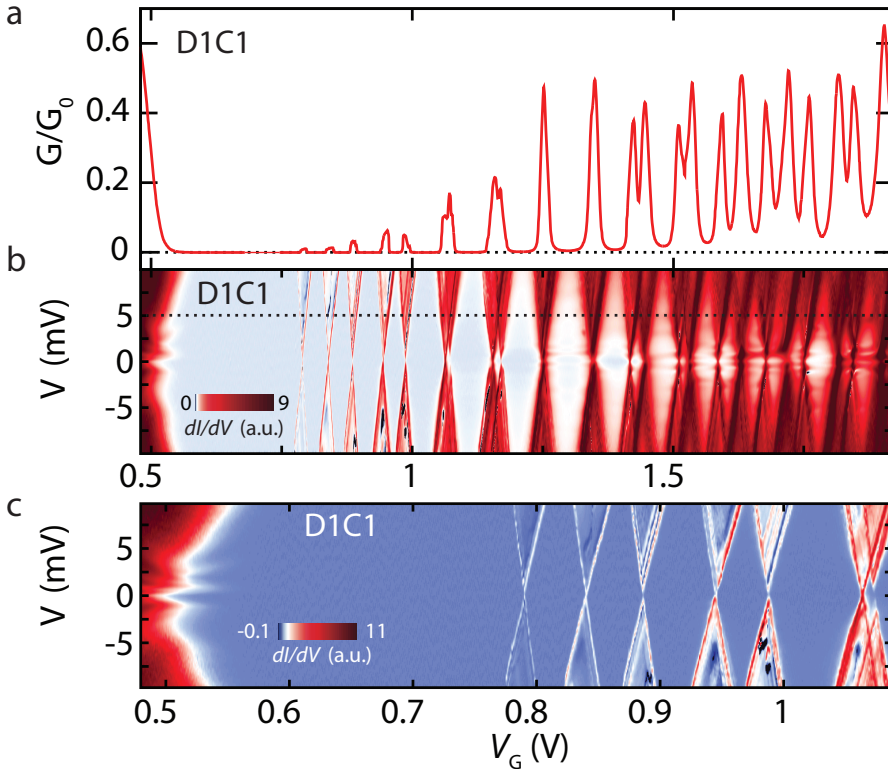


FIGURE 7.18: **Spectroscopy of the device in CB.** **a** Conductance (G/G_0) as a function of gate voltage. **b** Differential conductance dI/dV (colour) as a function of gate voltage (horizontal axis) and voltage bias (vertical axis). **b** Zoom of **b** shows the first visible diamonds. Signs for sequential tunnelling appear already with the 2 and 3 diamond. (see Fig. 7.19a)

Figure 7.18 shows the low-bias conductance of a CNT as a function of gate voltage, normalised to the conductance quantum $2e^2/h$. For gate voltages larger than 0.5 V we see a low conductance with periodic conductance peaks. The peak height increases with gate voltage. This indicates that the device is in the CB regime. Figure 7.18b shows the differential conductance dI/dV (colour) as a function of gate

(horizontal axis) and voltage bias (vertical axis). The figure corresponds to two sets of Coulomb diamonds from the two suspended CNT segments (see also Fig.7.3). The horizontal black dashed line indicates the voltage position at which the conductance trace shown in Fig. 7.18a was measured.

With increasing gate voltage, two observations can be made: The conductance peak heights, shown in Fig. 7.18a, on average increase with gate voltage. Features, such as horizontal lines present at low voltage biases within the Coulomb diamonds, increase in number and visibility.

7.6.1 VISIBLE FEATURES IN THE CB REGIME.

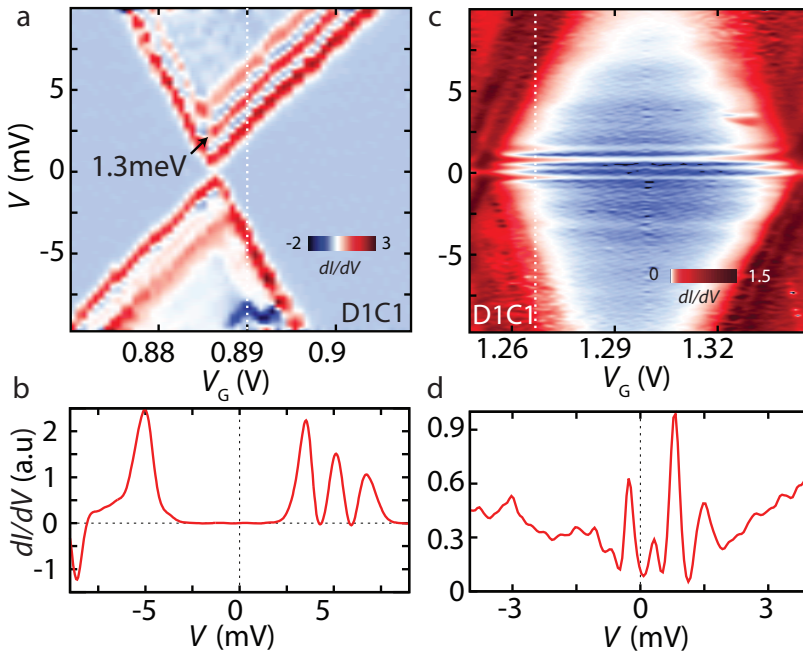


FIGURE 7.19: **Zoomed figures extracted Fig. 7.18.** **a,c** Differential conductance (colour) as a function of gate voltage (horizontal axis) and voltage bias (vertical axis). **b,d** are vertical line cuts extracted from Fig. **a** and **c** respectively. Their extraction positions are indicated by a vertical white dashed line (figures above them). **a** Crossing point separating two states showing excited states. At low energy, an arrow points at the excited state of 1.3 meV. **c** Coulomb diamond at a higher gate voltage than for **a**. Inside the Coulomb diamond (low conductance, blue area in the centre), Kondo-like features start to appear including several faint horizontal features visible at higher voltage biases.

Figure 7.19a is a zoom-in differential conductance of one of the first CB diamonds shown in Fig. 7.18b. Sequential tunnelling is observed at the edge of the Coulomb diamond. A black arrow points at an excited state with an excitation energy of $E_{ex} = 1.3$ meV. A vertical line-cut across the edge of the diamond (indicated by the white dashed line) is shown in Fig. 7.19b.

When increasing gate voltage horizontal lines start to appear within the Coulomb diamonds. Figure 7.19c shows a Coulomb diamond at higher gate voltages. It shows several horizontal lines. A vertical line-cut (white dashed line in Fig. 7.19c), shown in Fig. 7.19d, reveals two large peaks in the differential conductance, asymmetrically located with respect to $V = 0$. The features point at co-tunnelling with peaks, peaks followed by ridges. These most likely arise from Kondo enhanced co-tunnelling[13] (Split Kondo peaks) from the spinner valley degrees of freedom in the nanotube, which is split at zero magnetic field by the spin orbit coupling. Although from the datasets other explanations such as non-equilibrium Kondo-effects[14] cannot be ruled out.

7.7 NDC IN CO-TUNNELLING AT HIGHER GATE VOLTAGES

With increased gate voltage, the n-doping in the carbon nanotube segment increases and the tunnel barrier decreases (as the depletion length for free p+ decreases). Figure 7.20 shows the differential conductance (colour scale) as a function of gate and voltage bias at gate voltages between 1.9 V and 2.7 V. Figure 7.21a is a zoom in of Fig. 7.20. The vertical white dashed line indicates where the line cut shown in Fig. 7.21b was taken.

From Fig. 7.20 and 7.21a, we recognise our previous (Fig. 7.19c) 'co-tunnelling with peaks' lines within the diamonds (horizontal lines). For higher gate voltages we can identify kondo-like features, which are followed by those 'co-tunnelling with peaks' lines. (Similar to those seen in chapter 2 Fig. 2.8c) However, at some positions we observe a negative differential conductance; Fig. 7.21b shows an example with negative differential conductance dips at -0.8 mV and at 1 mV.

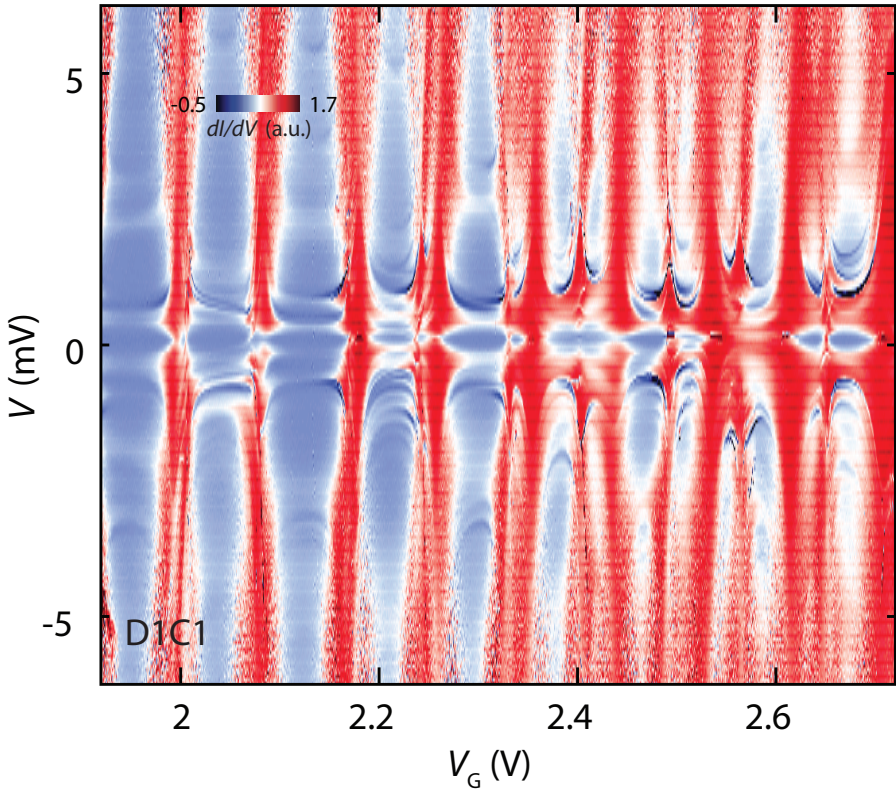


FIGURE 7.20: **Spectroscopic features in the Coulomb blockade regime.** Differential conductance dI/dV colour-map as a function of V_G and bias voltage V .

7.7.1 CONCLUSION

We think that the NDC is due to the superconducting leads. The effect was not present for low gate voltages, but as we increase the gate voltage, we increase the Fermi energy and decrease the resistance. This may in turn increase the influence of the superconducting contact leads and making proximity effects from the superconductor more likely to appear. An analysis of some of the observed bias features, (such as the peaks seen at higher bias voltages) was done in similar devices by Andersen et al.[15]. The origin of the negative differential conductance is unclear to us; we have seen this in other CNT-JJ devices as well.

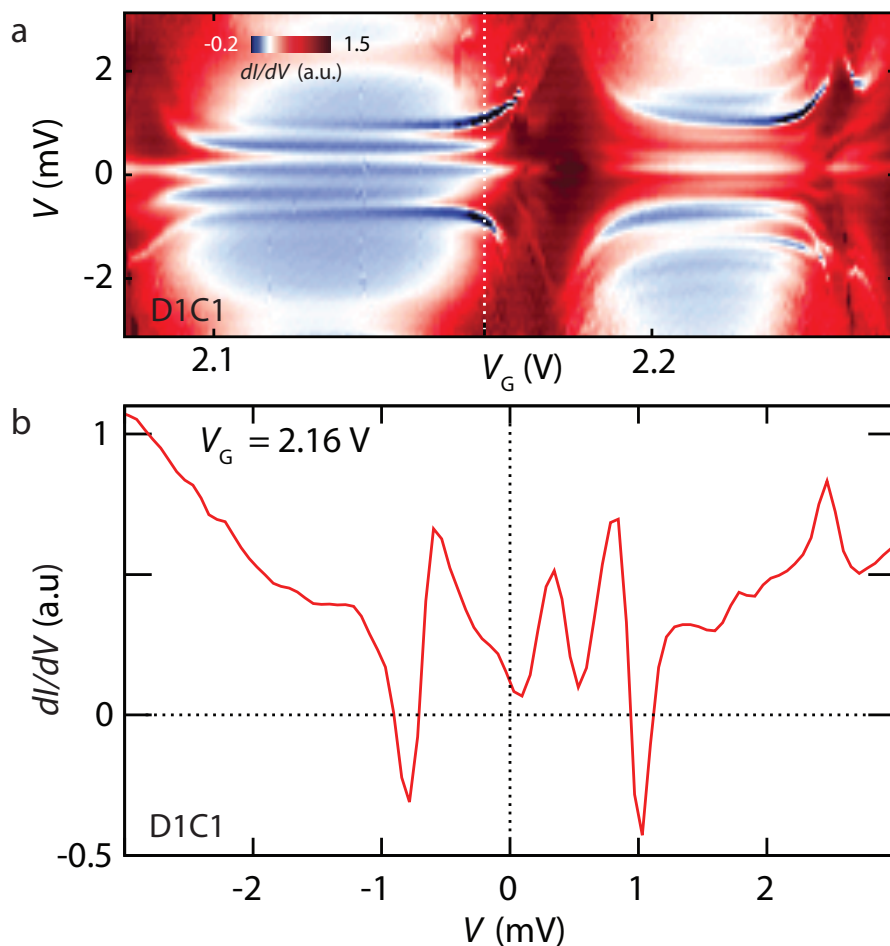


FIGURE 7.21: **Spectroscopic features in the Coulomb blockade regime.** **a** Differential conductance dI/dV colour-map as a function of V_G and bias voltage V . Zoom-in of two Coulomb diamonds in Fig. 7.20 which shows a negative differential conductance. **b** Differential conductance dI/dV line cut versus bias voltage at $V_G = 2.16$ V (dotted line in a). The differential conductance is negative for $V = -0.8$ and $V = 1.0$ mV.

7.8 SUMMARY AND CONCLUSION

We presented basic characterisation of a typical as grown CNT-JJ device with MoRe contact leads. We show that these devices carry a supercurrent in the FP and CB regime. From the IV and VI analysis, we distinguish several features some of which are gate dependent and others that are independent (i.g., Shapiro-steps). In the low-current bias map (up to $150 \mu\text{A}$, Fig. 7.11) we observe features which suggest the presence of Andreev bound states, correlated to single-particle energy levels, visible in the $2 \mu\text{A}$ current bias map (Fig. 7.14 and 7.15). Unlike in other previous devices such as those in Ref. [3] we do not see a hard superconducting gap but rather a mini-gap (Fig. 7.17). We think that when the single-particle energy levels enter this gap, Andreev-bound state features become visible in the IV curves.

In the Coulomb blockade regime we identify common features such as sequential tunnelling, co-tunnelling with peaks and Kondo lines. Additional to these we also observe negative differential conductance for higher gate voltages, whose origin is not clear to us yet. We suggest further experiments using hybrid junctions where a single carbon nanotube is suspended between superconducting and non-superconducting electrodes. Such a device would allow us to probe the Andreev bound energy levels, without a rotating phase in the superconducting contact leads (which arises when a voltage is applied to a JJ).

7.9 SUPPLEMENTARY INFORMATION

7.9.1 BASIC CHARACTERISATION AT 25 mK

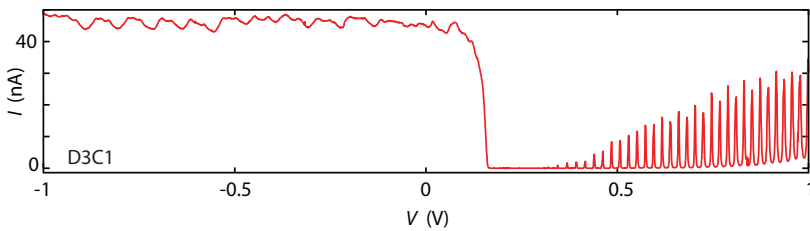


FIGURE 7.22: **Electric spectroscopic characterisation of a double SNS junction at 25 mK.** Two-terminal current I as a function of V_G and a fixed source-drain voltage bias ($V_B = 2 \text{ mV}$) of device D3C1. For negative V_G the conductance is high with small oscillations (Fabry P erot regime) for positive V_G the conductance is low with large oscillations (Coulomb blockade)

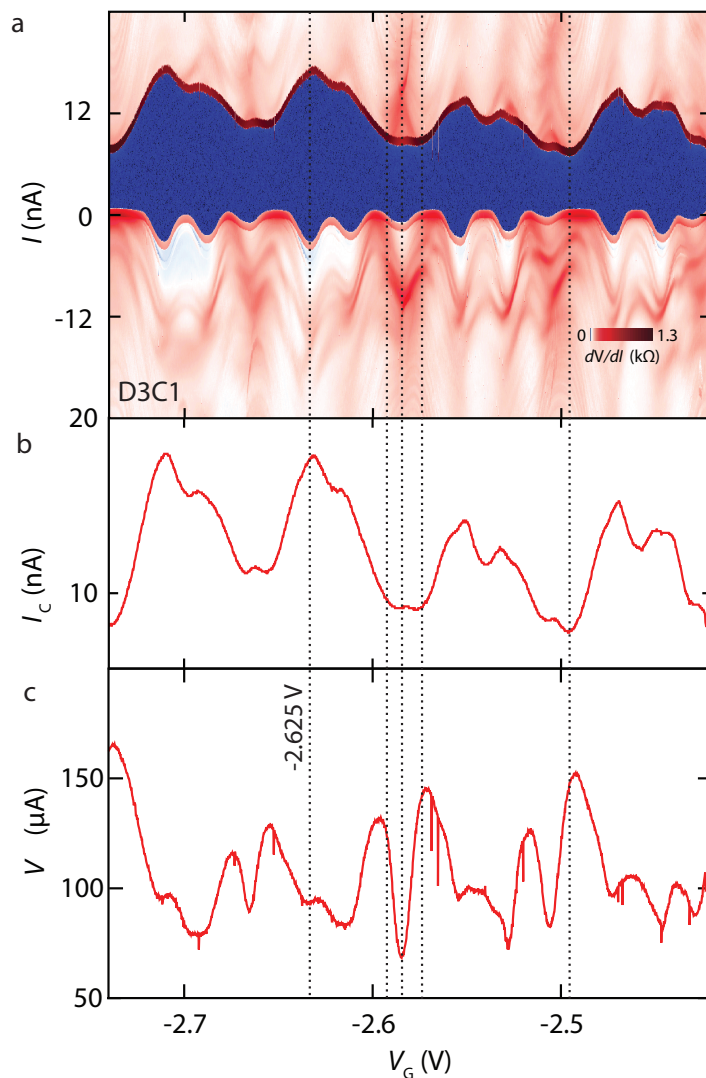
7.9.2 $I_C R_N$ PRODUCT IN THE FABRY PÉROT REGIME

FIGURE 7.23: **Gate dependent superconductivity in the FP region.** **a** Differential resistance dV/dI colour-map as a function of V_G and current bias I (forward sweep direction). **b** Critical current as a function of V_G , extracted from the positive voltage onset of the upper figure. The critical current oscillates with V_G , following the modulation of the normal state conductance. **c** Voltage measured directly above I_C as a function of gate voltage. Note that this measured voltage corresponds to a product of I_C times the CNT resistance present at this current.

7.9.3 CNT-JJ DEVICE SHOWS HYSTERETIC BEHAVIOUR

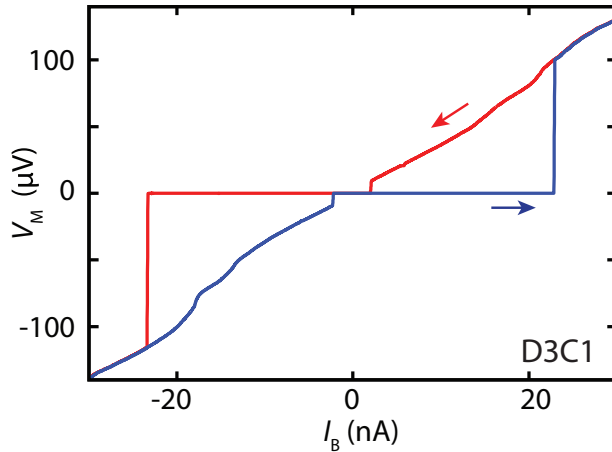


FIGURE 7.24: **Forward and backward current sweep of the CNT-JJ.** Four-terminal current-voltage trace at $V_G = -1.1\text{V}$. The onset of the resistive branch occurs at 24 nA, corresponding to a critical current of 12 nA per nanotube junction. The device is hysteretic, as can be seen from the forward (blue) and reverse (red) sweep directions[16].

7.9.4 SPECTROSCOPY UP TO 100 nA CURRENT BIAS

Figure 7.25a shows a two dimensional differential resistance map with a current bias of up to 100 nA. Figure 7.25b shows the remapped differential conductance of this. The method used to remap the measured voltage and the applied bias current is the same as described in the main text. The difference between this figure and the figure in the main text (Fig. 7.14) is that the data was measured in a different cool down (same device) and with a higher resolution in the current bias and the gate voltage sweep (slower).

From figure 7.25 we see that the superconducting region which is located in the centre (light blue region) which oscillates with gate voltage. Similar to the figure in the main text (Fig. 7.14), we see dispersive features at low current biases (red coloured features in Fig 7.25a). The difference is that these features are more visible and appear dominant for negative current biases. This is likely due to the hysteresis of the device, where a higher supercurrent is present for positive current biases, masking features at low voltages. This means that one should compare the negative current bias features to the experimental data seen of Pilet et al. [3].

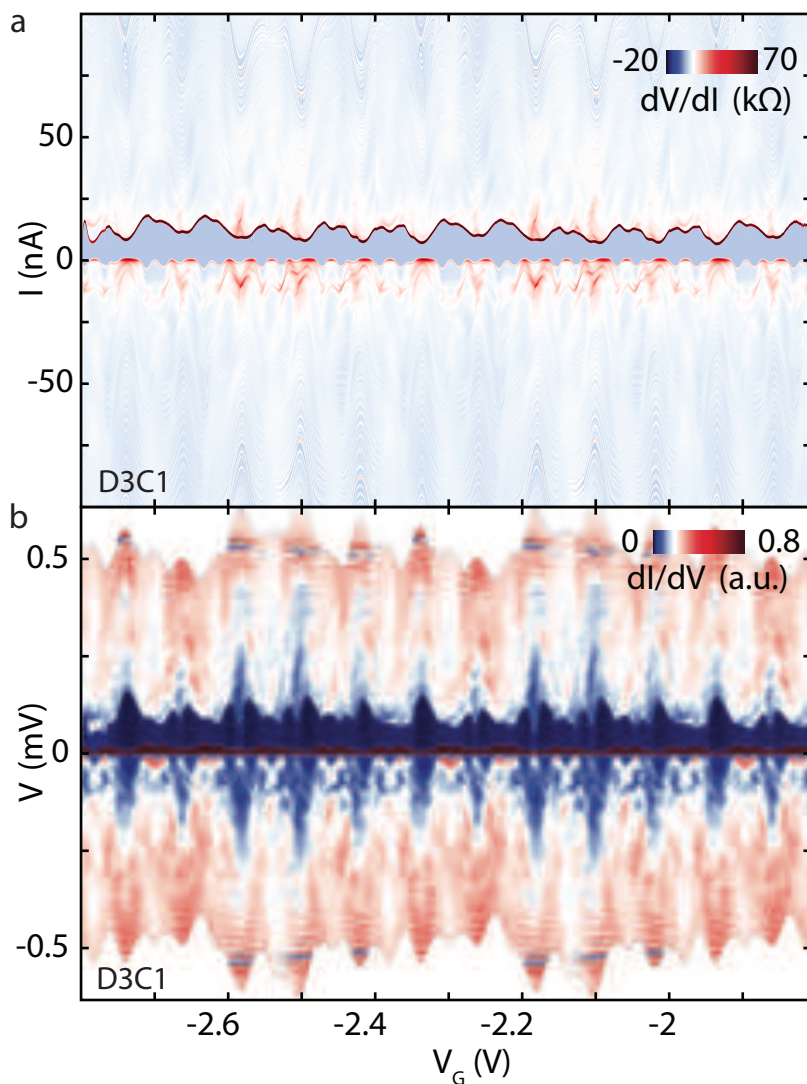


FIGURE 7.25: **Spectroscopic features up to 100 nA.** **a** Differential resistance dV/dI colour-scale map as a function of V_G and current bias I . **b** Remapped differential conductance dI/dV colour-scale map as a function of V_G and measured voltage V . (This data was taken from the same device as for Fig. 7.11, however at a different cool-down. The data was recorded at a high resolution and slower ramp-speed.)

REFERENCES

- [1] B. H. Schneider, S. Etaki, H. S. J. van der Zant, and G. A. Steele, *Coupling carbon nanotube mechanics to a superconducting circuit*, Sci. Rep. **2** (2012).
- [2] P. Jarillo-Herrero, J. A. Van Dam, and L. P. Kouwenhoven, *Quantum supercurrent transistors in carbon nanotubes*, Nature **439**, 953 (2006).
- [3] J. D. Pillet, C. H. L. Quay, P. Morfin, C. Bena, A. L. Yeyati, and P. Joyez, *Andreev bound states in supercurrent-carrying carbon nanotubes revealed*, Nature Phys. **6**, 965 (2010).
- [4] J. Wang, C. Shi, M. Tian, Q. Zhang, N. Kumar, J. K. Jain, T. E. Mallouk, and M. H. W. Chan, *Proximity-induced superconductivity in nanowires: Minigap state and differential magnetoresistance oscillations*, Phys. Rev. Lett. **102**, 247003 (2009).
- [5] B. Crouzy, E. Bascones, and D. A. Ivanov, *Minigap in a superconductor–normal metal junction with paramagnetic impurities*, Phys. Rev. B. **72**, 92501 (2005).
- [6] J. J. A. Baselmans, A. F. Morpurgo, B. J. Van Wees, and T. M. Klapwijk, *Reversing the direction of the supercurrent in a controllable Josephson junction*, Nature **397**, 43 (1999).
- [7] M. Tinkham, *Introduction to superconductivity* (McGraw Hill (New York), 1996).
- [8] H. Le Sueur, P. Joyez, H. Pothier, C. Urbina, and D. Esteve, *Phase controlled superconducting proximity effect probed by tunneling spectroscopy*, Phys. Rev. Lett. **100**, 197002 (2008).
- [9] L. Serrier-Garcia, J. C. Cuevas, T. Cren, C. Brun, V. Cherkez, F. Debontridder, D. Fokin, F. S. Bergeret, and D. Roditchev, *Scanning Tunneling Spectroscopy Study of the Proximity Effect in a Disordered Two-Dimensional Metal*, Phys. Rev. Lett. **110**, 157003 (2013).
- [10] A. F. Volkov, P. H. C. Magnée, B. J. Van Wees, and T. M. Klapwijk, *Proximity and Josephson effects in superconductor-two-dimensional electron gas planar junctions*, Physica C: Superconductivity **242**, 261 (1995).
- [11] N. B. Kopnin and A. S. Melnikov, *Proximity-induced superconductivity in two-dimensional electronic systems*, Phys. Rev. B. **84**, 64524 (2011).

- [12] M. Vissers, V. K. Chua, S. A. Law, S. Vishveshwara, and J. N. Eckstein, *Measurement of junction conductance and proximity effect at superconductor/semiconductor junctions*, arXiv preprint arXiv:1402.6055 (2014).
- [13] T. Sand-Jespersen, J. Paaske, B. M. Andersen, K. Grove-Rasmussen, H. I. Jørgensen, M. Aagesen, C. B. Sørensen, P. E. Lindelof, K. Flensberg, and J. Nygård, *Kondo-enhanced Andreev tunneling in InAs nanowire quantum dots*, Phys. Rev. Lett. **99**, 126603 (2007).
- [14] J. Paaske, A. Rosch, P. Wölfle, N. Mason, C. M. Marcus, and J. Nygård, *Nonequilibrium singlet–triplet Kondo effect in carbon nanotubes*, Nature Phys. **2**, 460 (2006).
- [15] B. M. I. Andersen, K. Flensberg, V. Koerting, and J. Paaske, *Nonequilibrium transport through a spinful quantum dot with superconducting leads*, Phys. Rev. Lett. **107**, 256802 (2011).
- [16] J. Clarke and A. I. Braginski, *The {SQUID} handbook*, vol. 1 (Wiley Online Library, 2006).

SUMMARY

Carbon nanotubes are unique candidates to study quantum mechanical properties of a nanomechanical resonator. However to access this quantum regime, present detectors are not yet sensitive enough. In this thesis we couple a carbon nanotube CNT mechanical resonator to a superconducting circuit which is a root towards such sensitivity.

Chapter 2 provides the theory and background for this thesis. First, a brief overview is given on previously used methods to detect the motion of a suspended carbon nanotube mechanical resonator. The methods include the rectification, FM mixing and the fast readout method. Then the quantum transport of electrons in a carbon nanotube in the Fabry-Pérot and Coulomb blockade regime is explained. These explanations are supported by examples of measured data, highlighting the different features. Third, a basic description of Josephson junctions (JJ's), Superconducting Quantum Interference Devices (SQUIDs) and Andreev Bound States (ABS) in a carbon nanotube Josephson junction is given.

Chapter 3 describes the fabrication process used to make a suspended carbon nanotube Josephson junction, with as grown CNTs. For the fabrication, three different heat resistant superconductors have been explored, Niobium-Titanium-Nitride, Rhenium and Molybdenum-Rhenium (MoRe). We achieved reliable results, low contact resistances and a proximity-induced supercurrent of 14 nA by using the MoRe superconducting alloy.

In **Chapter 4**, we present a CNT-SQUID made of MoRe with suspended CNT that forms the two Josephson junctions. The supercurrent passing through the SQUID is coupled to the displacement of the carbon nanotubes by applying a magnetic field of 1 T. The suspended CNT-JJs, are then statically displaced by applying a voltage to the gate electrode located underneath. By continuously measuring the voltage across the SQUID, while sweeping a current bias, we read out the change in critical current of the SQUID, as we displace the CNT. From the oscillation in the supercurrent, we detect the displacement of the CNT. We find that one 800 nm long CNT displaces by 1.85 nm per 1 V applied to the gate electrode. At 1 T we obtain a sensitivity of $0.36 \Phi_0/\text{nm}$, where Φ_0 is the flux quantum $\frac{h}{2e}$. The expected zero-point motion of the 800 nm long CNT is 3.6 pm. Together with its Q factor 3×10^4 and resonance frequency of 125 MHz, we expect a noise level of $16 \mu\Phi_0/\sqrt{\text{Hz}}$, which is nearly two orders of magnitude larger than the sensitivity of

a SQUID ($0.2\mu\Phi_0/\sqrt{\text{Hz}}$).

Chapter 5 presents experimental results of a suspended CNT-JJ, which acts as a mechanical resonator and a Josephson junction, subject to a time depended actuation force. We measure the voltage across the CNT-JJ as a function of applied bias current and gate voltage. Additionally, the suspended CNT-JJ is actuated by a radio-frequency source emitted by an antenna in close proximity. As the gate tunes the suspended CNT into the Fabry-Pérot regime, we observe a strongly enhanced mechanical signal at low-bias currents, when a mechanical mode is driven on resonance. We attribute this enhanced signal to the strong nonlinearities in the current bias and gate voltage. This allows the presence of a mixing signal at a very low current bias. These nonlinearities, arise from sub-gap states formed in the ballistic channel, and are absent in devices without superconducting contacts. Future experiments, with superconducting and normal contact leads for the same grown CNT, should shed light into these sub-gap states. From the data, we estimate an enhancement of the signal strength by a factor of 20 between low and high current biases, while the noise floor drops by a factor of 100. By using this method, we were able to easily detect the mechanical resonance modes of a CNT in the Fabry-Pérot regime.

The mechanical ringdown of a CNT is discussed in **Chapter 6**. At a temperature of 2 K, we find a difference between time scales, characterising dissipation and the decoherence of a CNT mechanical resonator, both of which are fundamentally different processes. While the driven frequency response measures a combination of both, time domain techniques can separate the two. Comparing frequency and time domain measurements of the mechanical quality factor, we find a spectral quality factor four times smaller than that measured in ringdown. This measurement shows that decoherence dominates the spectral response of a CNT resonator at low temperature. This decoherence arises at high driving powers, pointing to a non-linear dephasing mechanism. These results highlight the importance of time-domain techniques for understanding dissipation in mechanical resonators, and the relevance of decoherence mechanisms in nanotube mechanics.

Chapter 7 summarises the experimental results on suspended carbon nanotube devices with superconducting MoRe contact leads, made in the same way as described in Chapter 3. The devices have the same geometry and are made in the same way as those described in chapter 4, where a SQUID geometry was used to probe the displacement of a CNT. Unlike in chapter 5, no radio frequency was applied to the device. To identify a as-grown carbon nanotube Josephson junction, characterisation is done at room and low temperatures. This is then followed by a characterisation of the supercurrent in the Coulomb blockade and in the Fabry-Pérot regime. By analysing current-voltage (IV) and voltage-current (VI) curves at different gate voltages, different features such as Shapiro steps and single par-

ticle electron levels are distinguished. We observe a negative differential conductance in the Coulomb blockade regime, with features which suggest the presence of phase averaged Andreev bound states (ABS) in the Fabry-Pérot regime. These ABS appear to be linked to single-particle energy levels at low current biases.

SAMENVATTING

Koolstof nanobuizen zijn unieke structuren waarmee de kwantum-mechanische eigenschappen van mechanische systemen kunnen worden bestudeerd. Zeer gevoelige detectoren zijn vereist om deze mechanische bewegingen in het kwantum regime te bestuderen. In dit proefschrift koppelen we een koolstof nanobuis resonator aan een supergeleidend circuit, om een dergelijke gevoeligheid te behalen.

Hoofdstuk 2 beschrijft de theorie en de achtergrond voor dit proefschrift. Eerst wordt een koer overzicht gegeven van de in het verleden gebruikte methoden om de bewegingen van een koolstof nanobuis resonator te detecteren. Deze omvatten gelijkrichting, FM mixers, en een snelle uitleesmethode. Dan wordt het kwantum transport van elektronen in de nanobuis beschreven, zowel in het Fabry-Pérot regime als in het Coulomb-blokade regime. De uitleg wordt ondersteund met voorbeelden van gemeten karakteristieken die de verschillende regimes zichtbaar maakt. Ook worden Josephson juncties (JJ's) geïntroduceerd, Supergeleidende Kwantum Interferentie Devices (SQUIDs), en Andreev Bound States (ABS) in een koolstof nanobuis Josephson junctie.

Hoofdstuk 3 beschrijft het fabricageproces voor een device, waarin een vrij bewegende koolstof nanobuis, die is gegroeid over een opening, dient als JJ. Drie supergeleidende materialen, die bestand zijn tegen hoge temperaturen, zijn onderzocht: Niobium-Titanium-Nitride, Rhenium (Re), en Molybdenum-Rhenium (MoRe). Door MoRe te gebruiken wordt een lage contact weerstand bereikt, en een proximity-induced superstroom van 14 nA.

In **Hoofdstuk 4** presenteren we een CNT-SQUID die is gefabriceerd van MoRe, en waarin de twee Josephson juncties worden gevormd door een CNT. De superstroom door de SQUID wordt gekoppeld aan de verplaatsing van de CNT door een magnetisch veld van 1 T aan te brengen. De vrij bewegende CNT-JJs worden statisch verplaatst door een spanning aan te brengen op de gate elektrode die onder de CNT is gefabriceerd. Door de spanning over de SQUID te meten terwijl de bias-stroom wordt gevarieerd, meten we de verandering in de kritische stroom van de SQUID, terwijl we de CNT bewegen. Door de modulatie in de supercurrent in the supercurrent te meten, detecteren we de verplaatsing van de CNT. We vinden dat voor een 800 nm lange CNT, de verplaatsing per aangebrachte spanning op de gate elektrode 1.85 nm/V bedraagt. Bij 1 T verkrijgen we een gevoeligheid van $0.36 \Phi_0/\text{nm}$, met Φ_0 het flux kwantum $\frac{h}{2e}$. De verwachte nulpunts-beweging van

de 800 nm lange CNT is 3.6 pm. Samen met de Q factor, 3×10^4 , en de resonantie frequentie van 125 MHz, verwachten we een ruisniveau van $16 \mu\Phi_0/\sqrt{\text{Hz}}$, hetgeen bijna twee ordegrottes hoger is dan de gevoeligheid van de SQUID ($0.2\mu\Phi_0/\sqrt{\text{Hz}}$).

Hoofdstuk 5 geeft experimentele resultaten van een vrij bewegende CNT-JJ, die gelijktijdig fungeert als een mechanische resonator en als een Josephson junctie, die wordt geactueerd door een periodieke kracht. We meten de spanning over de CNT-JJ als functie van de aangebrachte bias-stroom en gate-spanning. Daarbij wordt de gesuspenderde CNT-JJ aangedreven door een radiofrequentie signaal, uitgezonden door een antenne in de buurt. Wanneer, met behulp van de de gate, de CNT in het Fabry-Pérot regime wordt ingesteld, zien we bij de mechanische resonantie frequentie bij een lage bias-stroom een sterk verbeterd signaal. We leggen uit dat de verbetering van het signaal is te danken aan de sterke niet-lineariteit bij de huidige bias en gate-spanning. Hierdoor kan een mengsignaal voorkomen bij een zeer lage bias-stroom. Deze niet-lineariteit is alleen aanwezig wanneer wordt gebruik gemaakt van supergeleidende contacten en ontstaat door sub-gap toestanden in het ballistische kanaal. Toekomstige experimenten, waarbij supergeleidende en normale contacten worden gecombineerd op de zelfde CNT, zouden meer inzicht kunnen verschaffen in deze toestanden. Uit de metingen schatten wij dat, ten opzichte van de hoge bias-stroom, bij de lage bias-stroom het signaal zo'n factor 20 versterkt wordt, terwijl de ruisvloer daalt met een factor 100. Door deze methode konden we de mechanische resonantie vormen van een CNT gemakkelijk te detecteren in de Fabry-Pérot regime.

De mechanische relaxatie van een CNT resonator wordt beschreven in **Hoofdstuk 6**. Dissipatie en de decoherentie zijn fundamenteel verschillende processen. Waar een gedreven frequentie response een combinatie van beide processen meet, kan een meting van het nagalmtijd de twee processen onderscheiden. Door frequentie en tijd-domein metingen te vergelijken in een CNT mechanische resonator bij een temperatuur van 2 K, vinden we een verschil tussen de tijdschalen waarop deze processen optreden. De Q-factor in de spectrum meting is viermaal kleiner dan die in de relaxatie meting. Deze meting toont aan dat decoherentie een belangrijke rol speelt in een CNT resonator bij een lage temperatuur. De decoherentie ontstaat bij hoge aandrijfkraft, hetgeen lijkt te wijzen op niet-lineaire faseruis. Deze resultaten benadrukken het belang van tijd-domein technieken om de dissipatie van mechanische resonators te bestuderen, en laten zien dat decoherentie een rol speelt in de dynamica van nanobuizen.

Hoofdstuk 7 vat de experimentele resultaten samen van koolstof nanobuizen met supergeleidende MoRe contacten, gemaakt zoals werd beschreven in hoofdstuk 3. De devices hebben dezelfde geometrie en worden op dezelfde wijze benut als in hoofdstuk 4, waarbij een SQUID werd gebruikt om de verplaatsing van een CNT te detecteren. Anders als in hoofdstuk 5, wordt nu geen radiofrequentie sig-

naal gebruikt. Om een schone koolstof nanobuis Josephson junctie te identificeren, wordt deze karakteriseert bij kamertemperatuur en bij lage temperaturen. Dit wordt dan gevolgd door een karakterisering van de superstroom in de Coulomb blokkade en de Fabry-Pérot regime. Door het analyseren van stroom-spanning (IV) en spanning-stroom (VI) curves bij verschillende gate-spanningen, worden verschillende fenomenen geobserveerd, zoals Shapiro stappen en enkel-deeltje elektron niveau's. In het Coulomb-blokkade regime vinden we negatieve differentiële geleiding, en indicaties voor de aanwezigheid van fase-gemiddelde Andreev gebonden toestanden (ABS) in het Fabry-Pérot regime. Deze ABS lijken verband te houden met enkel-deeltje energie niveaus bij lage bias-stroom.